The Rhodium Less Travelled:
Understanding the Influence of Bipyridyl Ligand Substituents on
[Cp*Rh] Catalysts for Hydrogen Evolution

Thesis by:

William N. G. Moore

Submitted to the Faculty of the Department of Chemistry in
Partial Fulfillment of the Requirements for Departmental Honors in Chemistry

KU
THE UNIVERSITY OF
KANSAS

Lawrence, Kansas
April 2019

Acknowledgements

First and foremost, I must acknowledge the guiding force in my research career over the past three years: Professor James Blakemore. For being willing to take a sophomore student into a new lab, for pushing me to attend and present at conferences around the nation, for teaching me new approaches every week at group meeting, for supporting my schoolwork, for supporting me financially, I thank you. The list goes on and on, but there is one piece in particular that merits individual mention. Without your tremendous efforts to compile, elaborate on, and explain my junior year research project, there is no way it would ever have been published. And publishing that paper was a monumental moment for two huge reasons. Primarily, it was extremely gratifying to me to see my research recognized as a peer-reviewed contribution to the existing body of scientific literature. That is quite literally a dream come true. Moreover, however, having a published paper was a key component in getting me into several reputable graduate schools, including my eventual choice: the University of California, Irvine. Thanks for everything James.

Of similar import is the man that got me interested in chemistry originally: Professor Misha Barybin. I came to KU as "undecided," meaning that I had not declared a major. Taking two honors general chemistry courses freshman year with Misha changed that. I immensely enjoyed pretty much everything about those classes, including the way he taught all the concepts from a fundamental standpoint, the way he used physical, in-class demonstrations, and the way he encourage everyone to go up to the front board from time to time. Meeting with him outside of class multiple times over the winter not only convinced me to declare a major in chemistry but also to join a research group. Discussions with Misha helped me to realize priorities I didn't know I had, and from those Misha guided me to look into and eventually join Dr. Blakemore's lab group.

Under different tutelage freshman year, it is highly unlikely I would still be pursuing chemistry to the degree (no pun intended) I am now.

Another absolutely vital contributor in making this thesis possible and not coincidentally also the person most responsible for developing my passion for research in specific is my mentor: Wade Henke. My first experiment under different mentorship was unsuccessful, but Wade soon took me under his wing and showed me a reaction that worked. As I began to develop those skills, he would show me more and more complicated procedures and experiments. Throughout those first six months I'm sure I asked him about a thousand questions, but he answered just about every single one. If there was any one he didn't know, he would find the answer somehow and tell me later. The fact that he created an environment in which I was free to ask questions and learn by doing, rather than by just watching him, exponentially increased my interest in research. I owe so, so much to Wade.

My committee is also an indispensable part of this thesis, of course, and they deserve mention here. My principle investigator Professor James Blakemore and faculty advisor Professor Misha Barybin have been mentioned above, but I would like to also formally acknowledge Professor Chris Elles. If there is one course in the chemistry major gamut that is known for being difficult, it is physical chemistry lab. And truth be told, I was extremely nervous for that class, but fortunately my professor was Chris. As not the smartest person in the class, I found his explanations clear and understandable despite the subject matter being relatively difficult. I would also like to thank Chris for being willing to serve on this committee despite being on sabbatical this semester; that does not go unnoticed.

If there's a theme in this section, it's that I have to thank a lot of people, and this section will be devoted to thanking the rest of my group members for their contributions to my

development as a chemist, researcher, and person. Our group post-doc Davide Lionetti is perhaps the most intimidating person I have ever met, but has simultaneously become one of the best teachers I have ever met (despite never taking a class from him). Whenever I come to him with a problem, he does a terrific job of getting me to realize that I already know the answer if I would apply knowledge in this way or that. And in the instances where I don't know the answer, he most certainly does, and he will explain it in terms on my level that I can understand. I would also like to thank my "peer" undergraduate student in the lab, Emily Boyd, as she has pushed me to work harder and smarter in lab because she herself works at a nearly unfathomable level. I put "peer" in quotes because she may be the same grade as me, but she is lightyears in front of me as a student and researcher. My close friends and coworkers Amit Kumar, Keaton Prather, Tyler Kerr, Shaun Kelsey, and Julie Hopkins all work just as hard as Emily if not harder and thus push me to be better in that respect as well. Amit in particular has been a recent inspiration with his passing orals in March. Notably, they also help me to decompress outside of research as well as the occasion arises, whether that being going to the recreation center or Taco Tuesday. I may not have as much contact with the other elder graduate students Katie Johnson, David Sconyers, and Yun Peng, but they facilitate a hard-working environment in lab as well. The new graduate students Riddhi Golwankar and Joseph Karnes definitely fit this description as well. Yun Peng has been helpful in specific given her expertise in the rhodium framework with which I work. Lastly, I will mention the three younger undergraduate students Jonah Stiel, Taylor Tompkins, and Toni Tompkins for their continued work in lab as well. As my current mentee, I will give a special shout-out to Toni for her perpetual curiosity and willingness to work around a range of schedule difficulties to make it into lab.

Lastly, but perhaps most significantly, I thank my immediate family: my mom Jana Graham, my dad Kent Moore, and my brother Andrew Moore. Nigh on everything positive that I contribute to the world can be traced back to their influence. My mom and dad raised me to be kind, curious, studious, logical, and pretty much every other positive adjective you can think of. I definitely don't always live up to that, but I hope that this thesis is a proper reflection of those adjectives as they relate to my research in chemistry. Speaking of chemistry, my brother wrote a 152 page chemistry lab report in high school for his International Baccalaureate class. If that didn't inspire me to work harder writing my 5 page organic lab reports, I don't know what did. Examples big and little abound, but suffice it to say my family is the original reason for essentially all of the positive impact I have on the world, including (hopefully) this thesis.

Abstract

Electrocatalytic hydrogen evolution is an attractive route for storing renewable energy in the form of chemical bonds. As chemical bonds, in the form of fuels, provide energy that can be used virtually anytime and anywhere, energy storage could help overcome the intermittence of most sources of renewable energy. This is largely due to the facts that hydrogen (H_2) is clean (carbon-neutral), simple (made up of only four particles, two electrons and two protons), and energy dense ($\Delta H_f = 436$ kJ/mol).[1] Electrolytic generation of H_2 requires an excessive electrical energy input without a suitable catalyst, and thus there is currently high interest in finding suitable catalysts for this transformation. Catalyst development is especially important, if this type of system is to be deployed in practical, industrial settings. Homogeneous molecular electrocatalysts are attractive for this purpose because they can be studied spectroscopically before, during, and after catalysis. For this study, the framework [Cp*Rh(bpy)] (where Cp* = pentamethylcyclopentadienyl and bpy = 2,2'-bipyridyl) was selected, due to the modular nature of the bpy ligand. It has been recognized that this ligand can be involved in managing electron density associated with these complexes during catalysis, but little work has been done to investigate the properties engendered by extremely electron withdrawing substituents on the bipyridyl ligand. Moreover, little is known about how such substituents affect the overall redox behavior of the [Cp*Rh(bpy)] fragment.

Chapter 1 of this thesis describes an in-depth investigation into the characteristics of a [Cp*Rh] complex (**1**, see Figure 1) bearing the 4,4´-dinitro-2,2´-bipyridyl ($^{4,4'-NO2}$bpy) ligand and multiple reduced forms of **1**. Isolated **1** was characterized by several forms of spectroscopy including nuclear magnetic resonance, electronic absorption, and mass spectrometry. Moreover, single crystals suitable for X-ray diffraction analysis were grown, and the structure of **1** solved

with the help of Dr. Victor W. Day. Electrochemical studies reveal that **1** is the first example of a monometallic [Cp*Rh] complex that exhibits three quasi-reversible one-electron reductions and a fourth irreversible reduction. In these studies, a rather large spacing between the redox events (~ 0.5 V) suggested the possibility of isolating one or more of the reduced species. In accord with this theory, the singly reduced species (**2**) could be chemically prepared and isolated. UV-visible absorption spectra display new peaks that correspond to the readily observed color change from red/orange to green upon reduction of **1** to **2**. X-band electron paramagnetic resonance spectroscopy confirms the paramagnetic nature of **2**, and reveals a narrow signal at $g = 2.006$, consistent with the majority of the unpaired electron density being localized on the $^{4,4'\text{-NO2}}$bpy ligand. Cyclic voltammetry and spectroelectrochemistry further confirm that **2** is produced by both electrochemical and chemical reduction of **1**, and that the second reduction of **1** is primarily metal-centered. Electrocatalytic studies reveal that the extremely electron-withdrawing nature of the nitro substituents effectively eliminates catalytic function, providing insight into the features that govern catalysis in [Cp*Rh] complexes.

Chapter 2 describes investigations of a second less-studied aspect of the [Cp*Rh(bpy)] framework: namely, the role of less symmetric substitution of the bipyridyl ligand in modulating reduction potentials and catalytic competence. In this work, a new divergent synthetic route was developed, in which known synthetic steps were strategically assembled to provide straightforward access to a small family of [Cp*Rh] complexes bearing a single substituent at the 4-position of the bpy ligand. The method thus developed enabled preparation of three new C_1-symmetric complexes with different substitutions at the 4 position of one of the pyridine rings of the bpy ligand: –NO$_2$ (**3**), –Cl (**4**), or –NH$_2$ (**6**). NMR spectroscopic characterization supports successful formation of the new diamagnetic compounds. Hammett analysis reveals a dependence of intraligand charge

transfer (ILCT) energy and metal-to-ligand or ligand-to-metal charge transfer (MLCT or LMCT) energy on the bpy ligand substituents, as reported by use of the σ_p^+ parameter. Electrochemical studies also confirm a Hammett parameter dependence of the reduction potentials of the new compounds, confirming an important role for singly substituted bipyridyl-type ligands in influencing the electrochemical behavior of [Cp*Rh(bpy)]-type complexes. Specifically, the more electron-donating substituents (as judged via the σ_p^- parameter) are associated with complexes displaying more negative reduction potentials. Building on the findings from Chapter 1, cyclic voltammograms collected with complex **3**, bearing the 4-nitro-2,2′-bipyridyl ligand, reveal slow chloride ligand loss upon one-electron reduction, implicating significant stabilization of the singly-reduced form by the single electron-withdrawing nitro group. As the chemical and electrochemical properties of these complexes are readily modulated by substituent effects, the strategy of ligand modification can thus be realistically anticipated to afford fine-grained control of electrocatalysis in future studies.
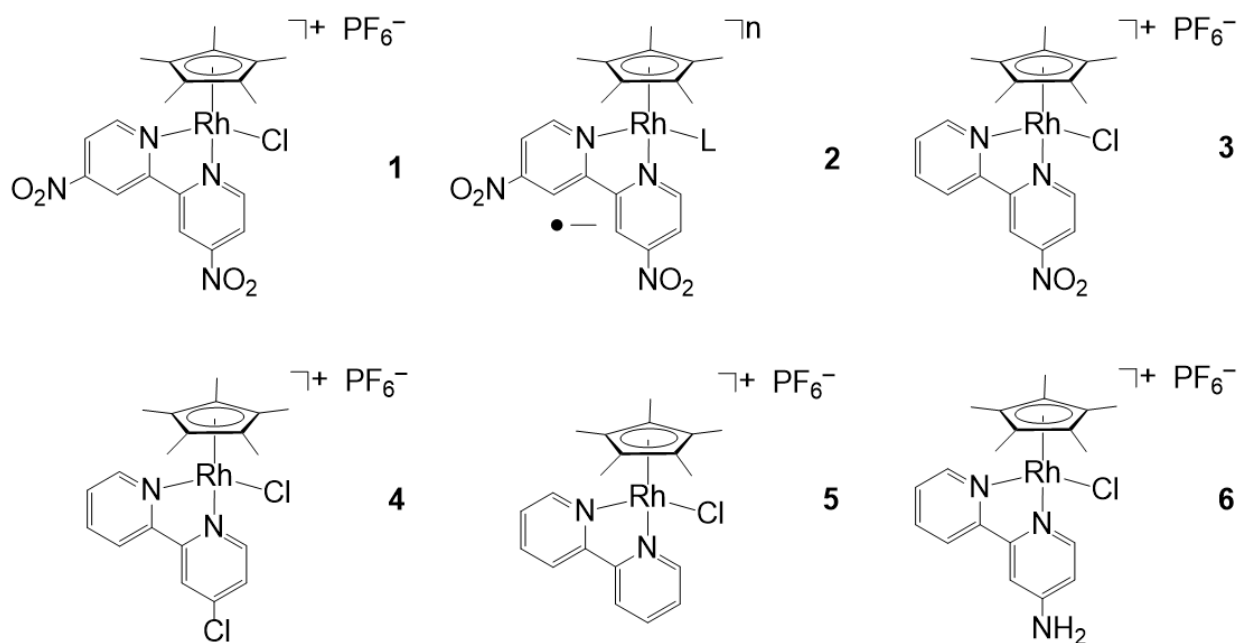
Figure 1. Compounds discussed extensively within this Thesis.

Chapter 1. Single-Electron Redox Chemistry on the [Cp*Rh] Platform Enabled by a Nitrated Bipyridyl Ligand

Introduction

Increased use of fossil fuels over the past century has caused unprecedented levels of greenhouse gases in the atmosphere.[2] Examining the levels of carbon dioxide, a prototypical greenhouse gas, in the atmosphere over the past 60 years reveals a trend that directly correlates with a rise in the average global temperature.[3] Given that there is a scientific consensus that a temperature increase over 2°C will result in irreversible changes to environments around the world, it would be advantageous to utilize carbon-neutral energy sources to avoid or slow catastrophic climate change.[4] Several such renewable energy sources already exist; widespread use of solar and wind energy is becoming more and more common in the United States, and usage is expected to increase over the coming decades as well.[4] This is great in principle, but comes with two associated challenges. First, most renewable energy sources, including the aforementioned two, are intermittent.[5] That would preclude their use on a full-time basis unless an efficient, large-scale energy storage program could be developed. Second, these sources tend to face the difficulty of distribution; in other words, the locations where the most sun and wind is available contrasts with places where most of the world's population density is located.[5] In both cases, transforming the electrical energy produced by these clean energy sources into a high-density chemical bond for usage later would be desirable, as chemical fuels can be stored indefinitely and are readily transferrable.

One of the simplest chemical bonds, and also fortunately one of the most energy dense, is found in the molecule dihydrogen.[1] Notably, sole use of the electricity generated by renewable energy to accomplish this bond formation requires enough energy input that it remains challenging to accomplish in a cost competitive way at industrial scales. Therefore, a significant body of research has focused on rationally designing electrocatalysts to facilitate this transformation and

ideally make it industrially viable. Four main categories of catalyst design persist: molecular (free flowing in solution), surface-attached (molecular catalysts attached to a surface), metal surfaces, and nanoparticles. Of this list, the only candidate that can be probed spectroscopically before, during, and after catalysis is the molecular electrocatalyst. This is an extremely advantageous characteristic because it provides more tools to determine how exactly the molecule performs its catalytic function.

The rhodium-based system developed by Kölle and Grätzel is a model system for molecular electrocatalysts and incorporates these considerations.[6] Importantly, it is a broadly useful model system for evolving dihydrogen in both aqueous and non-aqueous environments.[6] Interestingly however, although it has been around for over 30 years, a definitive mechanism for how it performs its catalytic function has not been fully elucidated.

As it stands currently, it is known that the parent compound **5** undergoes a $2e^-$ reduction prior to becoming catalytically active. In detail, this entails an electrochemical reduction-chemical change-electrochemical reduction (ECE) sequence as follows.[24] First, the parent cation is reduced by one electron to yield a transient neutral species with all original ligands bound. This is the first electron transfer (E) component. This compound likely has a highly electron-rich metal center, because it is known to undergo loss of the chloride ligand and subsequent shift of the bipyridyl ligand such that it results in being at a $180°$ angle with respect to the Cp* ligand. This is the chemical change (C) in the ECE process. This new species is a transient cation with a more positive reduction potential than the starting material and thus undergoes immediate reduction at that potential (E) to yield a neutral species. This formally Rh^I species has been chemically isolated and is known to be relatively highly catalytic for hydrogen evolution upon exposure to protons and a sufficiently reducing potential.[34,7]

My coworker Wade Henke recently published a paper in which he altered the catalytic pathway by which an analogous compound in this family performs catalysis by attaching highly electron-withdrawing trifluoromethyl substituents to the 4 and 4' positions of the bipyridyl ligand.[8] Cyclic voltammetry shows a 2e⁻ reduction much like the others in this family of [Cp*Rh] complexes. However, the positive shift in reduction potential (by about 250 mV) and broad appearance of the feature suggest that the singly reduced metal center might less readily give up its chloride ligand.[8] In other words, the CF_3 groups likely result in a metal center that is less electron dense even after reduction.

We reasoned that substitution with even more electron withdrawing functional groups could result in breaking up the 2e⁻ reduction event into separate 1e⁻ redox events. Leütz and coworkers actually published a paper in which they studied $[Cp*Rh(^{4,4'-NO2}bpy)Cl][Cl]$.[9] As nitro substituents are among the most electron withdrawing substituent available, we were extremely interested as to their findings.[10] Interestingly, they did not observe any reduction events for their complex in aqueous conditions.[9] However, as their methods relied upon a "robotic," high-throughput synthetic scheme and testing procedure, we anticipated that full synthesis and characterization of $[Cp*Rh(^{4,4'-NO2}bpy)Cl]^+$ (**1**) could provide more information on this type of complex.[9]

In this chapter, a study of compound **1**, which bears nitro substituents at the 4 and 4' positions of the bipyridyl ligand, is presented. This compound shows a markedly different electrochemical profile in non-aqueous conditions than that of Leütz's compound and that of a typical compound in the [Cp*Rh] family. **1** displays three quasi-reversible redox couples in CV and a fourth redox event that is chemically irreversible. Investigation of the first reduced form of the complex yields pertinent information concerning the nature of where exactly the complex gets

reduced and why a ligand-centered reduction (rather than metal-centered) may shut down productive catalysis.

Synthesis and Characterization of 1

Known procedures were strategically combined in order to synthesize the 4,4'-dinitro-2,2'-bipyridine ($^{4,4'-NO2}$bpy) ligand as outlined below in Figure 2.[11,12,13,14,15,16]

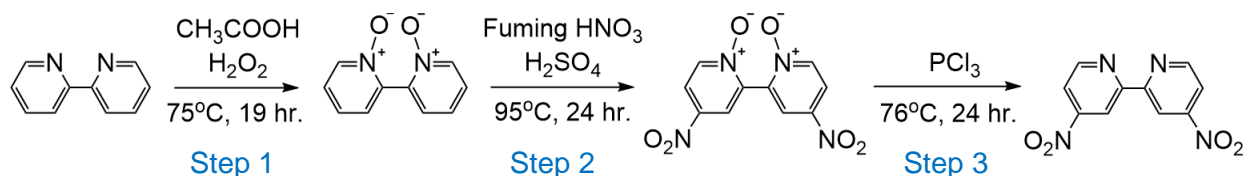**Figure 2.** Synthesis of $^{4,4'-NO2}$bpy: Step 1. Protection of the pyridyl nitrogens, Step 2. Nitration of at the para positions with respect to the pyridyl nitrogens, and Step 3. Deprotection of the pyridyl nitrogens.

Coordination to rhodium is accomplished by alteration of a known procedure (Figure 3), and involves use of the [Cp*RhCl$_2$]$_2$ complex developed by Maitlis.[17,18] A mass of 0.031 g (0.051mmol, 1 equiv.) [(Cp*)RhCl$_2$]$_2$ was suspended in about 5 mL of THF. Subsequent addition of 0.025 g (0.101 mmol, 2 equiv.) $^{4,4'-NO2}$bpy and 0.026 g (0.101 mmol, 2 equiv.) AgPF$_6$ to the THF suspension (in that order) was carried out. The resulting AgCl precipitate was then filtered off and the solution concentrated. Precipitation of bright yellow complex **1** was accomplished via addition of 50 ml diethylether. Drying the resulting solid provides 0.029 g of the desired product at 44% yield.
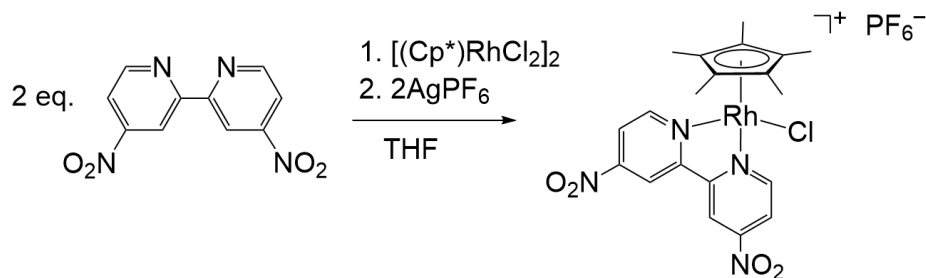
Figure 3. Synthesis of **1** in THF.

Analysis via NMR is shown in Figures 4-7. The four signals in the ^{1}H NMR of Figure 4 correspond to the four proton environments in complex **1**. The three signals between 8-10 ppm show up in the aromatic region and integrate to two each. These correspond to the six protons on the bipyridyl rings (only three signals observed due to the C_s symmetry in solution). The signal integrating to 15 in the aliphatic region corresponds to the 15 protons on the methyl groups attached to the Cp ring. In Figure 5, the six ^{13}C{^{1}H} signals also all correspond to complex **1**. The five most downfield signals correspond to the bipyridyl carbons, as they are all in a conjugated π system shifted downfield due to the nitro groups. The doublet at approximately 99.69 in the ^{13}C{^{1}H} spectrum corresponds to the carbons on the Cp* ring and appears as a doublet as a result of being split by Rh, which has $I = \frac{1}{2}$. The most upfield signal corresponds to the methyl carbons surrounding the Cp ring. Figure 6, showing the ^{31}P NMR, shows a single signal split into a septet. This corresponds to the phosphorus atom in the PF$_6$ counteranion split by the attached fluorines (as fluorine has $I = \frac{1}{2}$ as well). The ^{31}P NMR in Figure 6 and all other ^{31}P NMR in this Thesis are absolutely referenced via the H$_3$PO$_4^-$ standard in Mestrenova. Finally, the ^{19}F NMR in Figure 7 shows a single signal split into a doublet. This corresponds to the fluorines in the counteranion split by phosphorus (also having I = $\frac{1}{2}$). The ^{19}F NMR in Figure 7 and all other ^{19}F NMR in this Thesis are absolutely referenced to the CCl$_3$F standard in Mestrenova.
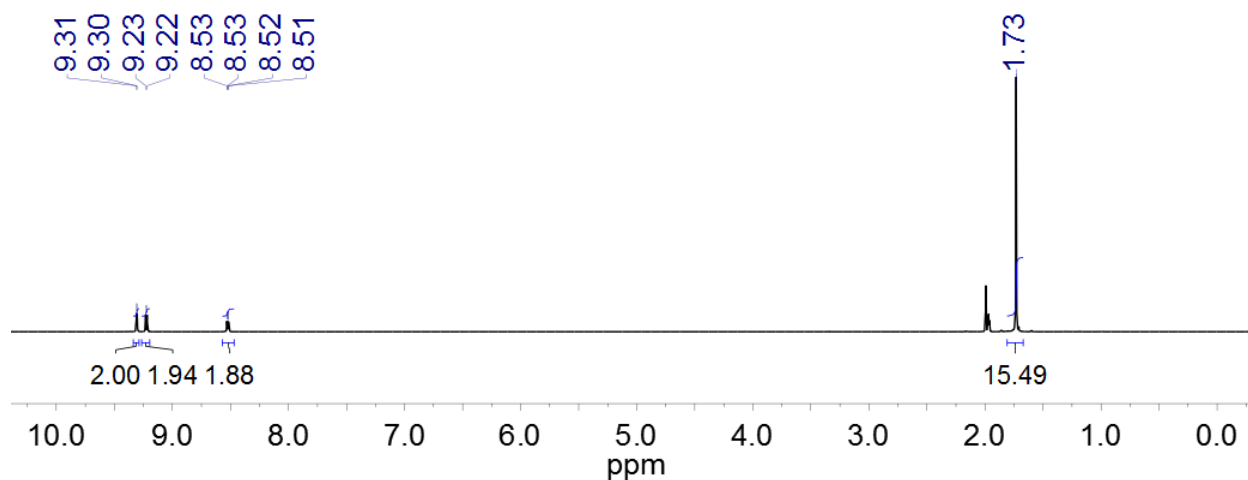
Figure 4. ^{1}H NMR spectrum (500 MHz, CD$_3$CN) of **1**.
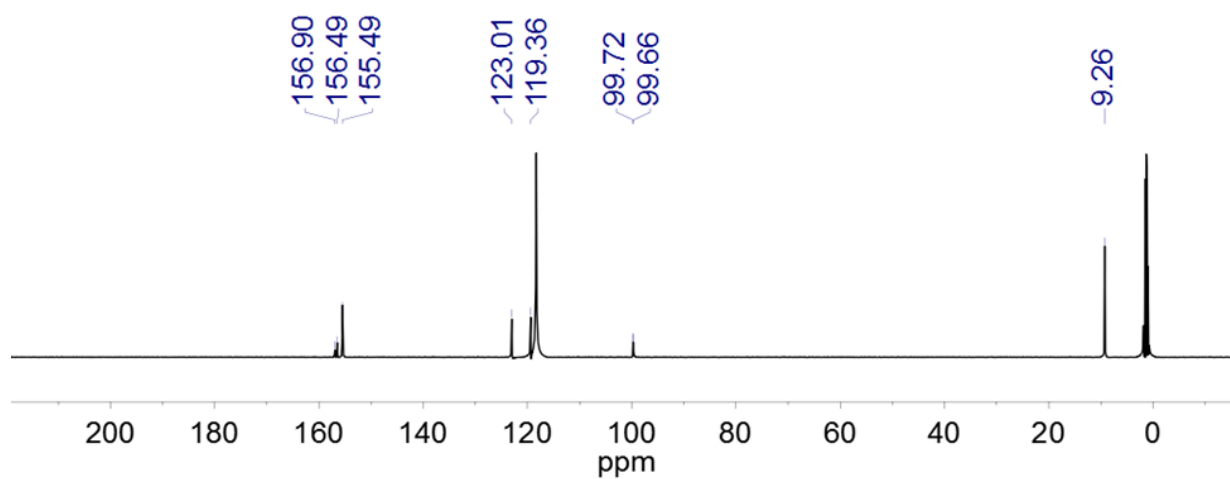

Figure 5. ^{13}C{^{1}H} NMR spectrum (126 MHz, CD$_3$CN) of **1**.
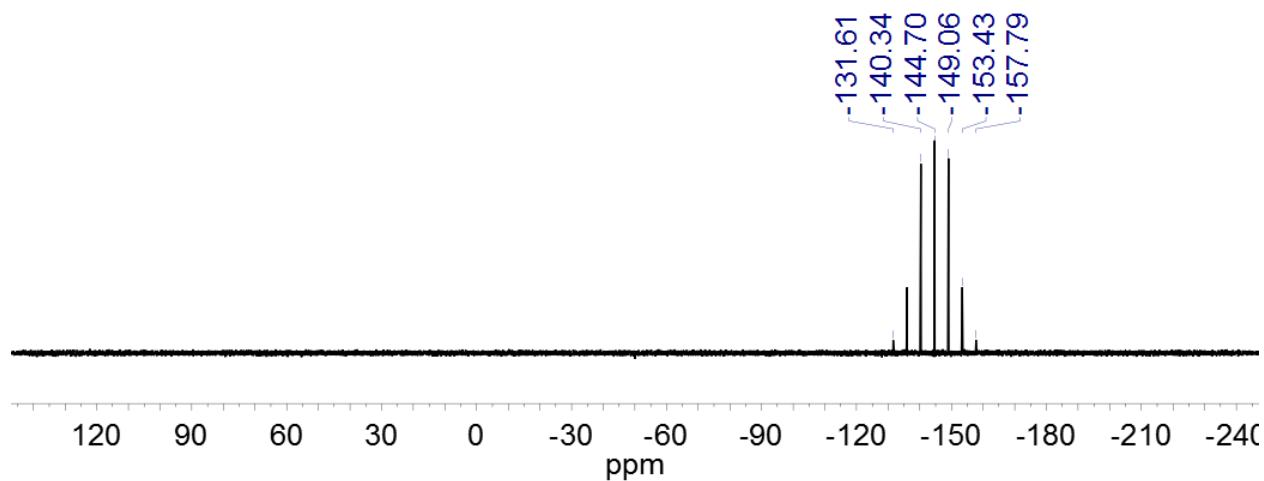

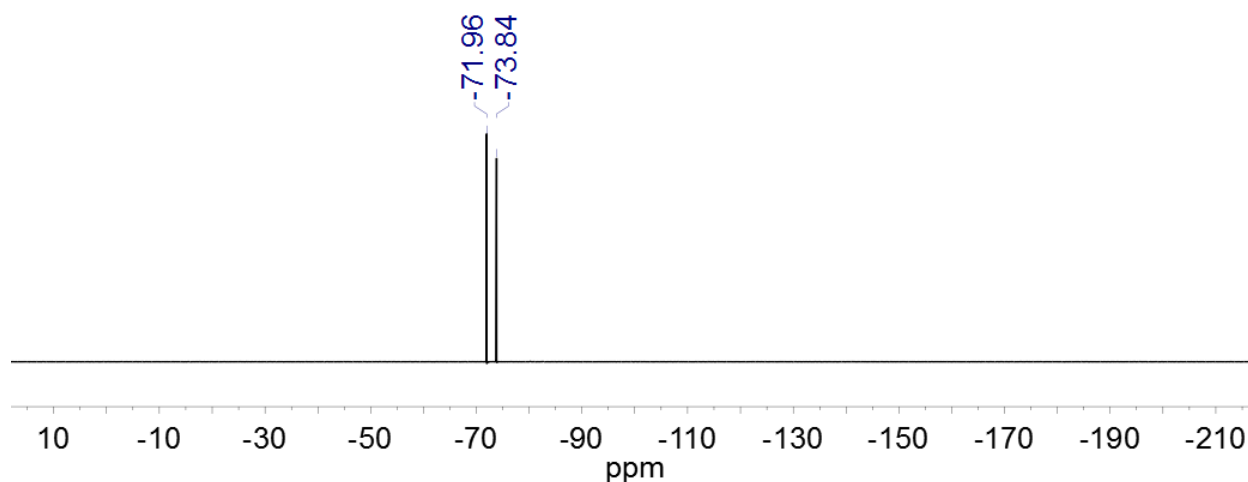**Figure 6.** ^{31}P{^{1}H} NMR spectrum (162 MHz, CD$_3$CN) of **1**.

16

Figure 7. ^{19}F NMR spectrum (376 MHz, CD$_3$CN) of **1**.

Vapor diffusion of diethyl ether into a concentrated acetonitrile (MeCN) solution of **1** yielded orange crystals suitable for single-crystal X-ray diffraction (XRD) studies (see Figure 8). The geometry at the rhodium center is pseudo-octahedral, with a first coordination sphere around the metal center containing [η^5-Cp*], [κ^2-$^{4,4'\text{-}NO2}$bpy], and a bound chloride anion (see Figure 8). The geometry and metal-ligand distances do not differ significantly from other structures of [Cp*Rh^{III}] complexes containing 4,4'-disubstituted-2,2'-bipyridyl ligands.[19] However, only a limited number of XRD datasets are available in the Cambridge Structural Database for metal complexes of $^{4,4'\text{-}NO2}$bpy, and our structure of **1** is the first structure obtained with rhodium.[20] In the structure of **1**, as in most other of structures containing $^{4,4'\text{-}NO2}$bpy, the (NO$_2$) groups are approximately co-planar with their partnered pyridine rings. In fact, of the seven total structures of $^{4,4'\text{-}NO2}$bpy itself,[21] or those containing $^{4,4'\text{-}NO2}$bpy,[22] only one of these has a O–N–C–C torsion angle greater than 13°. The observed co-planarity of the NO$_2$ groups and the pyridine rings suggests that there is likely strong electronic communication between these substituents and the π system of bipyridine. Therefore, we turned to electrochemical methods to establish the influence of the nitro groups on the electrochemical properties of the metal complex.
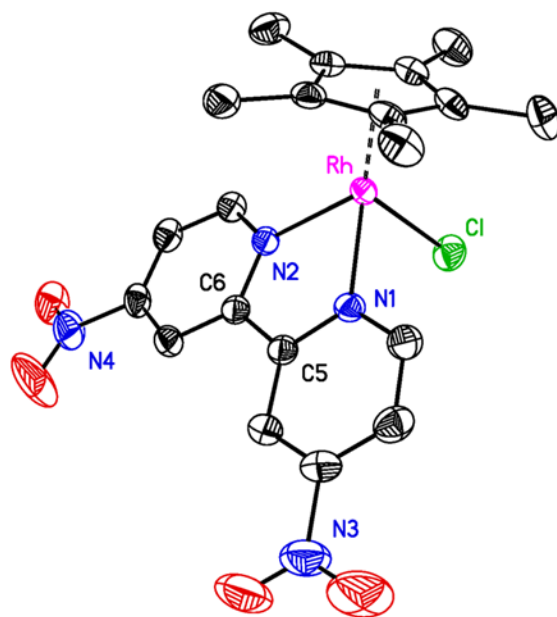
Figure 8. Solid-state structure (XRD) of **1**. H atoms, PF_6^- counteranion, and one co-crystallized MeCN molecule omitted for clarity. Displacement ellipsoids are shown at 50% probability. Single-crystal diffraction data were collected with a Bruker APEX-II CCD diffractometer. CCDC entry 1842459 contains the supplementary crystallographic data for compound **1**.

Cyclic voltammograms (CV's) of **1** (ca. 1 mM) were collected in THF solution containing 0.1 M tetrabutylammonium hexafluorophosphate ($[nBu_4N]^+[PF_6]^-$) as supporting electrolyte. Beginning at oxidizing potentials, **1** displays a manifold of four reduction events (see Figure 9) that onset around –1 V versus the ferrocenium/ferrocene couple (denoted hereafter as $Fc^{+/0}$). The key parameters associated with each of these four reduction events are summarized in Table 1. If the switching potential for the return anodic sweep is set at –2.2 V, the first three reduction events appear to be quasi-reversible with well-defined, clean return anodic waves. However, if the switching potential is set at a more negative value of –2.6 V, the fourth reduction wave is clearly visible. This fourth reduction, however, is not accompanied by a clean return oxidation wave, suggesting that one or more significant chemical reactions may follow injection of a fourth electron into the rhodium complex. Interrogation of the scan rate dependence of the both the cathodic and anodic peak currents for the first three observed redox processes reveals a linear dependence

18

between the peak potential and the square-root of the scan-rate (see SI, Figures S9-S11). This indicates that all the oxidized and reduced forms of the complex undergoing reduction and oxidation are freely diffusional in solution, and homogeneous.

We also carried out cyclic voltammetry of **1** in acetonitrile electrolyte, and consistently observed a similar manifold of reduction events (see Appendix 1, Figure S6). Specifically, three quasi-reversible reductions are followed by a virtually irreversible reduction.[23] However, we conducted most of our studies in THF electrolyte, as the complex typically yielded a better response under these conditions.
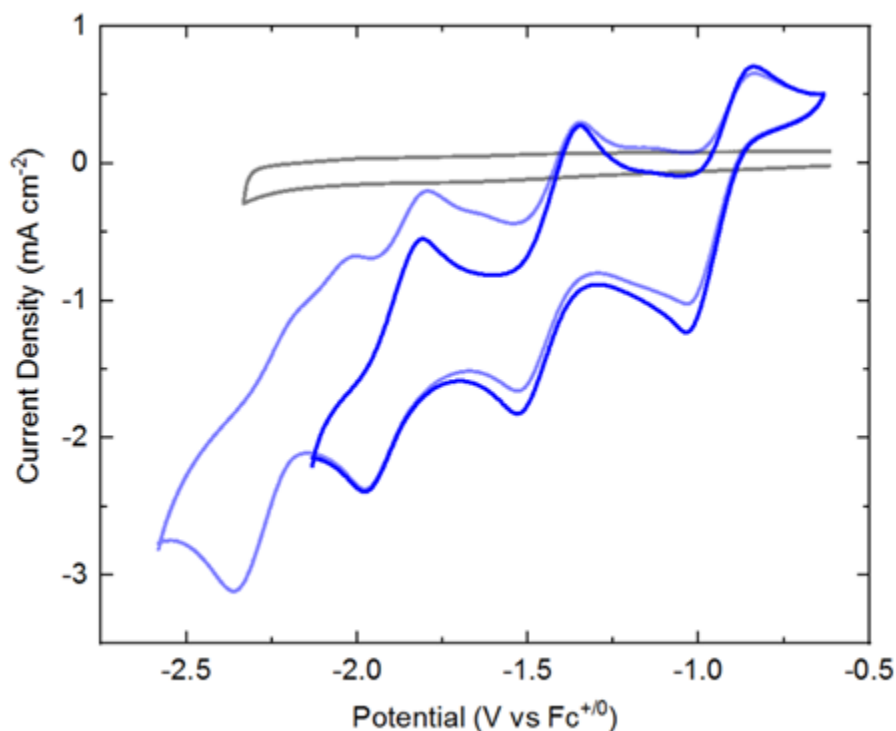
Figure 9. Cyclic voltammograms of **1**. Scan rate: 100 mV/s. Dark blue line: Cathodic sweep from ca. –0.6 V to a switching potential of –2.2 V and returning to –0.6 V. Light blue line: Cathodic sweep from ca. –0.6 V to a switching potential of –2.6 V and returning to –0.6 V. Gray line: electrolyte-only blank. Conditions: [**1**] ≈ 1 x 10^{-3} M; electrolyte: 0.1 M ($[nBu_4N]^+[PF_6]^-$) in THF.

Table 1. Cyclic voltammetry data for **1**. Conditions: [**1**] = 10^{-3} M; scan rate: 100 mV/s; electrolyte: 0.1 M ([nBu$_4$N]$^+$[PF$_6$]$^-$) in THF.

Redox event	$E_{1/2}$ (V)	ΔE_p (V)	$E_{p,c}$ (V)	$E_{p,a}$ (V)
A	–0.94	0.20	–1.04	–0.84
B	–1.44	0.18	–1.53	–1.35
C	–1.89	0.17	–1.98	–1.81
D	-	-	–2.36	-

In the cyclic voltammetry shown in Figure 9, the peak heights of the reduction processes appear to be similar, suggesting that the same number of electrons are transferred during each event. However, as the individual reduction events are relatively closely spaced, estimation of the appropriate background-corrected peak heights could be challenging. Therefore, differential pulse voltammetry (DPV) was carried out to quantitatively examine the number of electrons transferred in each event. For this determination, we prepared a solution containing a 1:1 mixture of ferrocene (Cp$_2$Fe) and **1** in THF containing 0.1 M ([nBu$_4$N]$^+$[PF$_6$]$^-$) supporting electrolyte and collected a differential pulse voltammogram from +0.5 V to –2.6 V (see Appendix 1, Figure S8). In addition to the one-electron process corresponding to the Fe^{III}/Fe^{II} couple of ferrocene, we observe four closely spaced and reasonably well resolved processes over a range similar to that seen for **1** in cyclic voltammetry. The areas of the four processes measured for **1** and that of Cp$_2$Fe were fit to Gaussian profiles, and comparison of the peak areas to that of the internal ferrocene standard confirms that one electron is indeed transferred in each event (see SI, Table S3 for peak area ratios).

The electrochemical response of complex **1** sharply contrasts with the behavior commonly encountered for other [Cp*Rh^{III}] complexes. Most other chloride-bound complexes in this family containing other diimine,[6,7] diphosphine,[19] or hybrid phosphine-monoimine ligands,[25] undergo a net two-electron reduction that appears as a single redox process in cyclic voltammetry experiments. As described in the Introduction (*vide supra*), this ECE-type electrochemical

response implies that a chemical reaction follows the initial reduction of the metal complex and leads to formation of a species that undergoes immediate transfer of a second electron.[24] Disentangling the nature of the elementary steps in this chemistry is of high interest, as the resulting 2e⁻-reduced complexes often undergo subsequent reactivity with protons. Notably, our recent work examining the case of a [Cp*Rh] complex bearing the hybrid 8-(diphenylphosphino)quinoline (PQN) ligand suggests that the first reduction of [Cp*Rh^{III}(PQN)Cl]PF$_6$ is rhodium-centered, and leads to ejection of the chloride ligand at the Rh^{II} oxidation state.[25] The electrochemical behavior of the [Cp*Rh] complex supported by the dimethyldipyridylmethane (Me$_2$dpma) ligand is also consistent with initial metal-centered reduction.[18]

Synthesis and Characterization of 2

Therefore, to investigate the nature of the first reduction of **1**, we targeted preparation of the singly reduced product. In accord with the clean, one-electron reduction of **1** observed by cyclic voltammetry, treatment of a THF suspension of **1** with cobaltocene ($E° \approx -1.3$ V, 2 equiv.)[26] results in an immediate color change from bright yellow to a deep shade of forest green. Following stirring for 10 minutes and subsequent removal of all volatiles under vacuum, the reduction product **2** was extracted with THF and isolated as a dark green solid. Characterization of **2** by ^{1}H NMR (Appendix 1, Figure S1) reveals a loss of all resonances associated with **1**, including those of the [κ^2-($^{4,4'-}$^{NO2}bpy)] ligand in the aromatic region and that associated with [η^5-Cp*] in the aliphatic region. The disappearance of these resonances and lack of new peaks associated with diamagnetic material is consistent with generation of a paramagnetic complex, as would be expected for a 1e⁻ reduction of **1** as observed in cyclic voltammetry. A small impurity of [Cp$_2$Co]$^+$ ($\delta = 5.66$ ppm) is observed

in NMR spectra of isolated samples from the reduction of **1**, but could not be removed due to the similar solubility profiles of **2** and cobaltocenium.

To further characterize **2**, we turned to electron paramagnetic resonance spectroscopy. Prior to reduction, **1** is a low-spin rhodium(III) complex with a d^6 configuration and $S = 0$. The cobalt(II) reductant (Cp$_2$Co) used to generate **2** has a d^7 configuration and is a $S = 1/2$ species, displaying the distinctive spectrum (consistent with literature) shown as the purple line in Figure 10. This spectrum displays hyperfine coupling to the $I = 7/2$ cobalt nucleus. In contrast, the spectrum of **2** isolated as described above reveals a relatively narrow and isotropic signal with a center crossing point at $g = 2.006$ ($H = 3341$ G). Although **2** could be considered to be a formal rhodium(II) species, the sharp and isotropic spectrum is instead consistent with an organic radical—in this case, predominant localization of unpaired electron density on the $^{4,4'-NO2}$bpy ligand. Thus, **2** can be most appropriately considered as a rhodium(III) complex with a bound $^{4,4'-NO2}$bpy$^{\bullet-}$. Retention of this ligand radical in the first coordination sphere of the rhodium center is consistent with both the quasi-reversible CV studies (*vide supra*) and spectroelectrochemical work that confirms the chemically reversible interconversion of **1** and **2** (*vide infra*) on the seconds to minutes timescale. Moreover, the lack of resolved hyperfine coupling to the $I = \frac{1}{2}$ ^{103}Rh nucleus (100% abundance) in **2** corroborates assignment of the reduced metal species as having unpaired electron density that is localized primarily on $^{4,4'-NO2}$bpy. Notably, the trace impurity of [Cp$_2$Co]$^+$ present in samples of isolated **2** does not contribute to the EPR spectrum shown in Figure 10, as [Cp$_2$Co]$^+$ is an $S = 0$ low-spin cobalt(III) complex.
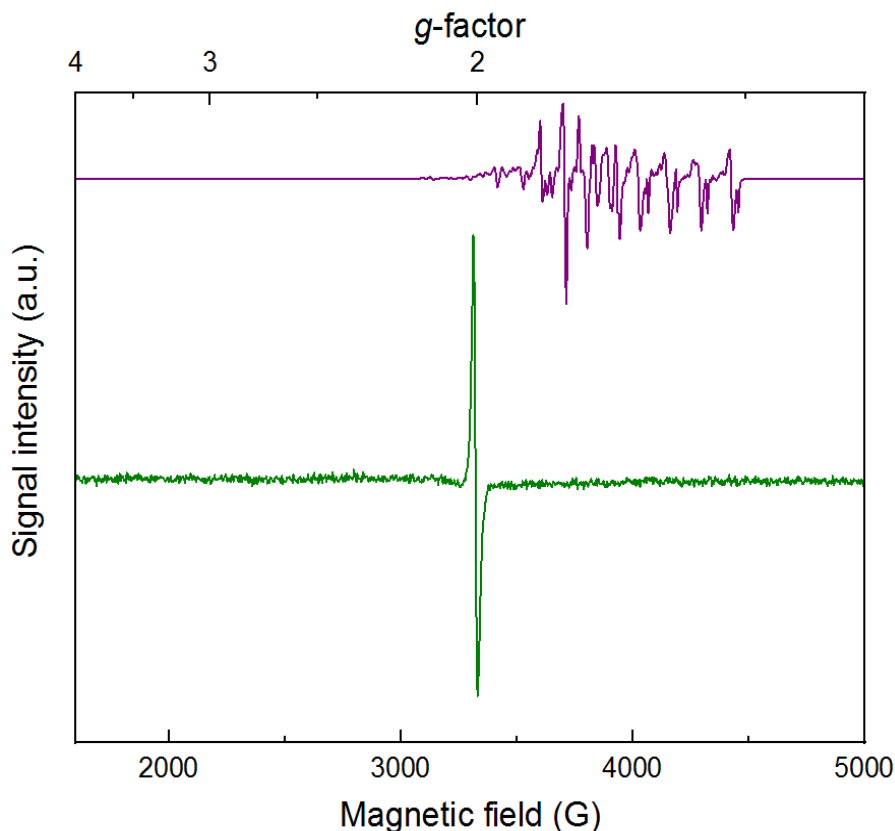
Figure 10. X-band Continuous Wave (CW) EPR spectrum of **2** (green line) and cobaltocene (purple line). Conditions: $T = 10$ K; modulation amplitude $= 2.0$ G; time constant $= 20.5$ ms; [**4**] $= 10^{-3}$ M.

Few examples of formal rhodium(II) complexes have been observed by EPR.[27] Localization of unpaired electron density in orbitals with increased Rh(II) character would be expected to result in a significantly more anisotropic spectrum than that observed for **2**, with larger g-value shifts and resolved hyperfine coupling to the metal nucleus. The experimental data for **2** compare well with data that we have recently obtained on [Cp*Rh(bpy$^{\bullet-}$)Me]^0 and [Cp*Ir(bpy$^{\bullet-}$)Me]^0 compounds.[28] Specifically, these methyl complexes display narrow rhombic spectra centered near $g \approx 2.0$. This greater rhombicity arises from hyperfine couplings to the $I = 1/2$ Rh$^{\text{III}}$ and $I = 3/2$ Ir$^{\text{III}}$ centers in these compounds, contrasting with the case of virtually ligand-centered **2**. Thus, we conclude that the unpaired electron density on $^{4,4'\text{-NO2}}$bpy$^{\bullet-}$ is contained in molecular

orbitals with very little character arising from rhodium, a phenomenon likely driven by the presence of the strongly electron-withdrawing nitro groups on $^{4,4'-NO2}$bpy.

To gain further insight into the $^{4,4'-NO2}$bpy-localization of electron density arising from the first reduction of **1**, we turned to electronic absorption spectroscopy (see Figure 11 and Appendix 1, Figure S3). The spectrum of **1** is unremarkable and displays features consistent with most rhodium(III) complexes; **1** is a yellow solid, and the UV-visible absorption spectrum reflects this with a relatively intense (ca. 5000 M^{-1} cm^{-1}) band trailing into the visible around 400 nm. Isolated **2** displays a very different profile, with distinctive new features in the visible-NIR region (λ_{max} values at 694 nm, 860 nm, and 945 nm with molar absorptivities of 13000, 6100, and 7800 M^{-1} cm^{-1}, respectively). Consistent with the observed forest-green color of **2**, a weaker absorption band is retained at lower wavelength (420 nm, 5200 M^{-1} cm^{-1}) and thus transmits predominantly green light between these bands. The absorption bands in the 800-1000 nm range are similar to examples of both free bpy$^{\bullet-}$ and metal complexes ligated by [bpy$^{\bullet-}$].[29,30] Analogous data is not available from prior work for dnbpy$^{\bullet-}$, although similar features are measured for the doubly reduced form of [Cp*Rh($^{4,4'-CF3}$bpy)Cl][PF$_6$], which possesses significant reduced-ligand character.[19] Thus, both EPR and electronic absorption data are consistent with assignment of $^{4,4'-NO2}$bpy-centered reduction in **2**.
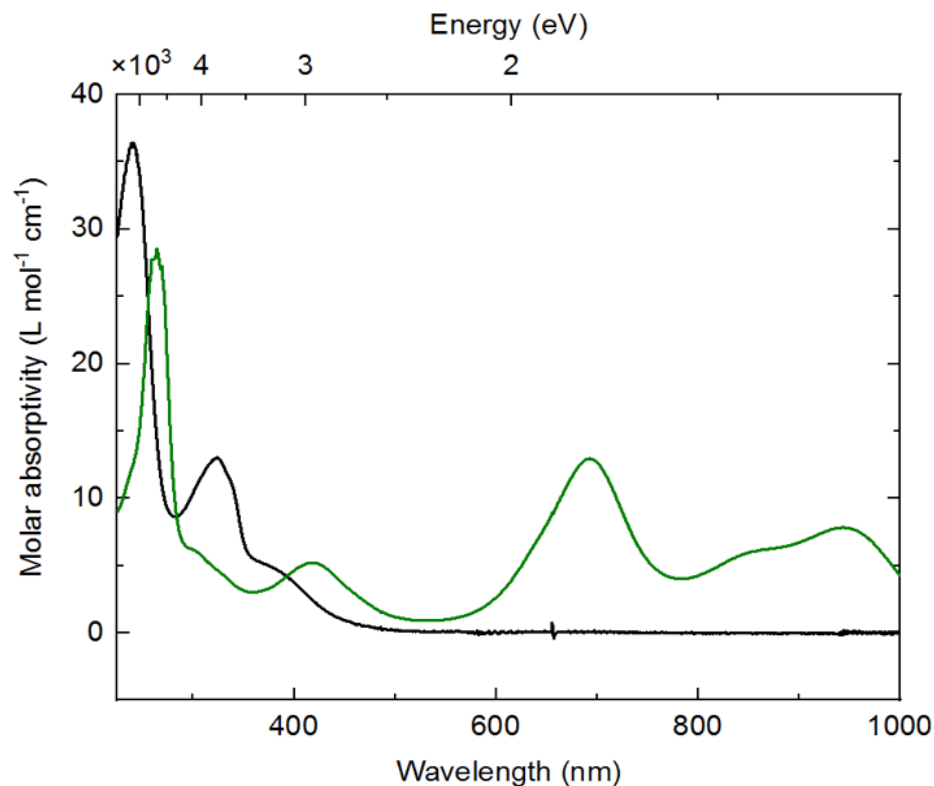
Figure 11. Electronic absorption spectra of **1** (black line) and **2** (green line). Conditions: [**1**] ≈ [**2**] ≈ 10^{-5}; solvent: tetrahydrofuran.

Further Electrochemical and Spectroelectrochemical Studies of 1 and 2

Metal-centered reduction of [Cp*Rh^{III}] complexes is associated with ejection of monodentate ligands such as chloride from the first coordination sphere. This phenomenon is driven by formation of transient, 19e$^-$ Rh^{II} intermediates upon reduction that release the monodentate ligand to form more stable 17e$^-$ species.[25] The assignment of ligand-centered reduction of **1** thus prompted us to explore whether analogous reactivity takes place here. To test this, we performed cyclic voltammetry on **1** in acetonitrile containing 0.1 M ([nBu$_4$N]$^+$[Cl]$^-$) as supporting electrolyte. The first reduction of **1** remains unchanged from the case of ([nBu$_4$N]$^+$[PF$_6$]$^-$), showing a quasi-reversible appearance. However, the appearance of the second reduction of **1** (or reduction of **2**) is different, showing two peaks on the cathodic sweep ($\Delta E \approx 175$

mV) and a single peak on the anodic sweep (see Appendix 1, Figure S11). This is consistent with the formation of both the cationic solvento complex [Cp*Rh(dnbpy$^{\bullet-}$)(NCMe)] and a neutral chloride complex [Cp*Rh(dnbpy$^{\bullet-}$)Cl] following the first reduction, when the electrolyte contains a 100-fold excess of chloride. Thus, under conditions where chloride is not found in excess (Figure 9), we propose that reduction of **1** leads to generation of the 18e$^-$, cationic [Cp*Rh($^{4,4'-NO2}$bpy$^{\bullet-}$)(NCMe)][PF$_6$] complex. Consistent with this significant coupled chemical reaction, the peak-to-peak separation ($\Delta E_p \approx 200$ mV in THF, 90 mV in MeCN) associated with reduction of **1** to **2** in ([nBu$_4$N]$^+$[PF$_6$]$^-$) is significantly larger than those associated with the following two reductions (180, 170 mV in THF; 70, 70 mV in MeCN) (see Table 1 and Table S1 in SI). Completing our proposed model for the electrochemistry, reduction of **2** leads to a single product, on the basis of the single anodic wave observed at −1.35 V in THF (Figure 9) and −1.19 V in MeCN (see Appendix 1, Figure S6). As this species is rather electron-rich, we speculate that the reduction of **2** produces [Cp*Rh(dnbpy)]^0; however, further assignments regarding this compound are beyond the scope of this study.

To gain further insight into the reductions of **1** that are readily accessible via electrochemical methods, we turned to UV-visible spectroelectrochemistry. We took the approach of *in situ* generation and detection of **2** and other reduced forms of **1** by use of a short-pathlength cuvette cell placed in the beam path of a UV-visible spectrophotometer for real-time data collection during working electrode polarization. With the working electrode polarized at −0.63 V vs. Fc$^{+/0}$, the spectrum of **1** contained in the cell (electrolyte: 0.1 M ([nBu$_4$N]$^+$[PF$_6$]$^-$) in THF) is virtually identical to that of **1** in pure THF free from supporting electrolyte. However, upon polarization at −1.31 V, the spectrum changes dramatically (Figure 12, panel a), with new features appearing that correspond to those of rhodium(III) bound to reduced $^{4,4'-NO2}$bpy$^{\bullet-}$. Notably, isosbestic points were

measured at 312 and 352 nm (Appendix 1, Figure S18), consistent with clean conversion of **1** to **2** in THF solution under the spectroelectrochemical conditions. However, close comparison of the spectroelectrochemical data (collected in THF electrolyte containing 0.1 M ([nBu$_4$N]$^+$[PF$_6$]$^-$) and the earlier UV-visible data collected on **2** (in pure THF) reveals that the λ_{max} values are slightly shifted in the two cases (417 vs. 418, 699 vs. 693, 865 vs. 860, 946 vs. 944 nm, respectively) (see Appendix 1, Figure S24). These minor differences are consistent with ligand exchange of chloride in favor of THF, facilitated by 0.1 M ([nBu$_4$N]$^+$[PF$_6$]$^-$), as similar spectral changes accompany exchange of halide ligands for coordinated solvent (e.g., MeCN) in other rhodium(III) complexes.[20,25]
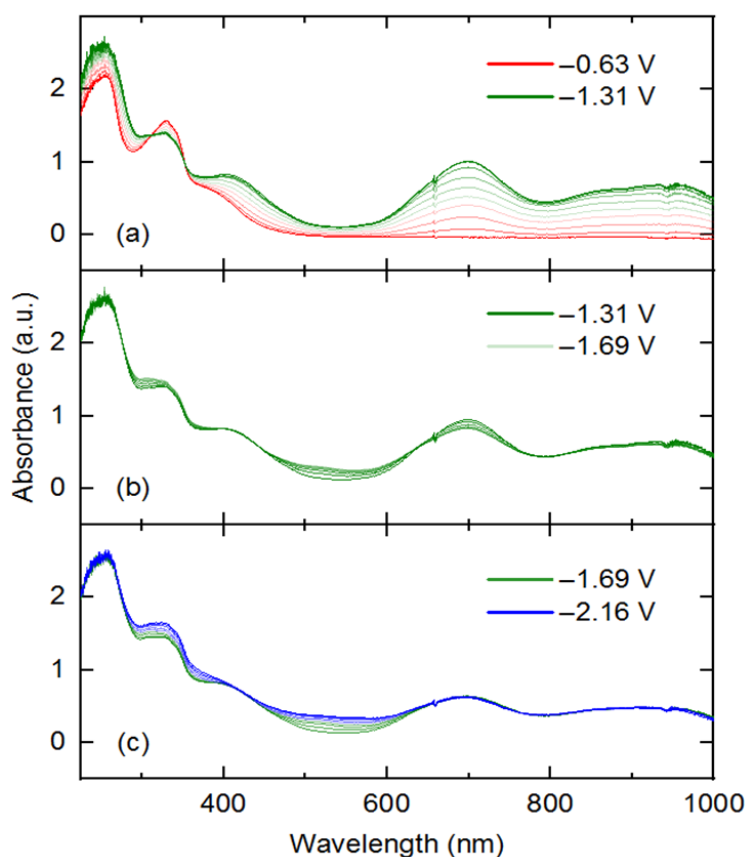
Figure 12. UV-visible-NIR absorption spectra obtained during spectroelectrochemical studies as described in the main text. Initial potentials for each experiment were –0.63 V (panel a), –1.31 V (panel b), and –1.69 V (panel c). Final potentials were –1.31 V (panel a), –1.69 V (panel b), and –2.16 V (panel c). Final potential was held until no spectral changes were reached, indicating full conversion of the thin-layer region to the desired form of the complex.

To confirm the apparent chemical reversibility observed in cyclic voltammetry for transformation of **1** to **2** (Figure 9) and **2** to **1** (see Appendix 1, Figure S12), an experiment was also carried out with an initial potential of –1.31 V and final potential of –0.63 V in an electrolyte solution prepared with **2** (see Appendix 1, Figure S22). In this experiment, the evolution of the spectral features detected in the experiment shown in Figure 12a were essentially reversed. This is consistent with clean regeneration of complex **1** from **2** upon electrochemical re-oxidation (isosbestic points at 312 and 352 nm).

Further potential excursions show spectral changes associated with the further reductions of **1**. A potential jump from –1.31 to –1.69 V results in fairly minor changes to the UV-visible spectrum (Figure 12b). Clear isosbestic points were observed at 437, 638, and 800 nm for this reduction event, corresponding to increased spectral absorption toward the blue region (522 nm) and slightly attenuated absorption intensity (peak at 699 nm) toward the longer wavelengths. A further potential excursion to –2.16 V (Figure 12c) results in further increases in absorption toward shorter wavelengths (325 and 522 nm), and virtually no changes in absorption at the longer wavelengths (isosbestic point at 420 nm). Based on the isosbestic behavior, we confirm the interconversion of single species implied by the electrochemical studies carried out in ($[nBu_4N]^+[PF_6]^-$).[18,25]

However, final potential excursion to –2.56 V results in non-isosbestic spectral evolution (Figures 12c and Appendix 1, Figure S21), suggesting formation of multiple speciation products or decomposition of the four-electron reduced species generated from **1**. This behavior is consistent with the irreversible reduction observed at –2.36 V in the voltammetry of **1** and confirms that the quadruply reduced form of **1** is unstable under electrochemical and spectroelectrochemical conditions. Study of the electronic structure of these further reduced intermediates is deserving of

future work, especially focusing on the localization of each reduction (metal, ligand, both) and coordination geometry of rhodium (presence or absence of bound chloride or solvent). Computational approaches could be of great use here, as well as further spectroscopic and synthetic/structural investigations.

H$_2$ Evolution Catalysis Studies of 1

As reduction of most [Cp*Rh] complexes bearing diimine-type ligands in the presence of acid can give rise to catalytic H$_2$ production, we examined electrochemical reduction of **1** in the presence of acid to check for formation of H$_2$ (as has been measured for both [Cp*Rh($^{4,4'-CF3}$bpy)Cl][PF$_6$] and **4**). We conducted these studies with **1** in MeCN electrolyte (in order to rely on the well-defined pK_a scale that is available in this solvent).[31,32] Addition of 1 atm of H$_2$ gas to the headspace of the electrochemical cell results in no major changes to the voltammogram profile, confirming that **1** does not readily serve as a catalyst for H$_2$ oxidation (see Appendix 1, Figure S13). However, addition of 15 equiv. of buffered Et$_3$NH$^+$/Et$_3$N results in a fully irreversible voltammogram profile, and a modest increase in current density across a broad potential range from –1 V to around –2 V (see Appendix 1, Figure S13). Beyond –2 V, there is a significant enhancement in the current flowing in the voltammetry, although at these potentials similar current enhancement is also observed for a rhodium-free electrolyte solution containing only buffered acid.

Bulk electrolysis was then carried out to ascertain the fate of the reducing equivalents transferred to the solution under these acidic conditions. Electrolysis was carried out at –1.75 V, prior to the onset of significant background currents, to reveal the behavior of the reduced metal complexes with acid. In a rhodium-free control experiment, 17.2 C of charge were passed through

the electrochemical cell, and a fairly significant amount of H_2 was generated corresponding to 87% Faradaic efficiency (product H_2 measured by gas chromatography). The analogous electrolysis carried out with **1** (Appendix 1, Figure S14) leads to passage of only 8.2 C of charge, corresponding to 1.95 e– per Rh center. A Faradaic yield of H_2 of only 5% was measured by gas chromatography, confirming that **1** does not serve as an effective (pre)catalyst for H_2 evolution under these conditions.

During electrolysis, the solution of **1** remains homogeneous, but turns a dark red color. To investigate, aliquots of the working solution were removed from the cell following electrolysis, the solvent removed *in vacuo*, and ^1H NMR data collected in CD_3CN to ascertain the identity of products formed by reaction of reduced **3** with acid. The ^1H NMR data reveal that several (≥3) diamagnetic [4,4'-NO2]bpy containing species are generated, based on the presence of multiple sets of [4,4'-NO2]bpy-like resonances in the aromatic region (see Appendix 1, Figure S15). However, no metal hydride signals were observable in the upfield region near –10 ppm (Appendix 1, Figure S16),[24,25] nor were the characteristic signals corresponding to formation of [Cp*H] (e.g., a doublet near 0.5 ppm) detected (Figures S15b and S15c in SI).[23,32] Thus, we conclude that decomposition accompanies reduction and protonation of **1**, resulting in formation of multiple products but very little H_2.

Discussion

The observation of four one-electron reduction events with complex **1** contrasts with the single two-electron, ECE-type reduction[24] events measured for most other diimine and diphosphine complexes of [Cp*Rh].[6,8,19,25] Results from our laboratory suggest that the first reduction is rhodium metal-centered in most of these cases.[18] Thus, initial metal-centered reduction

generates a transient 19e$^-$ rhodium(II) complex that undergoes subsequent ligand *dissociation* (to a 17e$^-$ species) and further reduction. **1** circumvents this more common reactivity by undergoing a first, ligand-centered reduction that leads only to *exchange* of bound chloride or solvent. As a side note, we have recently chemically prepared an analogous formally rhodium(II) complex bearing a bis(pyridyl) ligand; this complex is a metal-centered radical that circumvents further reduction through use of the bis(pyridyl) ligand that enforces a six-membered metallocyclic ring.[18] Here, we conclude that inclusion of the easily reduced dnbpy ligand and retention of a monodentate ligand in **2** contribute to the ability of the complexes to undergo sequential, one-electron reductions.

Our formulation of **2** as a ligand-centered radical is consistent with prior work from Yellowlees's group[33] on the nature of reduced species formed by reduction of nitrated bpy complexes of Pt^{II}. Specifically, their group found that the LUMO of Pt($^{4,4'-NO2}$bpy)Cl$_2$ is localized on the $^{4,4'-NO2}$bpy ligand; on the basis of exhaustive EPR spectroelectrochemistry and computational studies, they further assigned the radical in Pt($^{4,4'-NO2}$bpy$^{\bullet-}$)Cl$_2$ to be localized on a single 4-NO$_2$-pyridyl ring within the complex. The Pt compounds in their study displayed rich hyperfine structure in EPR spectra, enabling this assignment. In our EPR data for **2**, however, no such fine structure is observable. Thus, further work is needed to distinguish details of the exact localization of unpaired electron density within the conjugated $^{4,4'-NO2}$bpy system.

Cp*Rh(bpy) undergoes reaction with protons to form [Cp*H] species that are active intermediates in catalytic H$_2$ production.[34] Therefore, the observation of virtually no H$_2$-generating reactivity of reduced forms of **1** with protons is interesting from the perspective of understanding the structure and bonding features that engender catalysis involving H-atom transfer[35] from [Cp*Rh] complexes. In the chemistry of most [Cp*Rh] complexes, apparently metal-centered

reduction is followed by reactivity with protons to form either [Cp*H] complexes[35] or stable rhodium(III) hydride species.[23,25] Based on electrochemical studies of **1** in the presence of Et_3NH^+, we conclude that one or more of the reduced forms of **1** undergo reaction with protons, but these do not lead to effective H_2 generation.

However, involvement of ligand-centered orbitals in reduction events does not necessarily preclude proton reactivity in [Cp*Rh] complexes; rather, our results suggest that the electron-donating and -withdrawing character of ligands on these frameworks must be carefully balanced to accommodate the intermediates that may arise during catalysis. This conclusion is well supported by the prior work implicating a delocalized HOMO across the metal and ligands in most reduced Cp*Rh(diimine) complexes, and the reactivity of the doubly reduced forms of **5** and [Cp*Rh($^{4,4'-CF3}$bpy)Cl][PF$_6$] with protons towards hydrogen evolution.

Conclusions

In this chapter, the preparation, characterization, and electrochemical properties of [Cp*Rh^{III}($^{4,4'-NO2}$bpy)Cl][PF$_6$] (**1**). This complex displays four one-electron reduction events in organic electrolytes, contrasting with prior work on a similar complex that showed no reductions in aqueous electrolyte. Spectroscopic studies show that the singly reduced complex **2** generated from **1** is best formulated as [Cp*Rh^{III}($^{4,4'-NO2}$bpy$^{\bullet-}$)(L)]$^+$ where L = chloride or solvent, depending upon the conditions of the experiment. Spectroelectrochemical studies suggest clean interconversion of the various reduced forms, as isosbestic behavior is obtained in the UV-visible spectra associated with controlled potential excursions. However, in contrast to other [Cp*Rh] complexes bearing diimine ligands, electrochemical studies of **1** in the presence of excess Et_3NH^+ show that reduction in the presence of this weak acid does not lead to H_2 production. Taken together, these studies show that [Cp*Rh] complexes, and the reactions that they undergo upon

electron transfer, are readily tunable by judicious selection of supporting ancillary ligands. Our ongoing work is examining this strategy to harness the useful properties of this family of compounds.

Chapter 2. Tuning the redox properties of [Cp*Rh] catalysts with monosubstituted

2,2′-bipyridyl ligands

This chapter is based upon work from an ongoing project that is in preparation for publication.

Introduction

As discussed in Chapter 1, it would be advantageous to store excess renewable energy in chemical bonds. Accomplishing that transition effectively requires having a low energy input and facile production of a useful chemical. Dihydrogen is a great example of one such product. First and foremost, it contains a highly energy-dense bond at approximately 436 kJ/mol.[1] Secondly, use of dihydrogen abounds: (1) it is one of two reactants used to generate ammonia in the Haber-Bosch process, which takes up over 1% of the world's energy supply,[36] (2) it is used in the hydrogenation of many household foods such as butter,[37] and (3) it is also a key component in rocket fuel.[38]

Notably, using electrical energy to directly generate H_2 from a solution containing protons is not efficient enough to be conducted on an industrial scale. Therefore, use of a catalyst is key to making electrochemical hydrogen evolution industrially viable. Kölle and Grätzel did important early work synthesizing [Cp*Rh] catalysts for this specific purpose.[6] Moreover, work on this system over the past 30 years has shown that these catalysts can be tuned to perform more or less efficiently than the parent complex by symmetrically substituting the bipyridyl motif.[8] However no information is available on non-symmetric substitutions of the bpy ligand within this framework. Motivated by this knowledge gap, this projects uses a divergent synthetic route to yield a series of 4-substituted bipyridines and examines how coordination of these ligands to the [Cp*Rh] platform results in changes to the characteristics of these candidate catalysts.

Divergent Synthesis

Strategic combination of a set of previously developed synthetic procedures from the literature enables a divergent synthesis route from which three 4-substituted bipyridines can be synthesized from a common precursor: 4-nitro-2,2′-bipyridine-*N*-oxide.[39,40,41,42] The synthetic

scheme in Figure 13 outlines the reactions necessary to access all three new [Cp*Rh] complexes bearing these non-symmetric ligands. Coordination of the ligands to the [Cp*Rh] platform was accomplished via known literature procedures.[17,18] Complex **5**, the parent 2,2′-bipyridyl complex, was available in our laboratory from work in other areas.

Synthesis of each compound was confirmed by NMR spectroscopy. Figures 14-17 show the ^{1}H, ^{13}C{^{1}H}, ^{31}P, and ^{19}F NMR spectra for Complex **3**. Due to the asymmetric nature of bipyridyl substitutions, seven unique resonances are observed in the aromatic region of the proton NMR (Figure 14). Each resonance integrates to one with respect to the most downfield signal. The methyl protons on the [Cp*] ring show up as a single resonance at approximately 1.7 ppm. Lack of other signals indicates there are no other diamagnetic Cp* or bpy-containing species present.
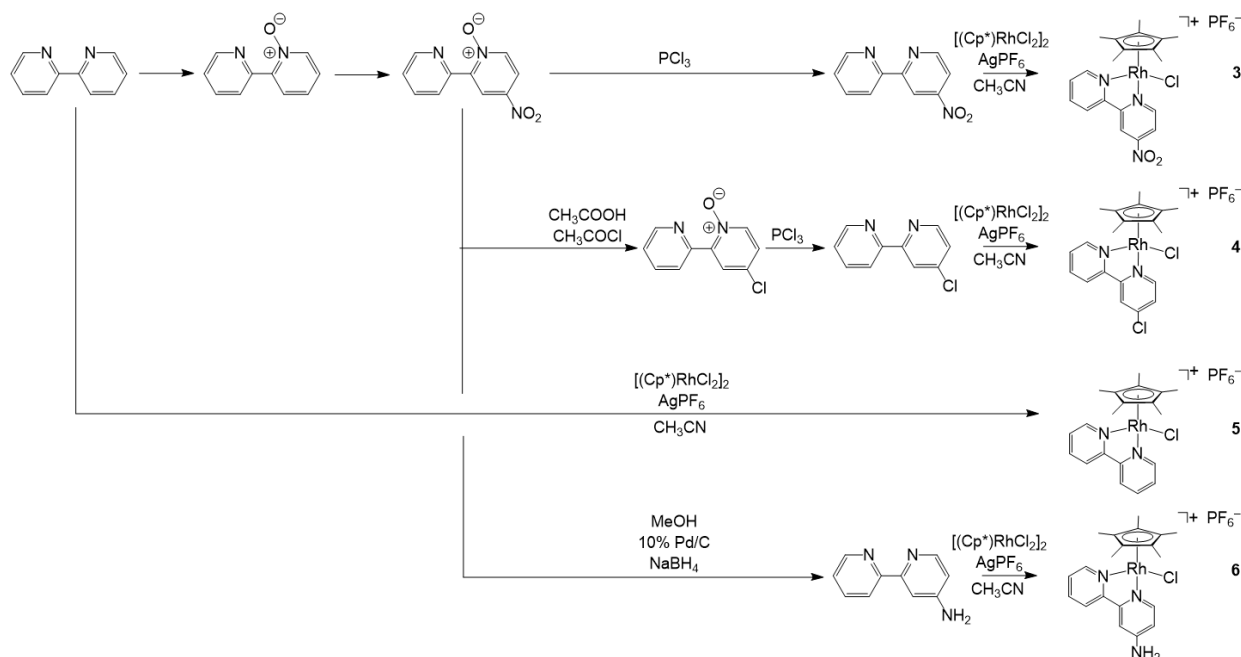
Figure 13. Synthetic scheme for preparation of C_1-symmetric [Cp*Rh] complexes.
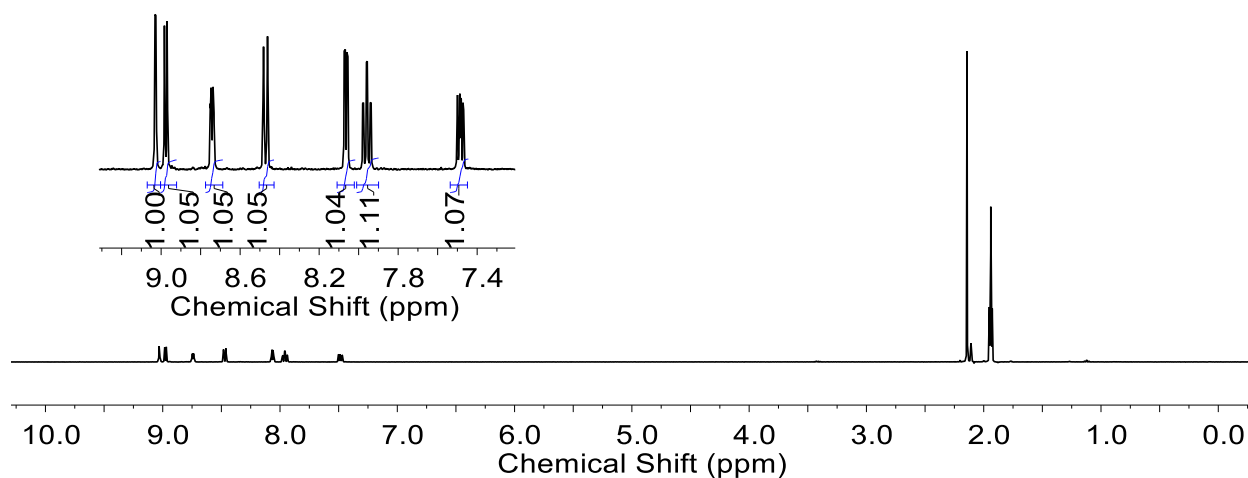
Figure 14. ^{1}H NMR spectrum of **3**.
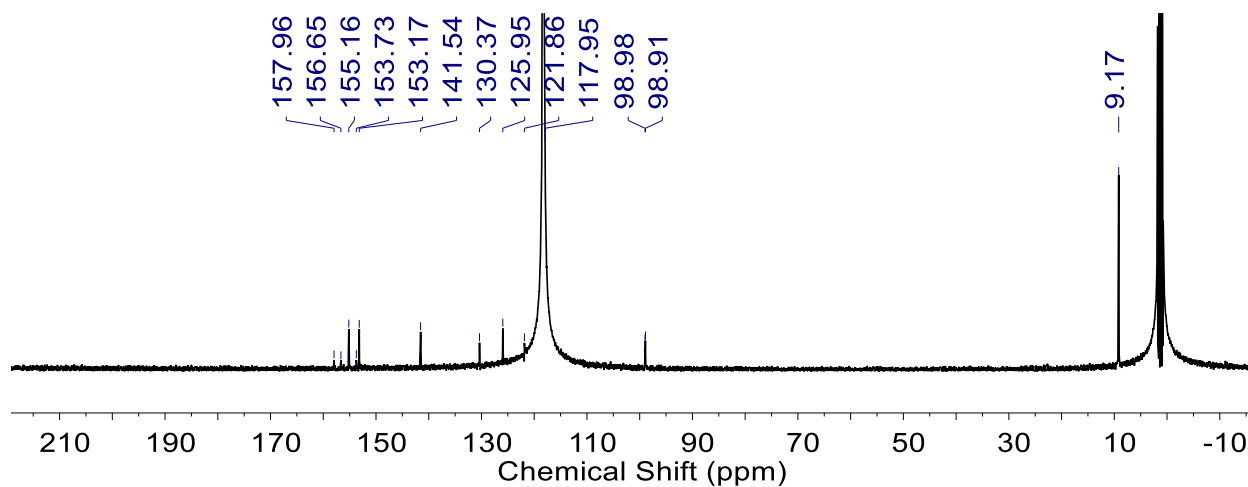
Figure 15. ^{13}C{^{1}H} NMR spectrum of **3**.
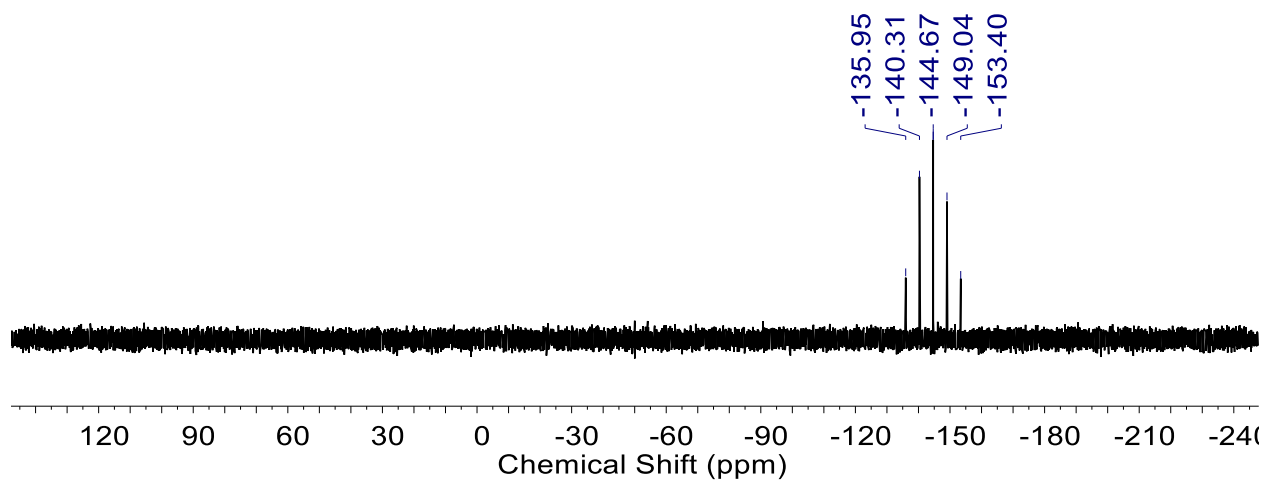
Figure 16. ^{31}P NMR spectrum of **3**.
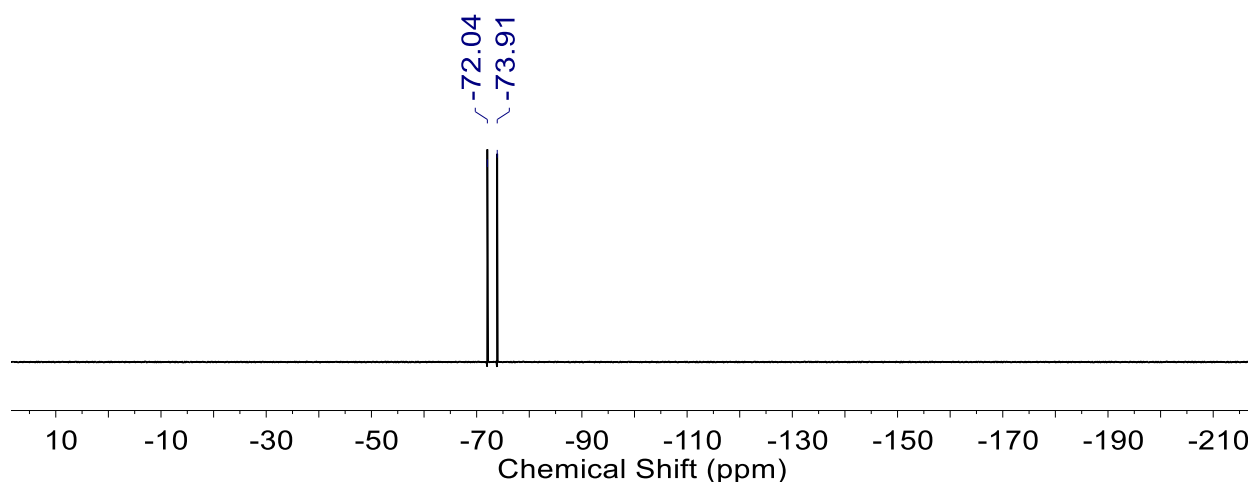
Figure 17. ^{19}F NMR spectrum of **3**.

Figures 18-21 and 22-25 show the ^{1}H, ^{13}C{^{1}H}, ^{31}P, and ^{19}F NMR spectra for Complex **4** and **6** respectively. Similarly to complex **3**, seven distinct resonances in the aromatic region correspond to the bipyridyl protons, and a single resonance in the aliphatic region between 1.6-1.8 ppm corresponds to the methyl protons on the [Cp*] ring. Mass spectrometric characterization of complex **3** is included in Figure S2 of Appendix 2. Small peaks slightly downfield of the major resonances in Figure 22 (^{1}H NMR) are indicative of a small amount of solvent-bound (rather than chloride bound) metal complex. Complex **6** is particularly susceptible to formation of a solvento species because the amino substituent inductively pushes electron density onto the rhodium metal center, weakening the Rh−Cl bond. In this case, the MeCN is a weaker σ-donor ligand than chloride.[43] This leads to a less electron-rich metal center and a slight downfield shift for both the aromatic protons and [Cp*] methyl protons.
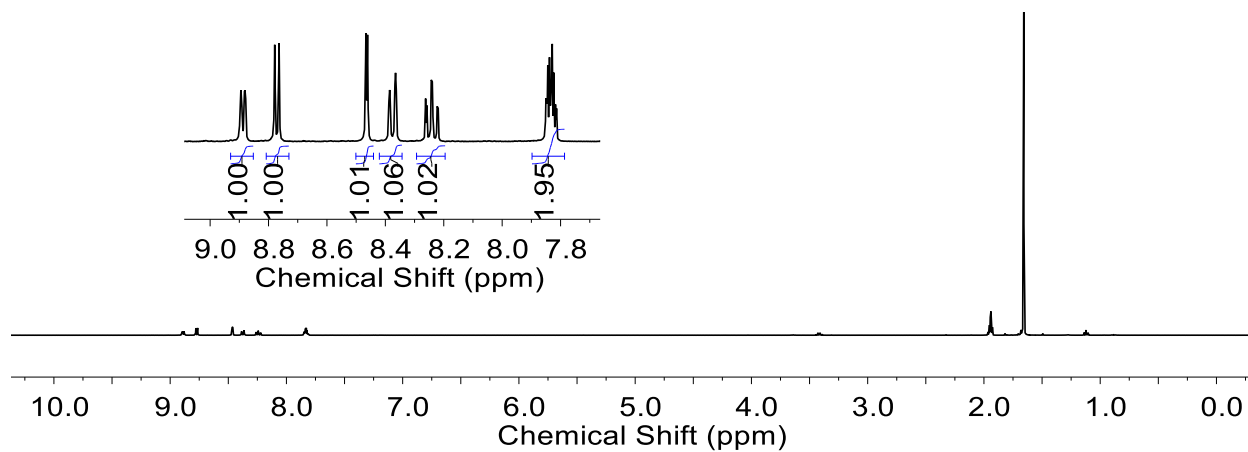
Figure 18. ^{1}H NMR spectrum of **4**.
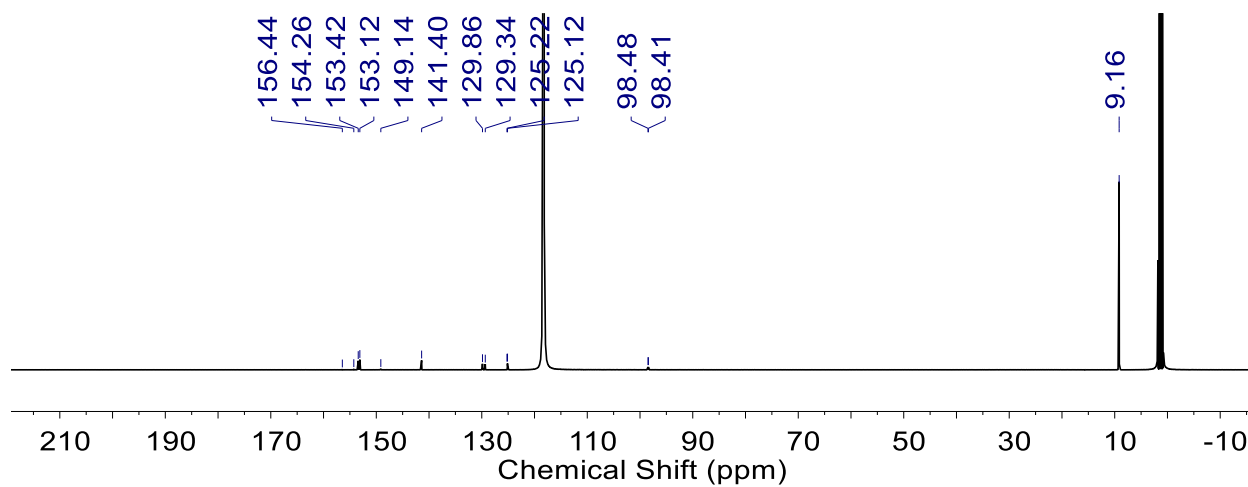
Figure 19. ^{13}C{^{1}H} NMR spectrum of **4**.
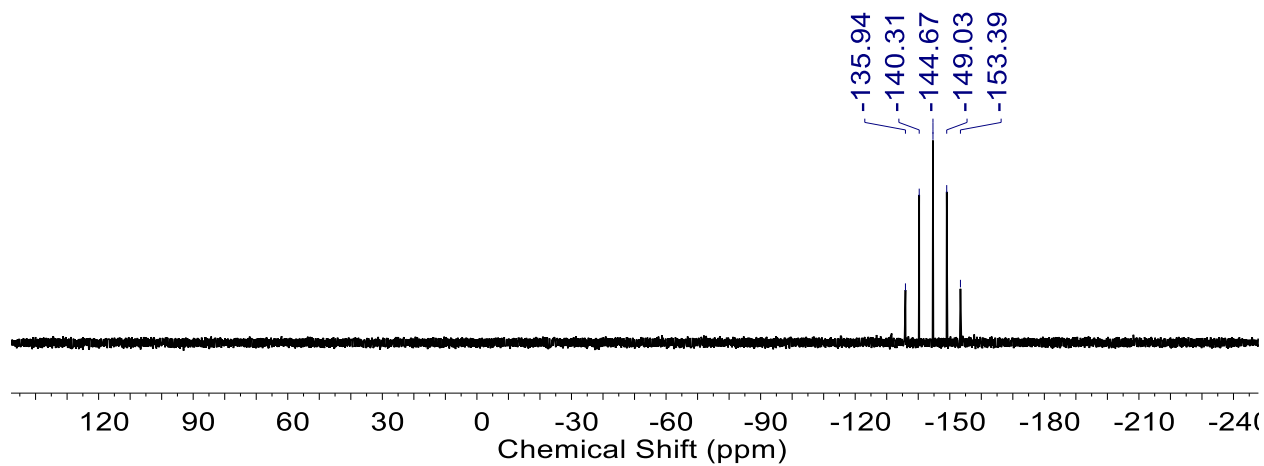
Figure 20. ^{31}P NMR spectrum of **4**.
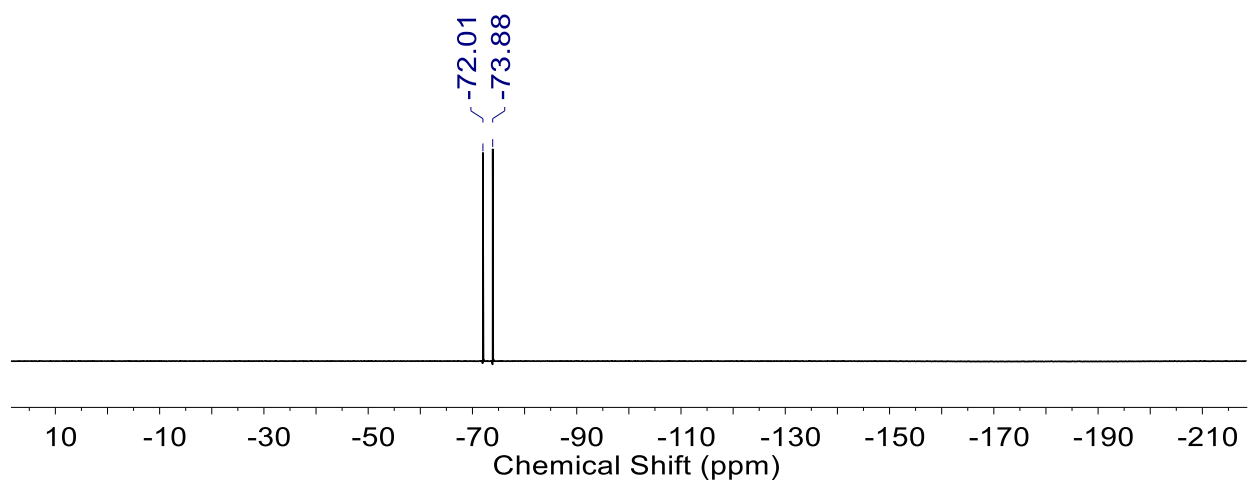
Figure 21. ^{19}F NMR spectrum of **4**.
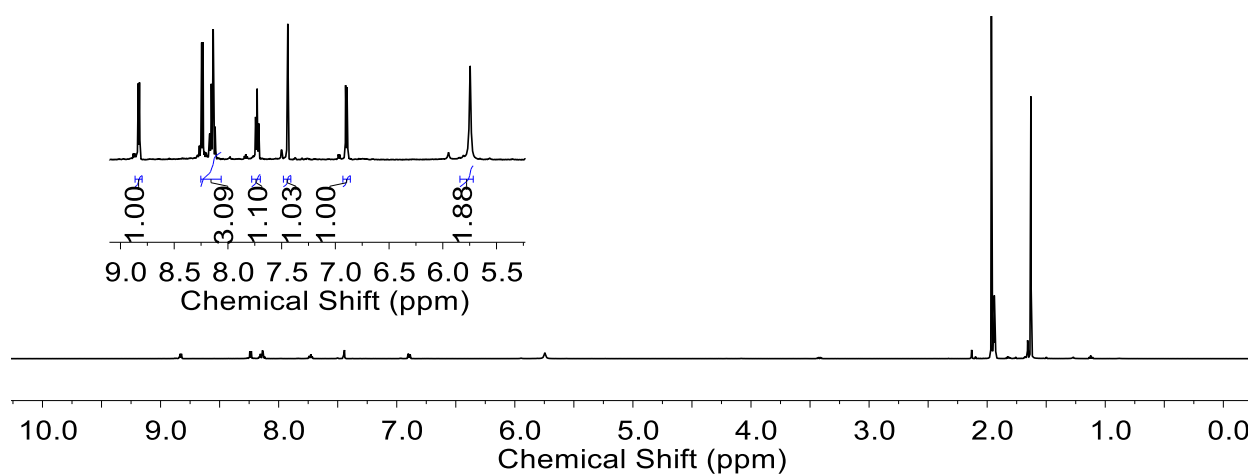
Figure 22. ^{1}H NMR spectrum of **6**.
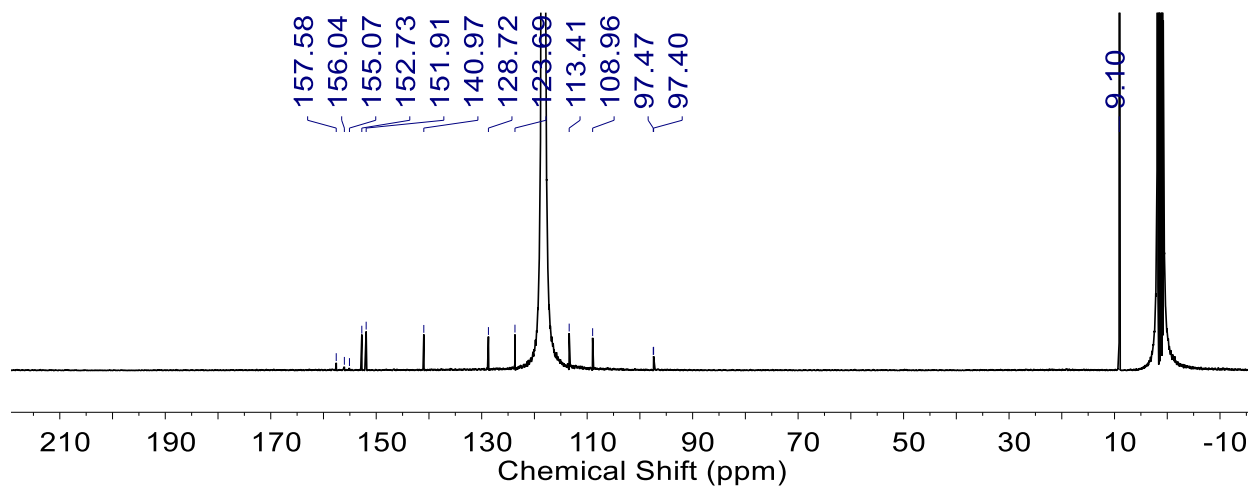
Figure 23. ^{13}C{^{1}H} NMR spectrum of **6**.
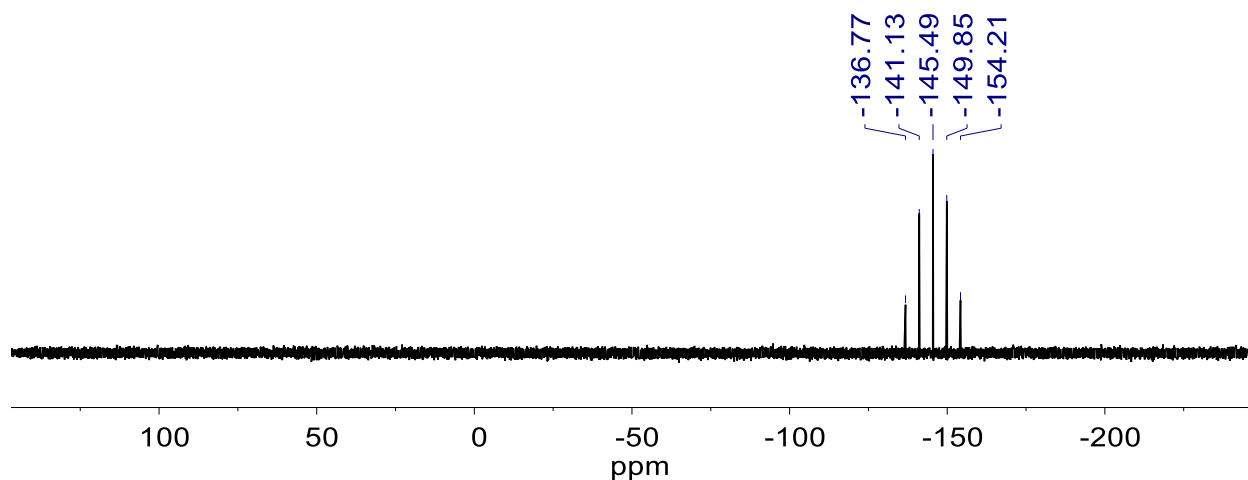
Figure 24. ^{31}P NMR spectrum of **6**.
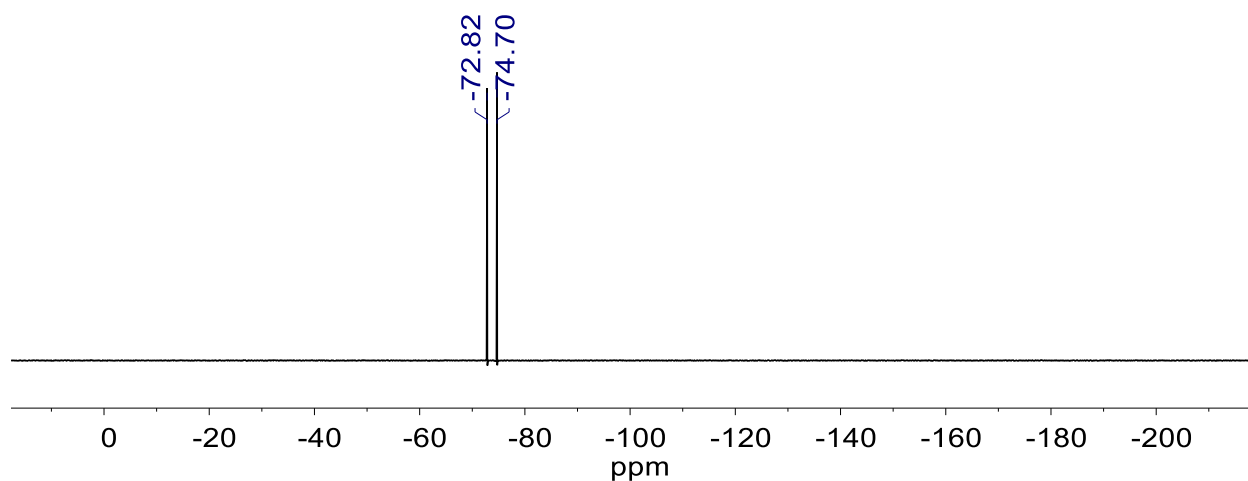
Figure 25. ^{19}F NMR spectrum of **6**.

Single crystals of **4** suitable for X-ray diffraction (XRD) analysis were obtained via slow evaporation of acetonitrile. Data was collected at 200 K with Cu X-rays from a Bruker MicroStar microfocus rotating anode generator running at 45 mA and 60 kV. An Apex 2 detector was positioned at 50.0 mm and equipped with Helios multilayer mirror optics. Frames were collected using counting times of 4-6 seconds for the 1-degree wide scans. Taking into account the likelihood that both r– and s– metallostereocenters will exist due to coordination of the non-symmetric ligand, Olex was set to calculate the relevance of each based on the electron density at the 4 and 4′ positions of the bpy ligand. Based on this calculation, there was approximately a 4:1

mixture of the s:r stereocenters. Other than this unusual feature of the structure solution, it was found that the bond lengths of note were in good agreement with other known structures of analogous [Cp*Rh(bpy)] complexes. The structure is shown in Figure 26 and relevant bond lengths are shown in Table 2.
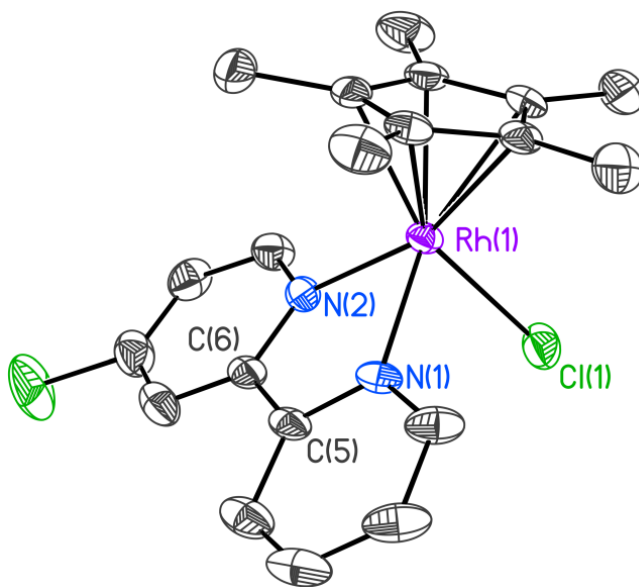
Figure 26. Solid-state XRD crystal structure of complex **4**. Hexafluorophosphate counteranion and hydrogen atoms are omitted for clarity. Displacement ellipsoids shown at 50% probability.

Table 2. Relevant bond lengths for XRD crystal structure of complex **4**.

	Distance (Å)
Rh–N(1)	2.094(4)
Rh–N(2)	2.117(4)
Rh–Cl(1)	2.401(1)
Rh–Cp*centroid	1.771

The next piece of characterization obtained in an effort to understand the properties of these complexes was electronic absorption spectroscopy in the UV-visible region. Complexes **3-6**

display a similar absorption profile, with strong absorption bands in the UV region and weak molar absorptivity bands in the visible region (Figure 27). A number of these absorption bands show up as shoulders on larger peaks and thus the following method was used to distinguish the relevant peak wavelengths. Using Origin Pro software, the first derivative of each absorption spectrum was taken. Local maxima below y = 0 were interpreted to correspond to a mathematically determined center of a shoulder peak. Compiling the estimated absorption band maxima across all complexes reveals some notable trends with respect to the electron donating/withdrawing character of the substituents.
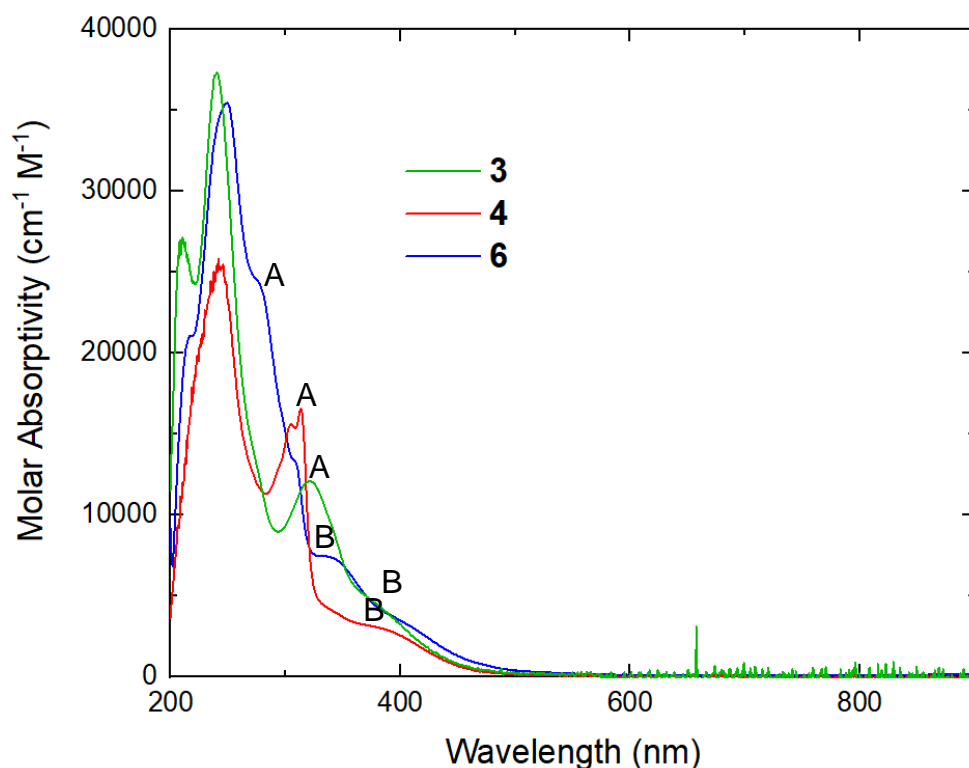
Figure 27. UV-vis absorption spectral overlay for complexes **3**, **4**, and **6**. Peaks denoted as "A" are assigned as ILCT bands based on having high molar absorptivity's and absorbance values in the UV range.[43] Peaks denoted as "B" are assigned as MLCT/LMCT bands based on their relatively low molar absorptivities ($1,000 < \varepsilon < 10,000$ cm^{-1} M^{-1}) and absorbance in the visible range.[43]

There are three main methods by which the electron/withdrawing nature of a substituent can be quantified, all of which fall under the umbrella of the Hammett parameter.[10] The first, original, method utilizes a benzyl ring substituted at the para position (with the substituent of interest) with respect to a carboxylic acid group.[10] Deprotonation of the carboxylic acid group under a certain set of conditions will occur at a certain rate. That rate depends, of course, on the substituent present at the para position. Once the rate for the hydrogen substituted version is determined, the Hammett parameter can be calculated for any substituent by measuring the rate, taking the log of the quotient ($K_{substituent}/K_H$), and normalizing with a factor ρ.[10] The resulting parameter (σ_p) most accurately reflects the character of substituents in similar systems. That is, systems where the substituent is connected to an aromatic moiety and where the transition incurs a negative charge localized at the para position with respect to the substituent. The other two methods utilize different groups besides the carboxylic acid. For the σ_p^- parameter, a para-substituted phenol is used for comparisons.[10] In this case, deprotonation results in a negative charge that can be delocalized over the phenyl ring. For the σ_p^+ parameter (also known as the Brown-Okamoto parameter), that functional group is an isopropyl group in which a chloride replaces the primary hydrogen.[44] In this case, the transformation undergone is the loss of the chloride anion, resulting in a positive charge that can be delocalized over the phenyl ring.[44]

Comparing absorption bands against each of these three parameters is revealing in terms of what transition is occurring. Take the strong intraligand charge transfer (ILCT) bands in the UV region for instance. Plotting these bands against all three parameters and applying a best-fit line reveals which parameter fits the transition most aptly. All three plots are included in Figure 28. For this transition, the σ_p^+ parameter fits markedly better than the other parameters with an R^2 of 0.99. This jives well with the fact that an ILCT involves excitation of an electron from an orbital

associated with the chromophore ligand (the bpy) to an excited state associated with the same ligand. That excitation essentially results in buildup of a quasi-positive charge on the ligand, directly in line with the buildup of positive charge for the Brown-Okamoto parameter. Notably, the trend itself describes a relationship between the electronic nature of the substituent and the ILCT gap where the more electron donating ligands display larger energy gaps.
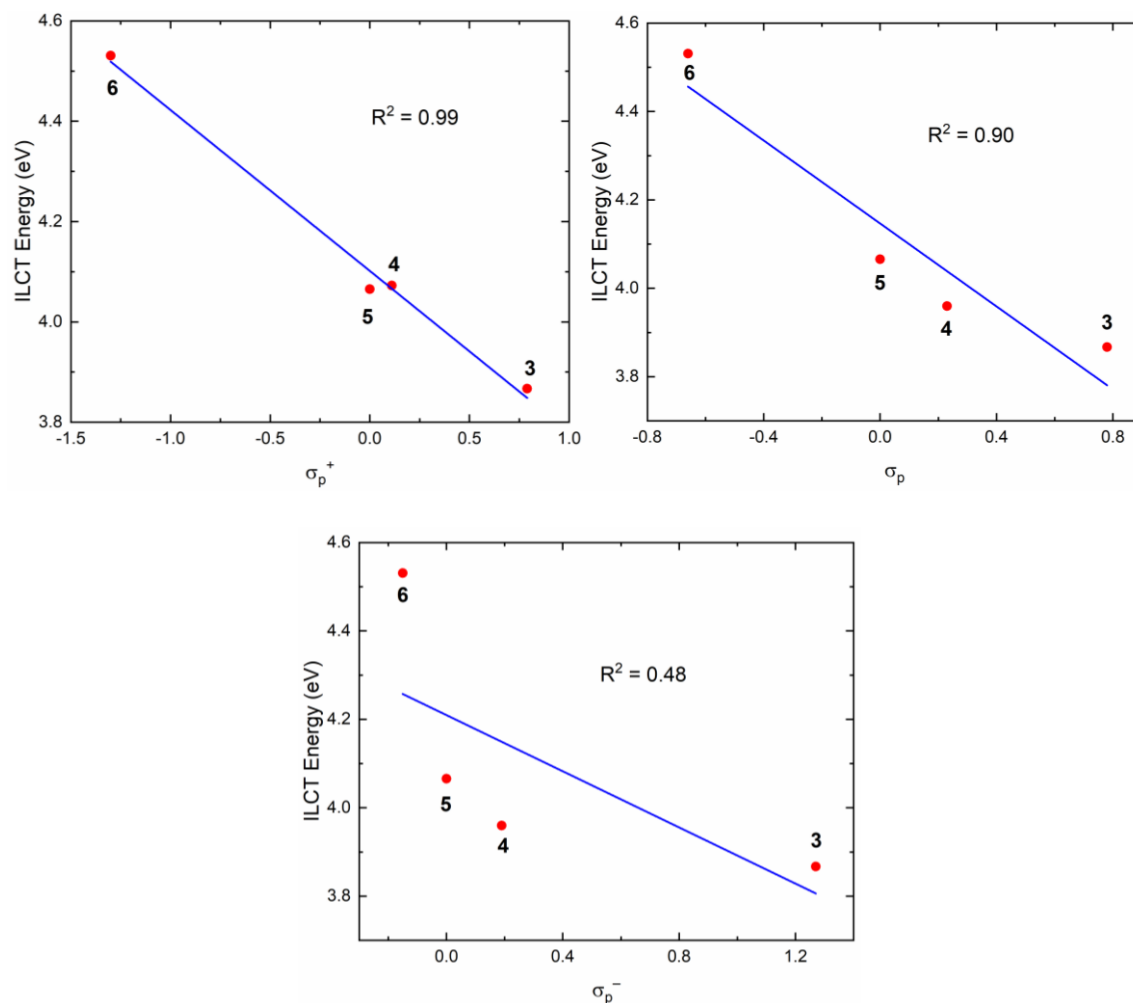

Figure 28. All three Hammett parameter plots versus ILCT energy (in eV). Best-fit lines calculated using OriginPro software with R^2 values included.

Interestingly, applying the same comparison to the metal to ligand charge transfer (MLCT) or ligand to metal charge transfer (LMCT) results in the same parameter fitting best as well (see Figure 29). Accordingly, it is expected that a buildup of positive charge on the chromophore is

45

occurring upon visible light excitation. Specifically, this would be in line with an LMCT, as the excitation of an electron from an orbital associated with bpy to the rhodium metal center would result in a positive charge delocalized throughout the aromatic ligand. Conversely, an MLCT would likely fit the σ_p^- better because excitation of an electron from an orbital associated with the metal to one associated with the bpy would rather result in buildup of delocalized negative charge on the aromatic bpy.
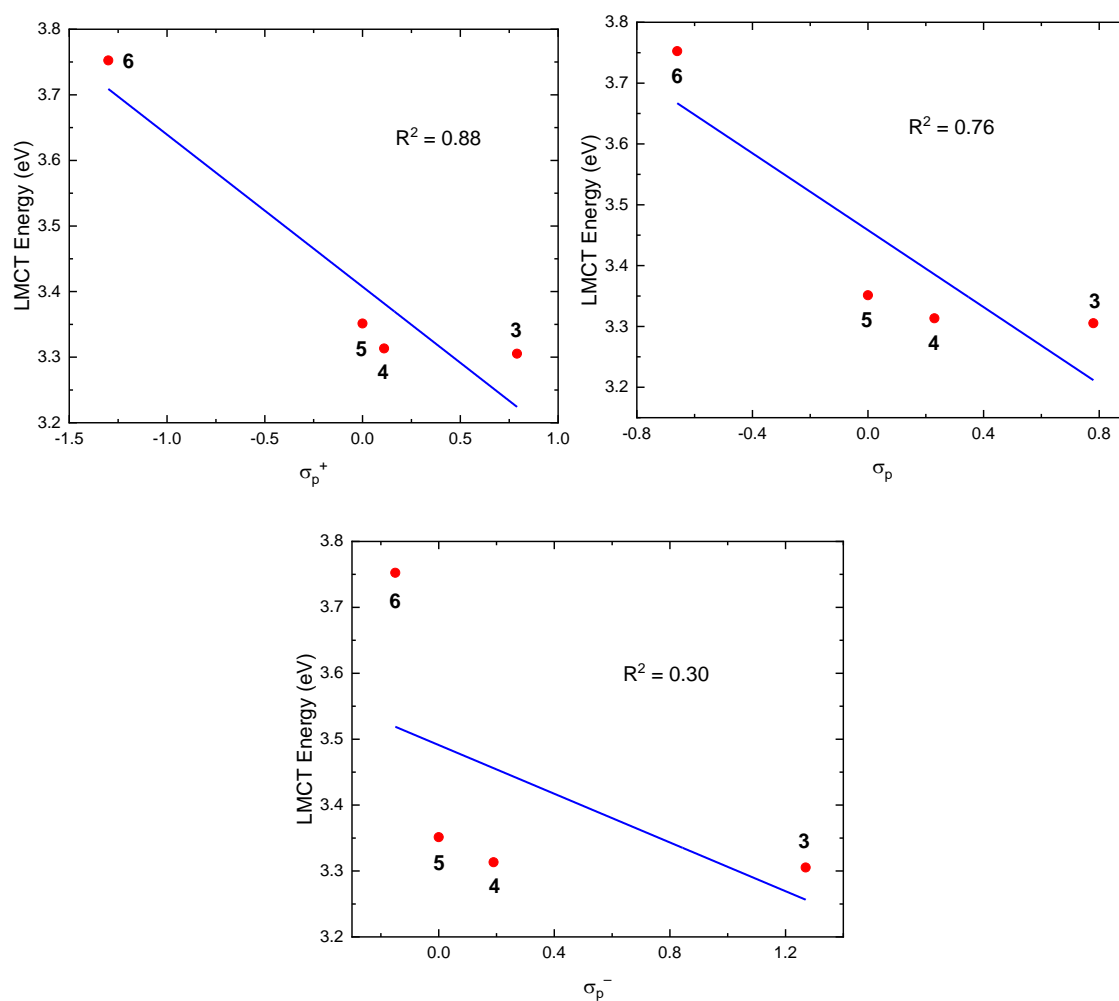
Figure 29. All three Hammett parameter plots versus MLCT (or LMCT) energy (in eV). Best-fit lines calculated using OriginPro software with R^2 values included.

With UV-vis spectroscopy characterization complete and in the interest of beginning to probe the catalytic ability of these complexes, we next turned to electrochemical characterization.

CV data for all three complexes is included in Figure 30. Complexes **4 − 6** all display a single redox event that corresponds to the typical two-electron process with an ECE-type reduction. However, complex **3** exhibits an atypical electrochemical profile in CV (see Figure 30). It shows two cathodic peaks close together at approximately −1 V vs $Fc^{+/0}$, with a single associated anodic peak. Additionally, another quasi-reversible redox event is observed at more negative potentials. The ability to resolve multiple redox events of this complex is consistent with the extreme electron-withdrawing nature of the nitro substituent and its tendency to engender unique phenomena as seen in Ch. 1. Assignment of the first two cathodic peaks is made in the scheme in Figure 31, based on analogous work with complex **1**. Since the $^{4\text{-}NO2}$bpy ligand is sufficiently electron withdrawing, the singly reduced character likely involves character from both the metal center and bpy ligand. That results in an equilibrium between chloride dissociation and retention. Chloride dissociation results in the first sharp reduction and a typical $2e^-$ ECE wave, but retention results in the sloping second reduction at more negative potentials. In order to support this assignment, the complex $[Cp^*Rh(^{4\text{-}NO2}bpy)NCMe][PF_6]$ was synthesized (NMR spectrum in Appendix 2, Figure S1) by adding 1 equiv. of $AgPF_6$ to complex **3**. CV of the new complex (as shown in Appendix 2, Figure S3) results in convergence of the first two cathodic peaks and a shift to lower potentials. This is consistent with the assignment made in Figure 31 in multiple respects. The NCMe ligand, being a poorer σ-donor, results in a rhodium metal center that is less electron rich and therefore more easily reduced. Additionally, as an L-type ligand, NCMe would be more likely to dissociate after the first reduction, resulting in the sharper, typical 2 electron ECE reduction process. This is clearly reflected in Appendix 2, Figure S3.

47
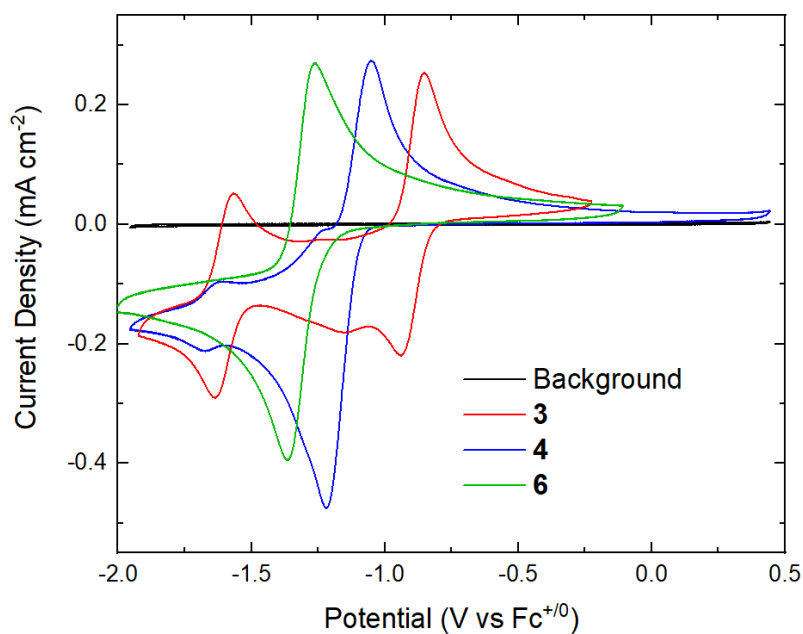
Figure 30. CV overlay of complexes **3**, **4**, and **6**. Concentration of complexes was ~ 1 mM; electrolyte was 0.1 M ($[nBu_4N]^+[PF_6]^-$) in MeCN. WE = highly oriented pyrolytic graphite (HOPG), CE = Pt, and RE = Ag$^{+/0}$.

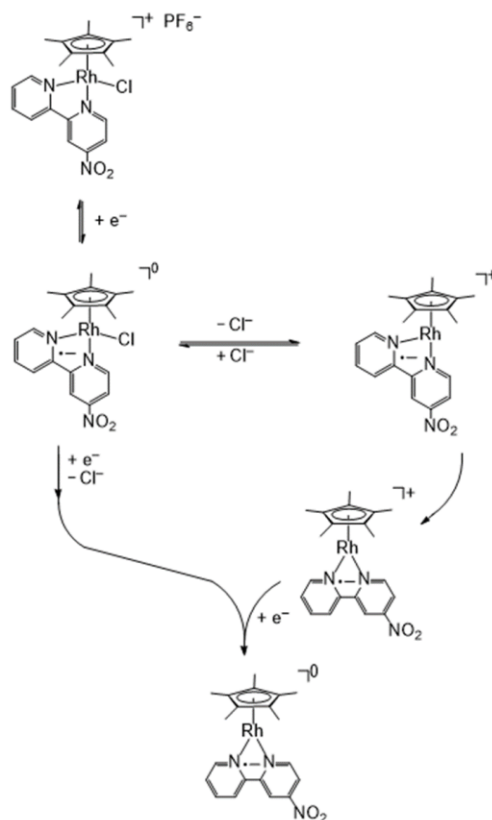**Figure 31**. Electrochemical reduction scheme of complex **3** based on analogous work with complex **1**.

48

The potential of the $Rh^{III/I}$ couple was also plotted against all three Hammett parameters as shown in Figures 32. The σ_p^- parameter trends best with these reduction potentials. This can be readily interpreted since electrochemical reduction leads to buildup of negative charge that is delocalized over the bpy ligand. The result is that more electron-donating substituents result in more negative reduction potentials, while electron-withdrawing substituents incur the opposite. This trend mirrors what has been seen before in more symmetric complexes: specifically, there is significant electronic communication between the bpy ligand and rhodium metal center. The prior findings with more symmetric disubstituted ligands on the same framework were previously uncovered by my coworker Wade Henke.[8]
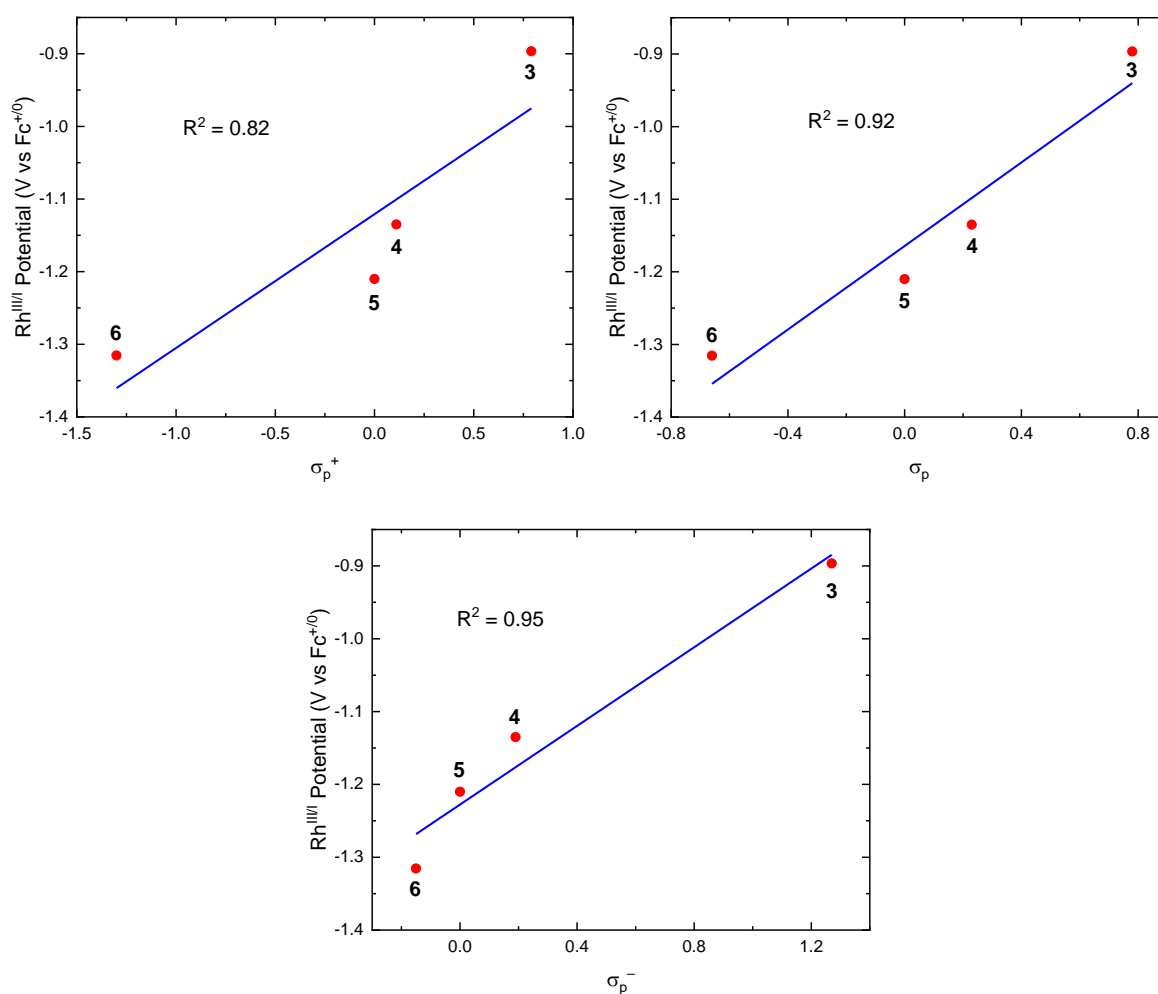
Figure 32. Hammett parameter plots for $Rh^{III/I}$ couple potentials of complexes **3**, **4**, and **6**.

Conclusions

A divergent synthetic method was strategically assembled by piecing together literature syntheses as a straightforward route to preparation of four bipyridyl ligands of differing electron withdrawing/donating character, three of which are non-symmetric ($^{4\text{-}R}$bpy where R = NO$_2$, Cl, H, and NH$_2$). These ligands were coordinated to the [Cp*Rh] platform yielding three new compounds. Clean isolation of the complexes was confirmed by NMR analysis as well as single-crystal XRD in the case of the chloro-derivative. UV-vis spectroscopy reveals that the electron withdrawing/donating character of the substituent affects the charge transfer energies of the complex. More specifically, both the ILCT and MLCT band energies vary uniformly with the Brown-Okamoto parameter (σ_p^+). As the electron donating character of the substituent increases, so does the energy of both charge transfers. Electrochemical analysis via CV reveals typical Rh$^{III/I}$ couples for complexes **4**, **5**, and **6**. Complex **3**, however, displays a unique electrochemical profile in which there is an equilibrium between Cl$^-$ dissociation and retention as a result of shared singly reduced character between the Rh center and electron withdrawing ligand (this situation arises uniquely as a result of the nitro substituent). The potentials of the Rh$^{III/I}$ couples also trend well with the Hammett parameter. In this case, there is a linear relationship with the σ_p^- parameter, a reflection of generating a delocalized negative charge upon reduction. In this trend, more electron-donating substituents incur more negative redox potentials. To the best of our knowledge, this is the first instance in which it has been demonstrated that properties of [Cp*Rh] complexes can be definitively affected by non-symmetric monosubstitution of a bidentate bipyridyl ligand. Taken further, these studies suggest exciting opportunities in tuning catalysis with these complexes. Future work will focus on determining the catalytic ability of each complex and addressing these opportunities in detail.

Appendix 1

NMR Spectroscopy
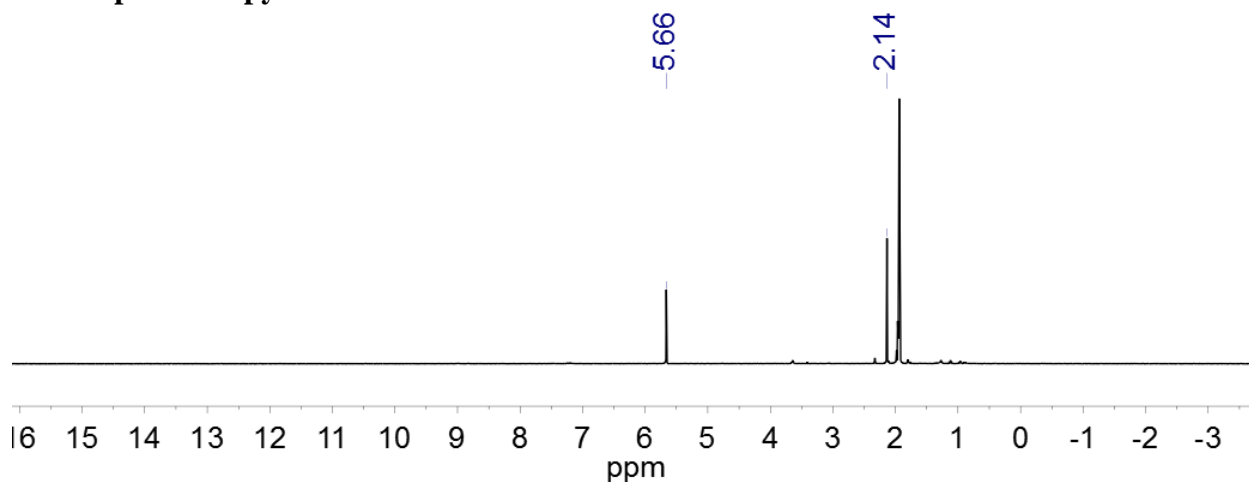
Figure S1. ^{1}H NMR spectrum (400 MHz, CD$_3$CN) of aliquot from reduction of **3**. Minor trace impurities: water, THF, Et$_2$O, toluene, acetonitrile, and pump oil. Cobaltocenium visible at δ = 5.66 ppm.
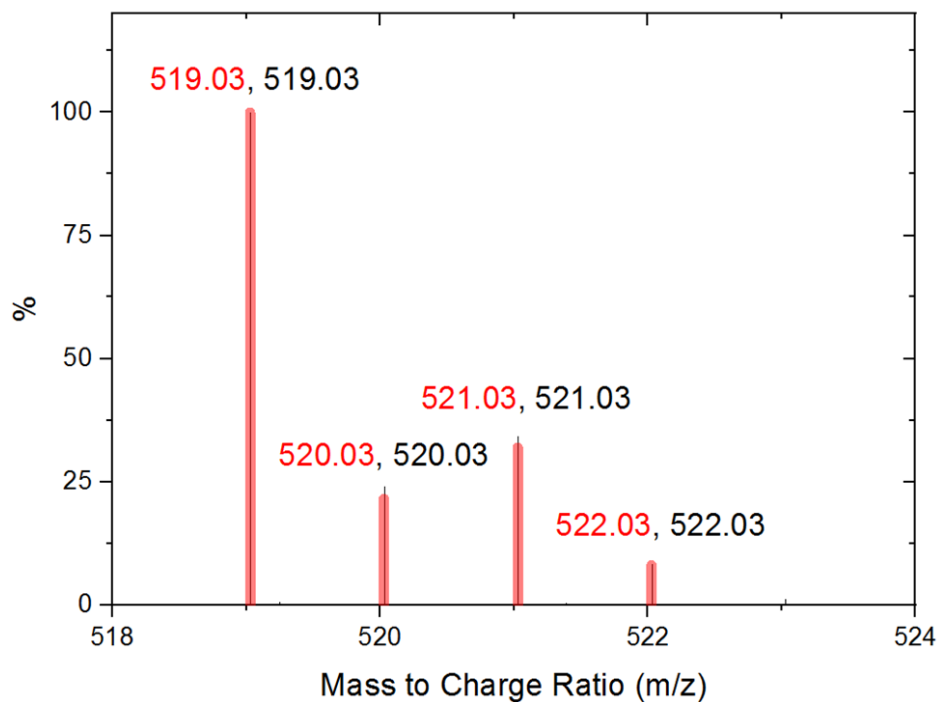
Mass Spectrometry

Figure S2. Mass spectrometry of **3**. Comparison overlay of predicted (red) and experimental (black) mass spectra in MeCN.
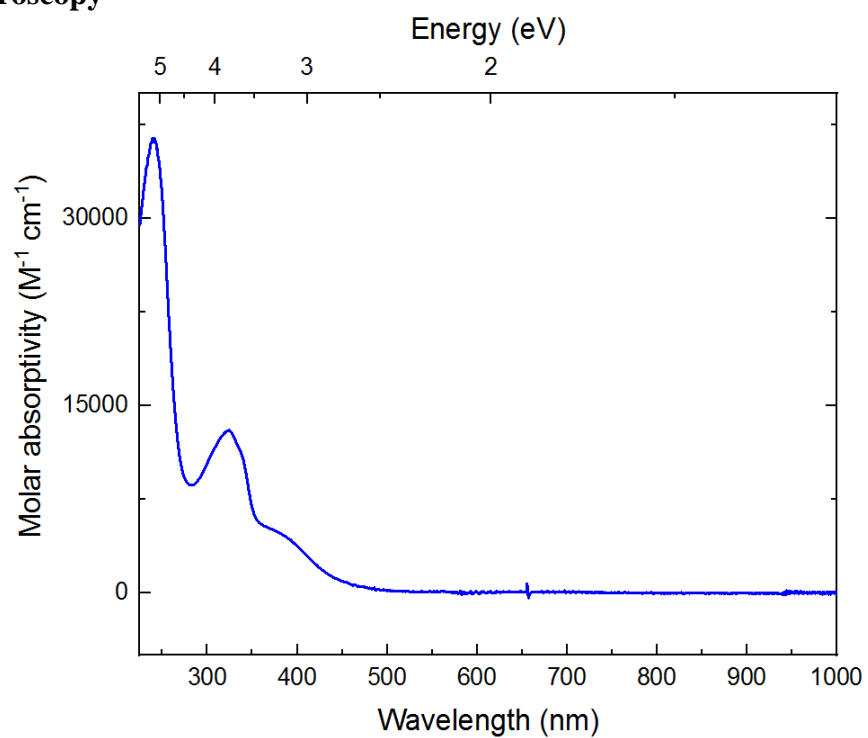
Optical Spectroscopy

Figure S3. Electronic absorption spectrum of **3** in THF: 263 (36400), 323 (13000), 365 (5300 M^{-1} cm^{-1}).
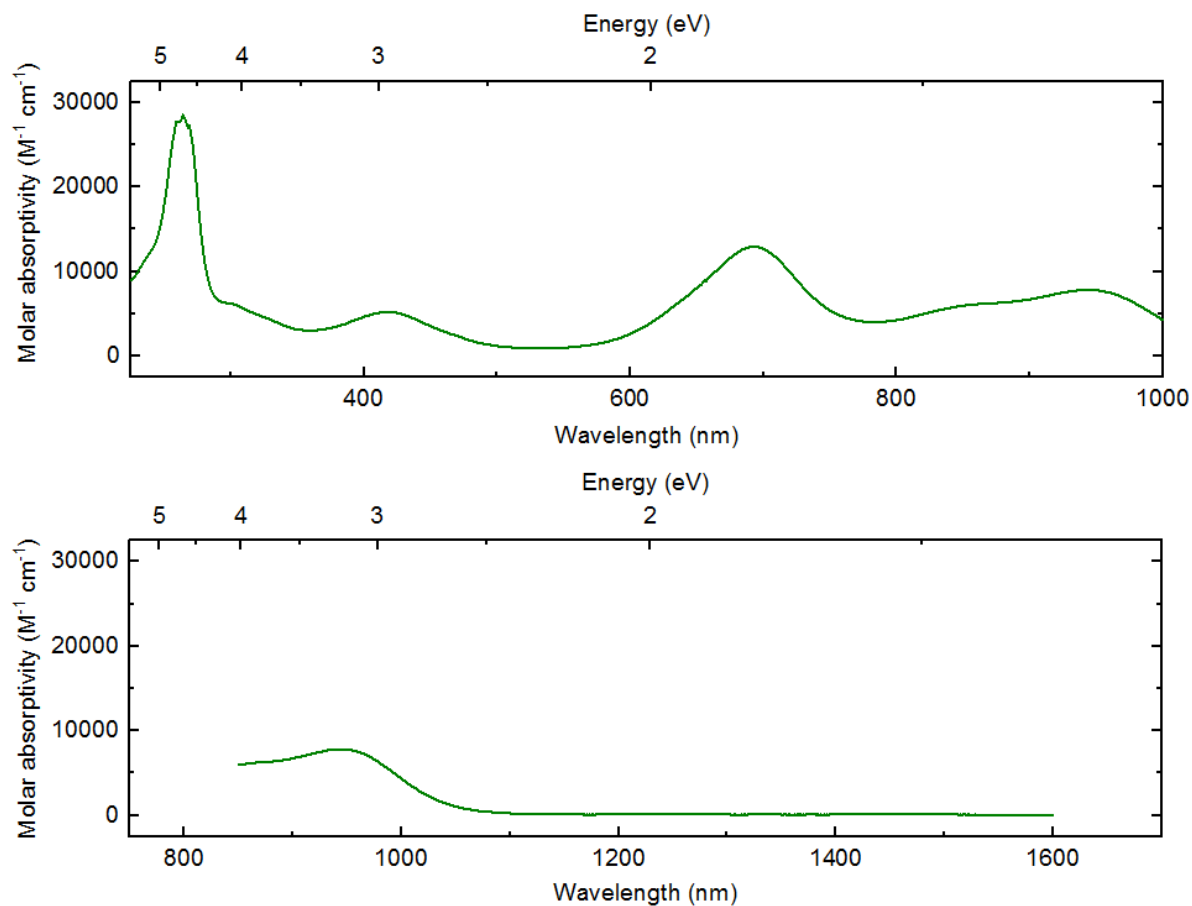
Figure S4. Electronic absorption of isolated **4** in the UV-visible region (top panel) and near infrared (NIR) region (bottom panel): 265 (28500), 300 (6100), 420 (5200), 694 (13000), 860 (6100), and 945 (7800). Spectra were taken with the same 0.1 mM solution in a Schlenk cuvette under an atmosphere of N_2. The near IR spectrum was collected with a Shimadzu 3600 UV-vis-NIR Spectrophotometer.

Electrochemistry
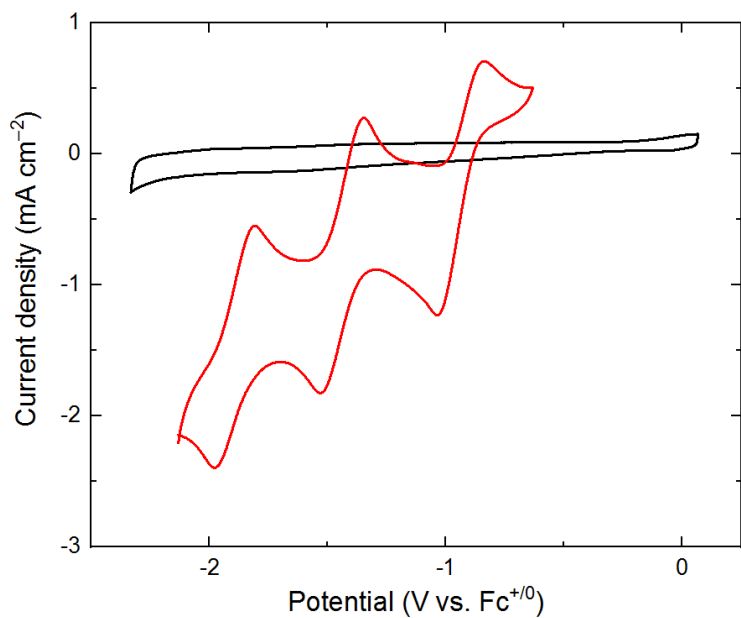
Figure S5. Cyclic voltammetry of **3** (THF, 0.1 M ([nBu$_4$N]$^+$[PF$_6$]$^-$), 100 mV/s; red line) overlaid on background response (black line). Second complete cycles shown for both voltammograms.
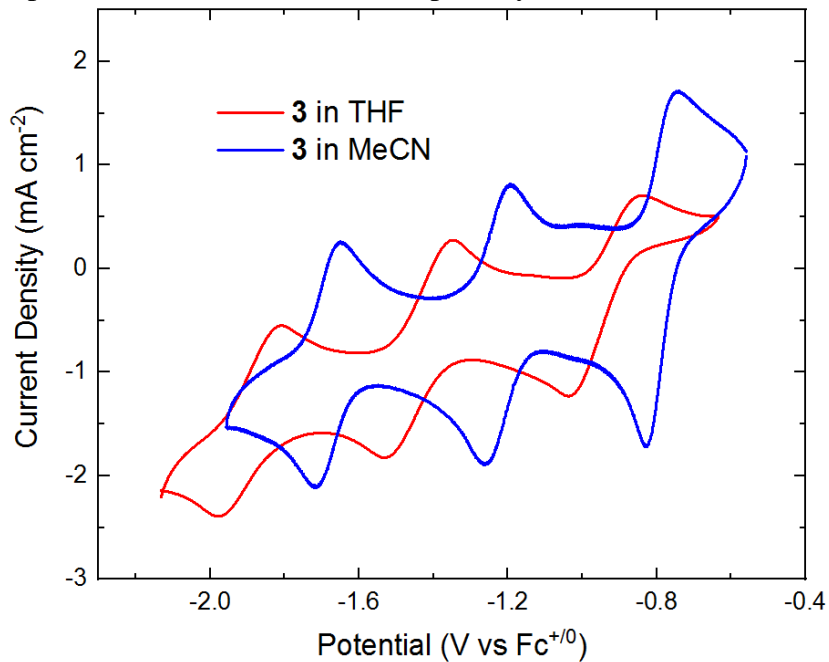
Figure S6. Cyclic voltammetry of **3** in THF and MeCN with 0.1 M ([nBu$_4$N]$^+$[PF$_6$]$^-$) as supporting electrolyte at a 100 mV/s scan rate.

	THF		Acetonitrile	
Couple	$E_{1/2}$	ΔE_p	$E_{1/2}$	ΔE_p
A	−0.94	0.20	−0.79	0.09
B	−1.44	0.18	−1.23	0.07
C	−1.89	0.17	−1.68	0.07
D	−2.19	0.35	−2.07	0.12

Table S1. Tabulated cyclic voltammetric data (midpoint potentials, $E_{1/2}$, and peak–to–peak separations, ΔE_p) for **3** in THF and MeCN with 0.1 M [^{n}Bu$_4$N][PF$_6$] as supporting electrolyte at a 100 mV/s scan rate.

Solvent	$E_{pc}^{(A)}$	$E_{pa}^{(A)}$	$E_{pc}^{(B)}$	$E_{pa}^{(B)}$	$E_{pc}^{(C)}$	$E_{pa}^{(C)}$	$E_{pc}^{(D)}$	$E_{pa}^{(D)}$
THF	−1.04	−0.84	−1.53	−1.35	−1.98	−1.81	−2.36	~ −2.0
Acetonitrile	−0.83	−0.74	−1.26	−1.19	−1.72	−1.65	−2.12	~ −2.0

Table S2. Cyclic voltammetric peak positions (cathodic, $E_{p,c}$, and anodic, $E_{p,a}$) for **3** in THF and MeCN with 0.1 M ([nBu$_4$N]$^+$[PF$_6$]$^-$) as supporting electrolyte at a 100 mV/s scan rate.
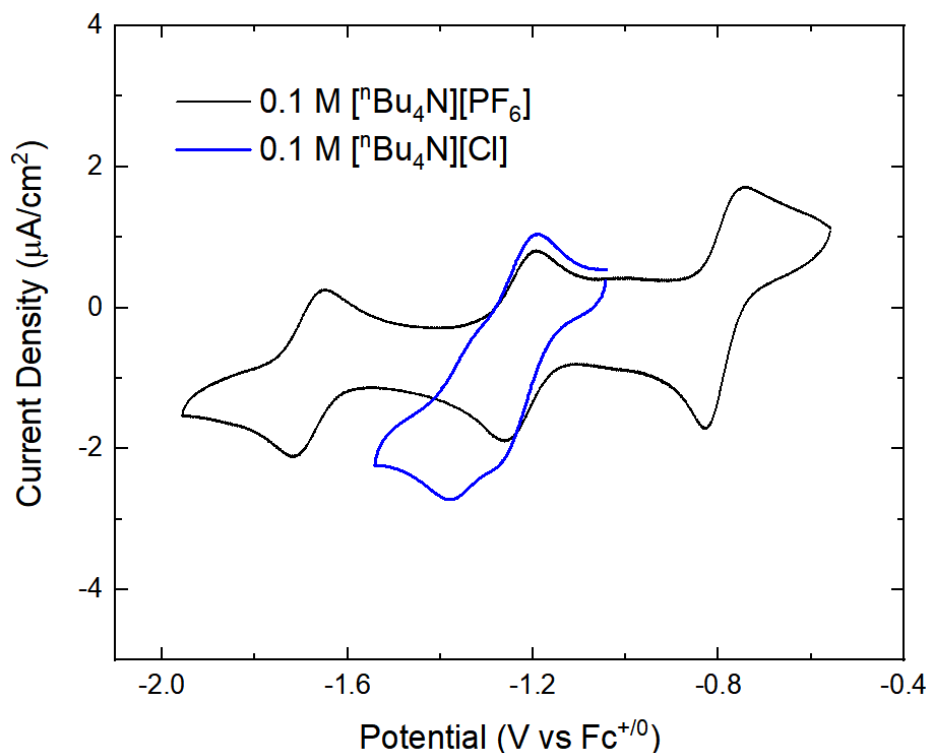
Figure S7. Cyclic voltammetry of **3** in acetonitrile with 0.1 M ([nBu$_4$N]$^+$[PF$_6$]$^-$) and ([^{n}Bu$_4$N]$^+$[Cl]$^-$) respectively. Reduction events occur at −1.28 and −1.38 V vs Fc$^{+/0}$. Single oxidation occurs at −1.19 V.
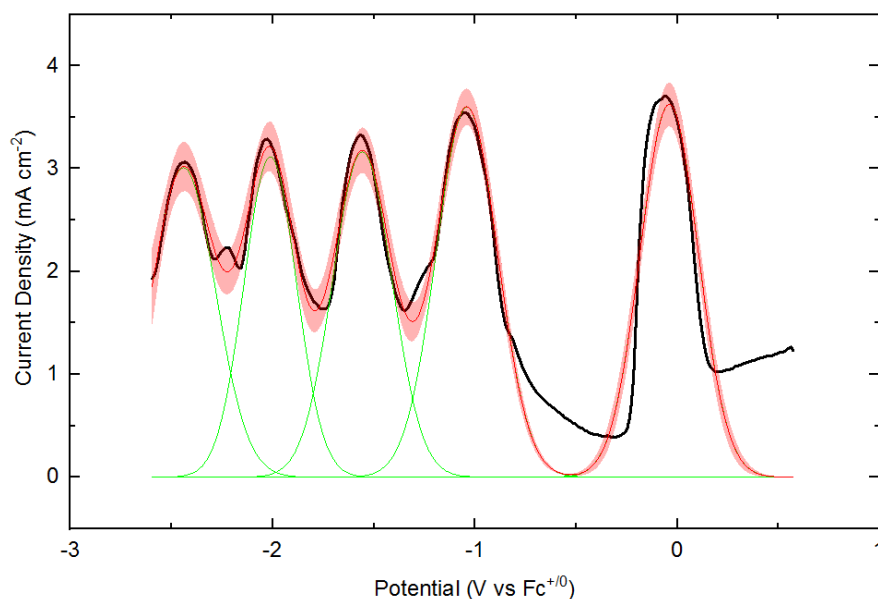
Figure S8. Differential pulse voltammetry (THF, 0.1 M ^{asdf}, 10 mV step size) of **3** with one equivalent of ferrocene (black line). Gaussian fit of the five peaks shown in green and red lines. Associated uncertainty at 95% included in light red.

Couple	Peak area ratio w.r.t. Fc$^{+/0}$ peak	Fit peak area
D	0.9 ± 0.1	1.02 ± 0.10
C	0.8 ± 0.1	1.00 ± 0.10
B	0.9 ± 0.1	1.16 ± 0.06
A	1.1 ± 0.1	1.37 ± 0.03
Fc$^{+/0}$	1.0 ± 0.1	1.30 ± 0.04

Table S3. Tabulated differential pulse voltammetry data for **3** in THF electrolyte at scan rate of 100 mV/s.
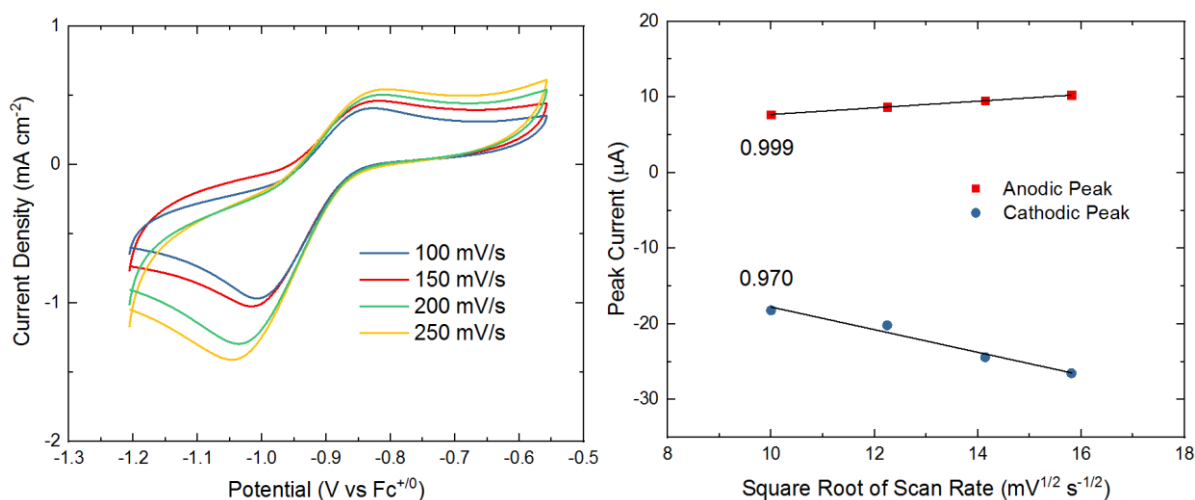
Figure S9. Scan rate dependence of couple A indicating free diffusion.

56
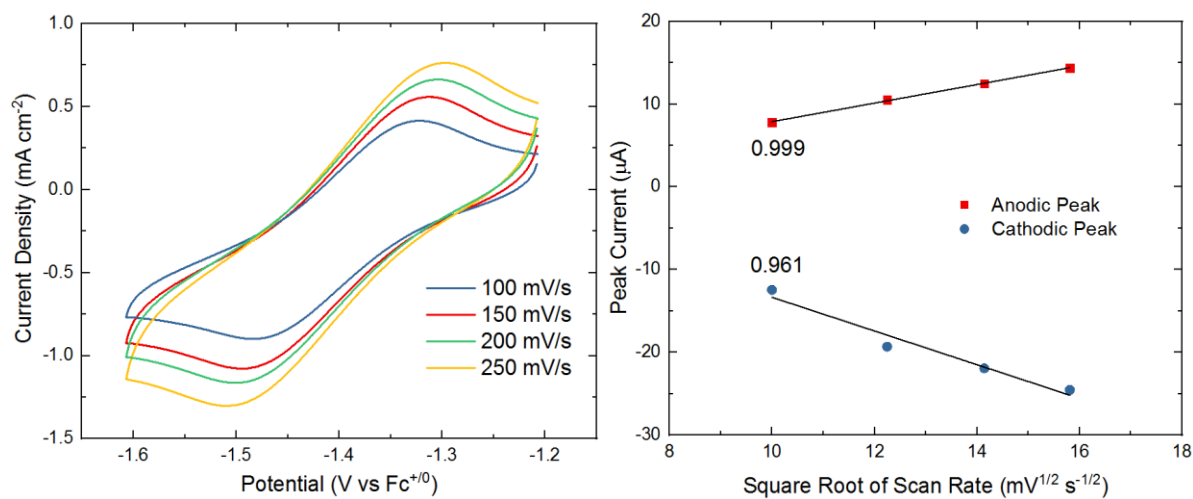
Figure S10. Scan rate dependence of couple B indicating free diffusion.
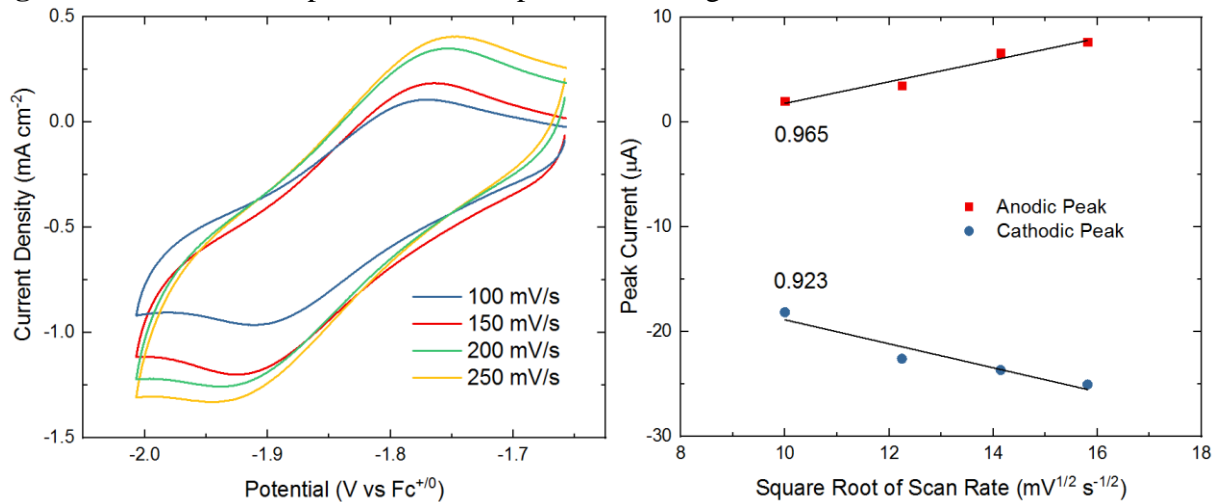
Figure S11. Scan rate dependence of couple C indicating semi–free diffusion. Small discrepencies indicate marginal instability of triply reduced **3**.
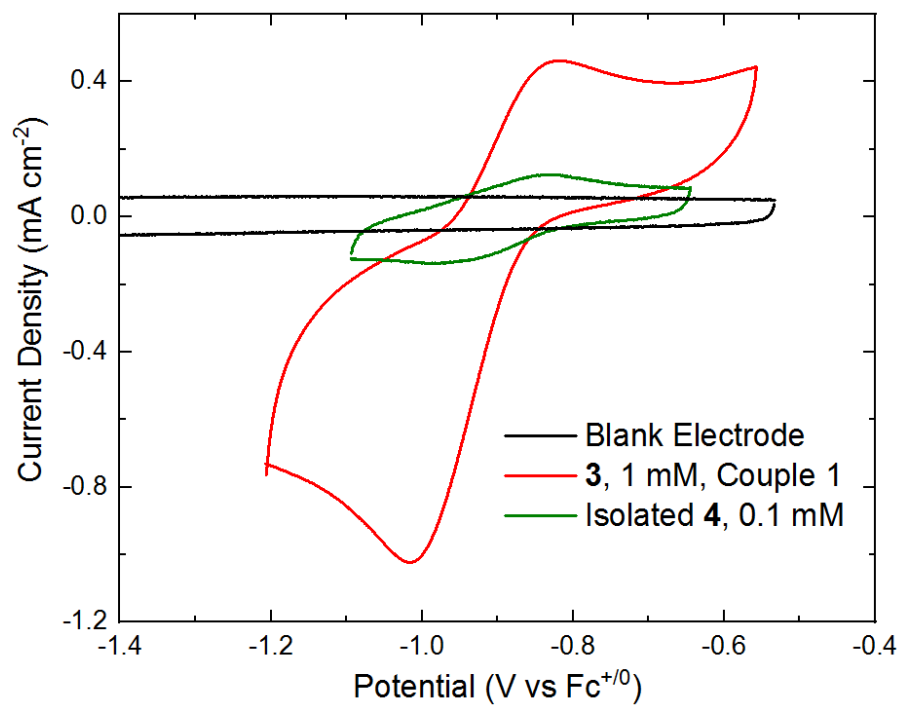
Figure S12. Cyclic voltammetry (THF, 0.1 M [^{n}Bu$_4$N][PF$_6$]) of reduction product **4** in comparison with the starting **3**.

	$E_{p,c}^{(A)}$	$E_{p,a}^{(A)}$	$E_{1/2}$	ΔE_p
3	−1.04	−0.84	−0.94	0.20
Isolated **4**	−1.02	−0.84	−0.93	0.18

Table S4. Tabulated cyclic voltammetry data for **3** and **4** in THF electrolyte at scan rate of 100 mV/s.
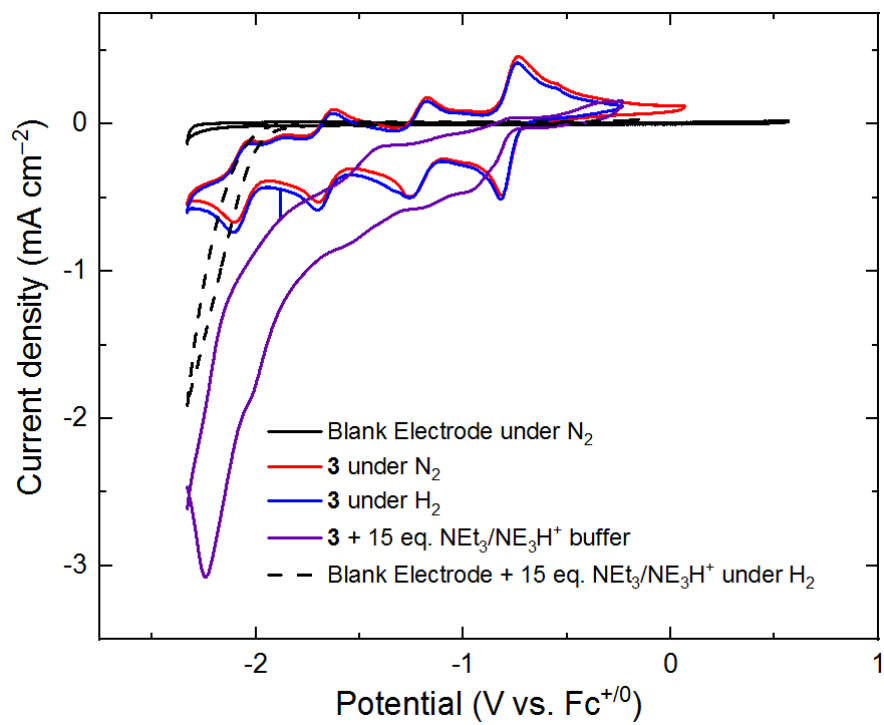
Figure S13. Cyclic voltammetry studies in MeCN with addition of triethylamine (NEt_3) and triethylammonium bromide ($[Et_3NH][Br]$) buffer under an atmosphere of H_2.

Bulk Electrolysis
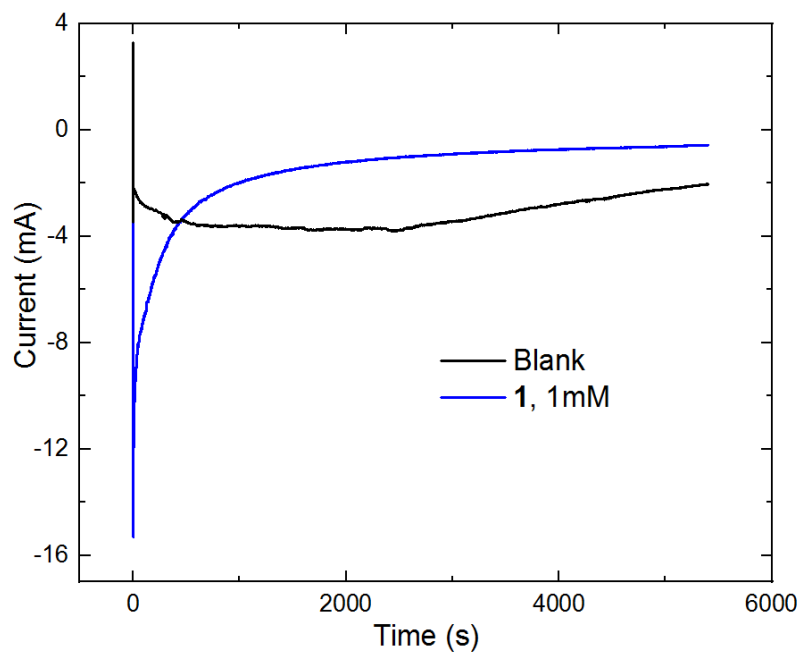
Figure S14. Chronoamperometry experiments conducted during bulk electrolyses. Polarization at -1.75 V vs $Fc^{+/0}$. Ten equivalents of ferrocene included as sacrificial reductant, and 10 equivalents of $[Et_3NH][Br]$ added as the acid. Supporting electrolyte was 0.1 M $[NBu_4][PF_6]$ in each case.
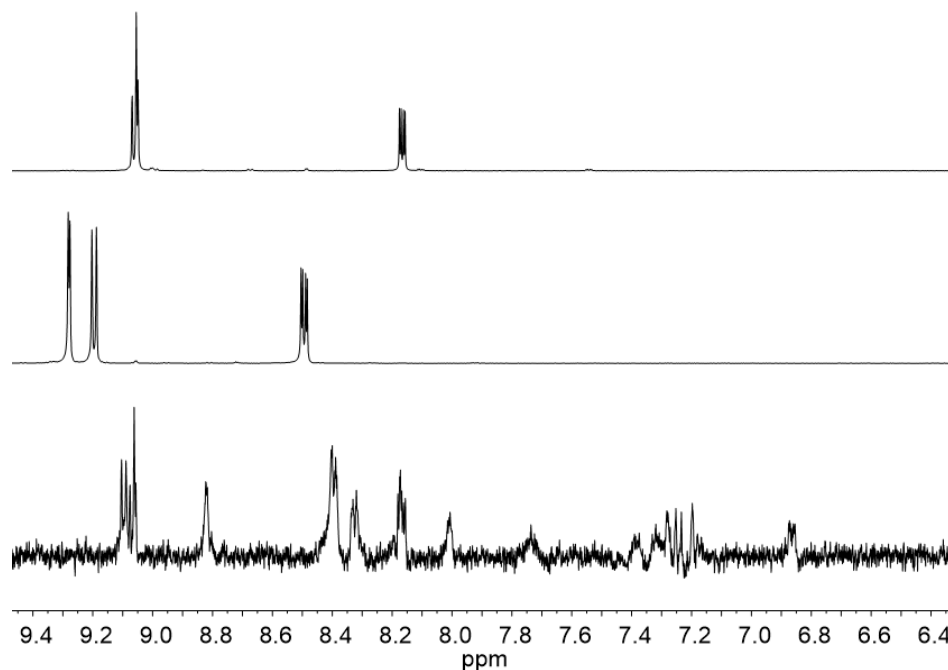
Figure S15a. ^{1}H NMR spectra (400 MHz, CD$_3$CN) of free ligand (top panel), pure **3** (middle panel), and pumped down bulk electrolysis solution (bottom panel). Alophatic region cut out for clarity due to large [^{n}Bu$_4$N][PF$_6$] peaks.
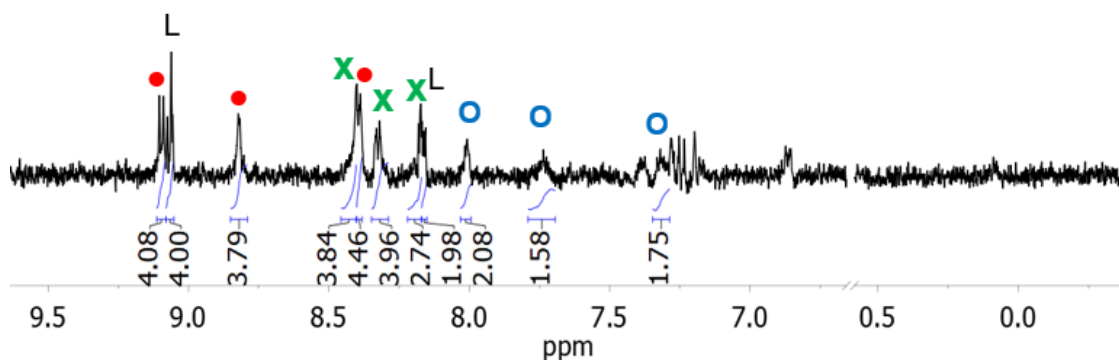
Figure S15b. ^{1}H NMR spectra (400 MHz, CD$_3$CN) of pumped down bulk electrolysis solution showing three sets of $^{4,4'\text{-}NO2}$bpy peaks(●, X, O) integrating approximately 1:1:1 in addition to two signals corresponding to free ligand (**L**, 2:1 due to overlap).
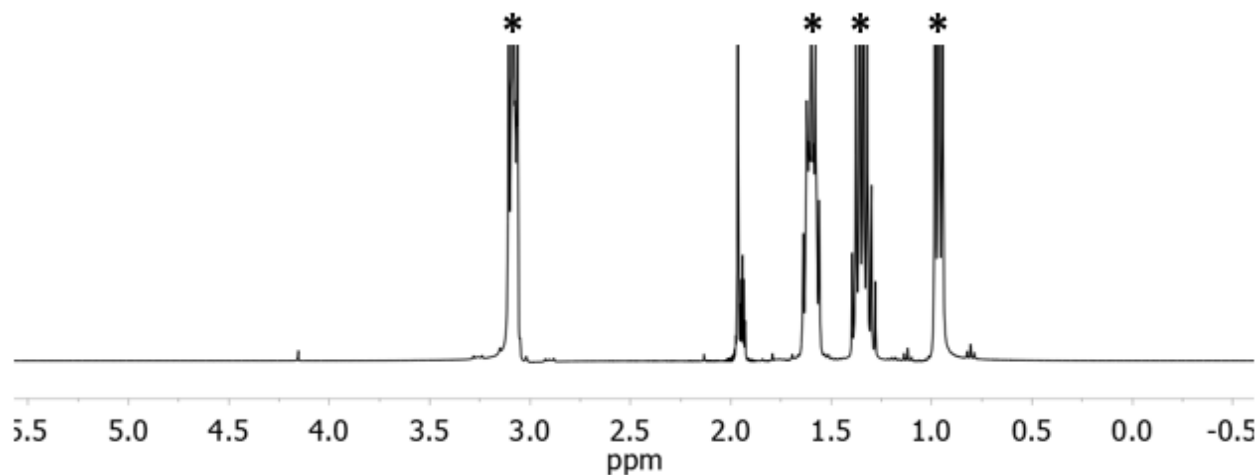
Figure S15c. ^{1}H NMR (CD$_3$CN, 400 MHz) showing the aliphatic region of sample obtained from bulk electrolysis solution following removal of solvent *in vacuo*. Four sharp peaks visible (✷) corresponding to tetrabutylammonium and triethylammonium.
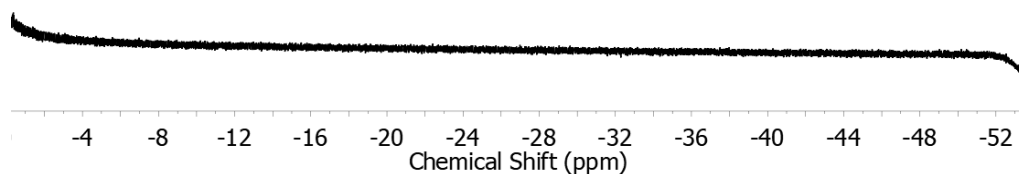
Figure S16. ^{1}H NMR spectrum (400 MHz, CD$_3$CN) of aliquot from bulk electrolysis cell, pumped down. No hydride signals visible.
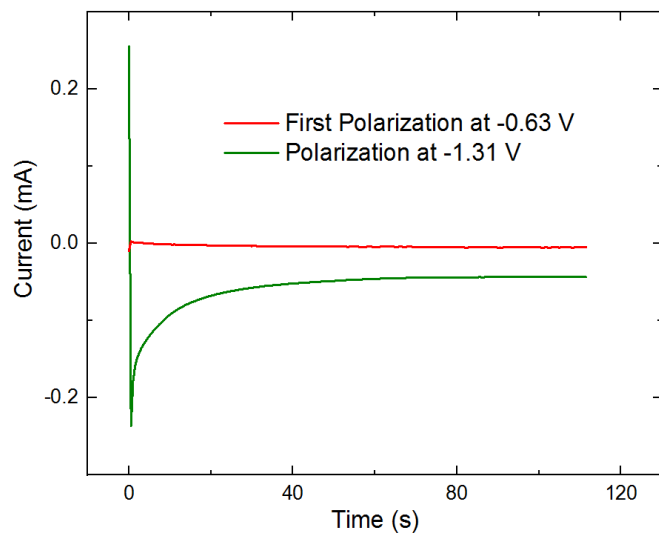
Spectroelectrochemistry (SEC)

Figure S17. Chronoamperometry experiments for polarization positive and negative of the first redox couple.
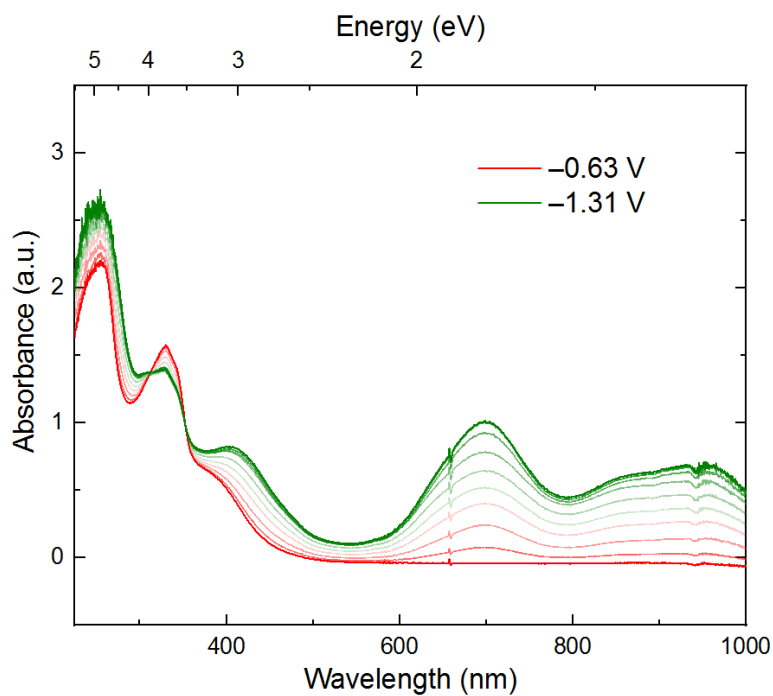
Figure S18. Electronic absorption spectra of **3** selected at regular intervals during polarization (initial: -0.63 V, final: -1.31 V vs. to $Fc^{+/0}$). Isosbestic points are located at 312 and 352 nm.
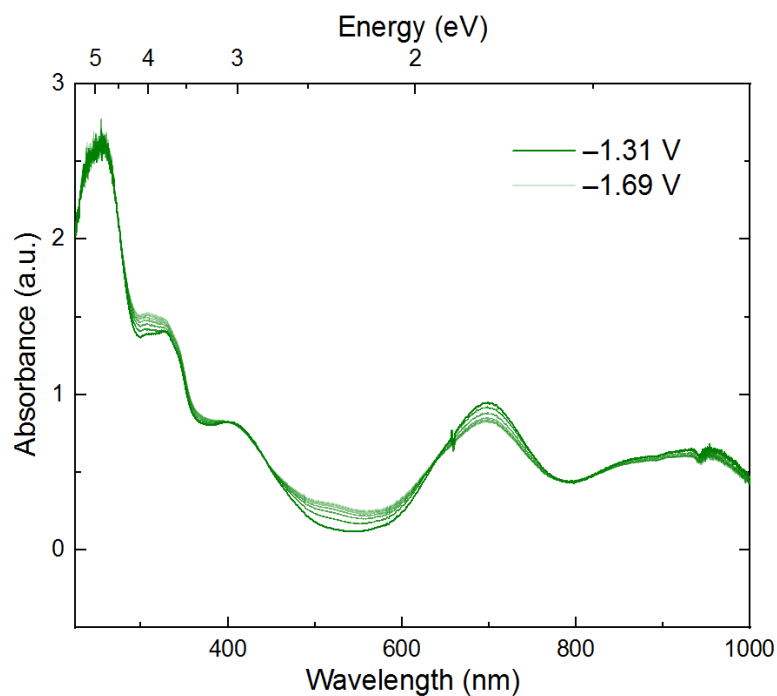
Figure S19. Electronic absorption spectra selected at regular intervals during polarization (initial: −1.31 V, final: −1.69 V vs. Fc$^{+/0}$). Isosbestic points are located at 437, 638, and 800 nm.
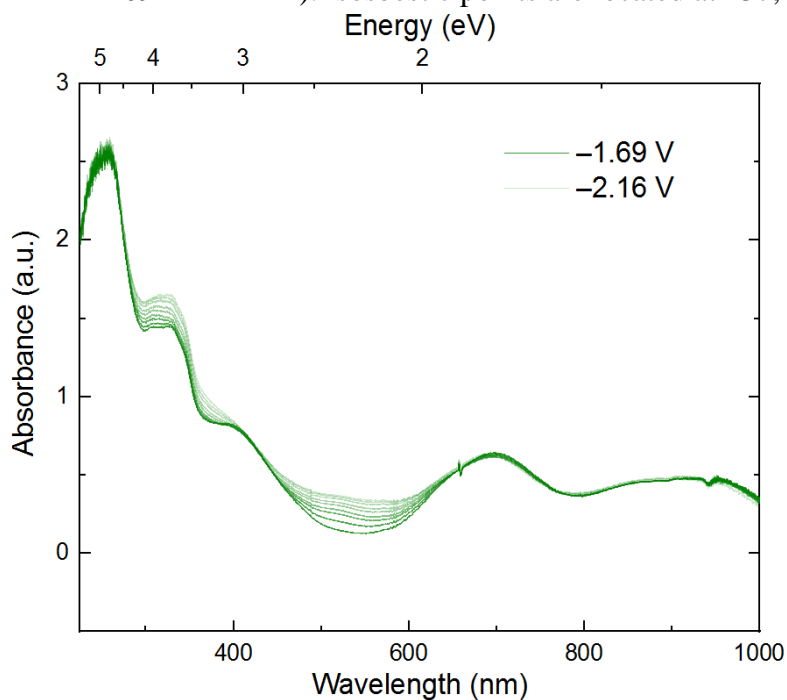

Figure S20. Electronic absorption spectra selected at regular intervals during polarization (initial: −1.69 V, final: −2.16 V vs. Fc$^{+/0}$). Isosbestic point located at 420 nm.
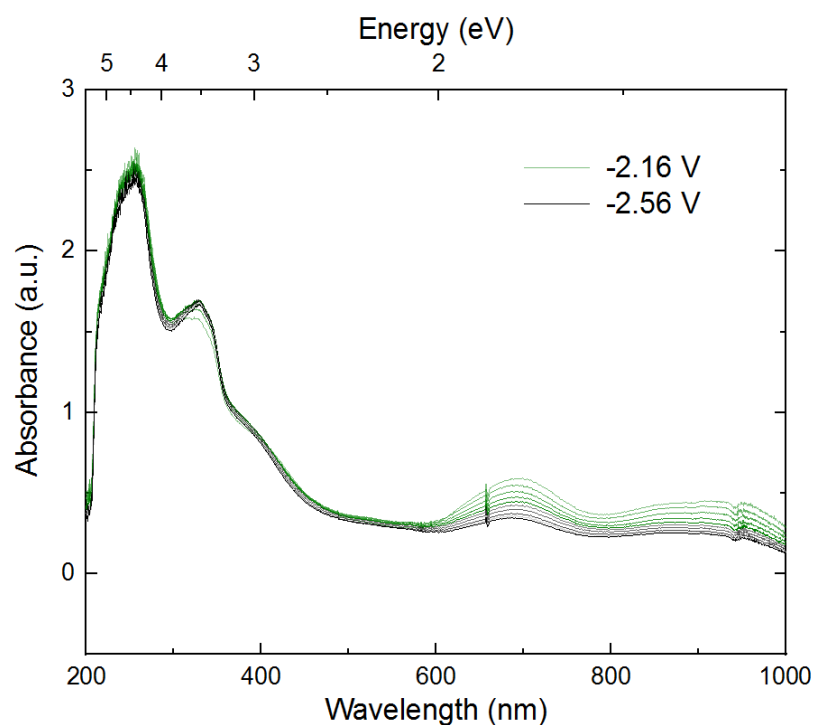
Figure S21. Electronic absorption spectra selected at regular intervals during polarization (initial: −2.16 V, final: −2.56 V vs. Fc$^{+/0}$).
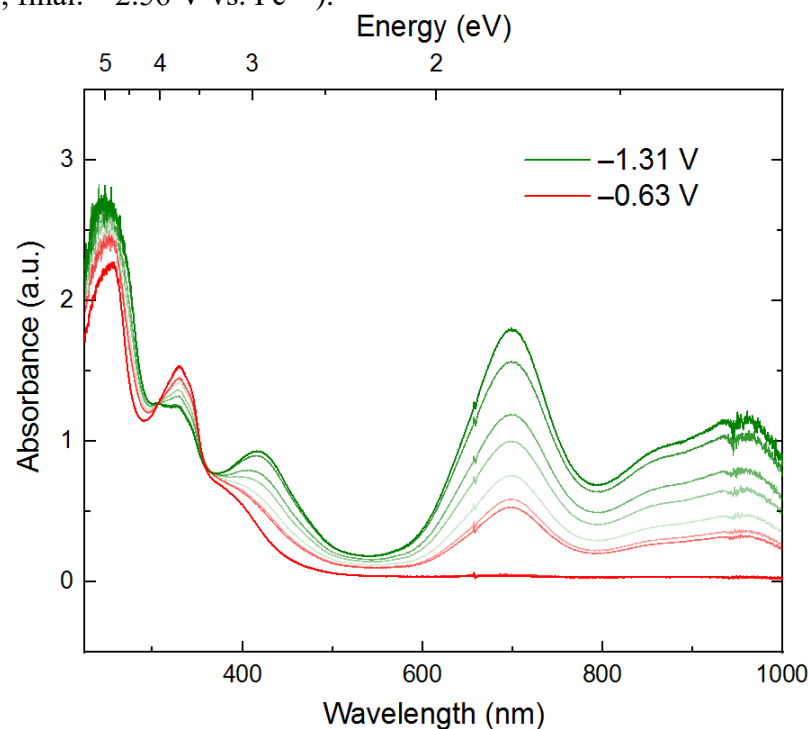

Figure S22. Electronic absorption spectra selected at regular intervals during polarization (initial: −1.31 V, final: −0.63 V vs. Fc$^{+/0}$). Distance from working to counter electrode altered from 10 to 1 mm. Isosbestic points remain at 312 and 352 nm.
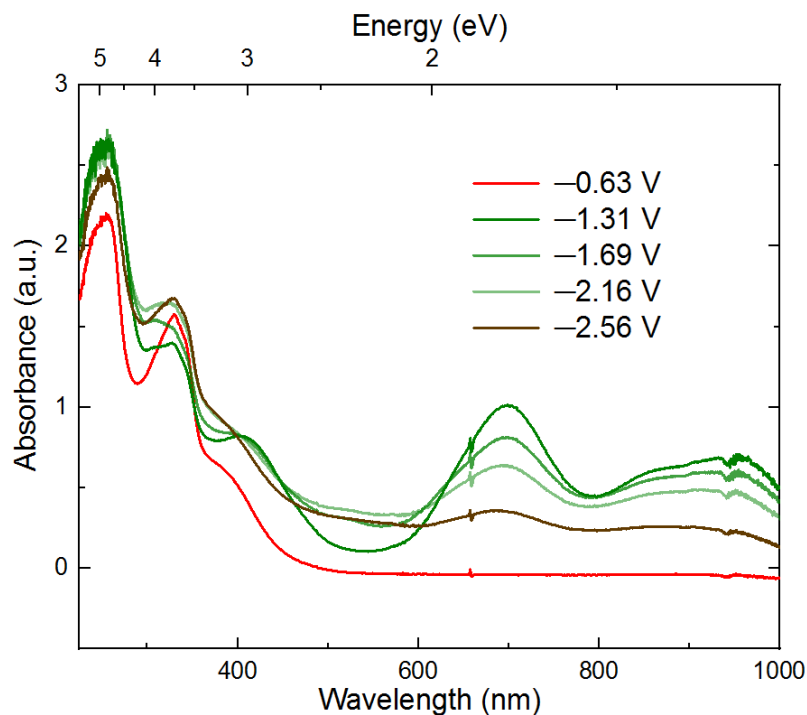
Figure S23. Electronic absorption spectra of the five accessible oxidation states of **3**.
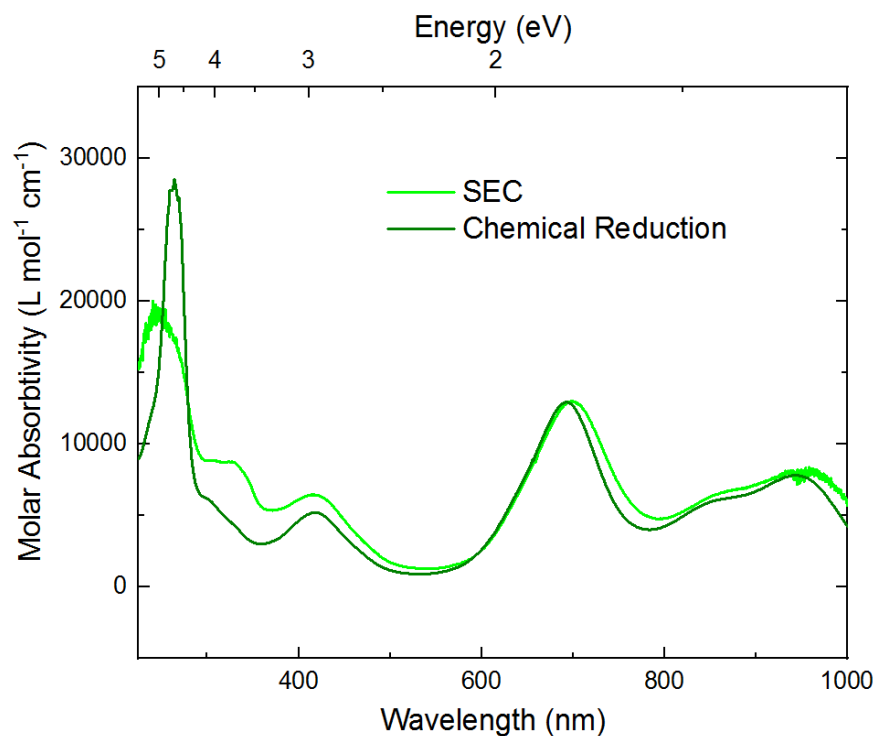

Figure S24. Electronic absorption spectra (THF) of electrochemically singly reduced **3** (produced by SEC) and **4** (produced by chemical reduction and isolation). SEC spectrum taken in the presence of 0.1 M [$^{n}Bu_4N$][PF_6] as electrolyte. Molar absorptivity calculated assuming complete conversion after constant current achieved in chronoamerometry experiment.

Crystallographic Information

Refinement Details for **3.**

A crystal of **3** was mounted on a nylon loop using Paratone oil under a nitrogen stream. Low temperature (200 K) X-ray data were obtained with a Bruker MicroStar microfocus rotating anode generator running at 50 mA and 45 kV (Cu Kα = 1.54178 Å; Apex II detector positioned at 50.0 mm and equipped with Helios multilayer mirror optics). All diffractometer manipulations, including data collection, integration and scaling were carried out using the Bruker APEXII software.[45] Absorption corrections were applied using SADABS.[46] The space group was determined on the basis of systematic absences and intensity statistics and the structure were solved were solved by intrinsic phasing using XT.[47] All non-hydrogen atoms were refined using anisotropic displacement parameters. Hydrogen atoms were placed in idealized positions and refined using a riding model. The structure was refined (weighted least squares refinement on F^2) to convergence using the Olex software package equipped with XL.[48]

Table S5: Crystal and Refinement Data

Compound	**3**
CCDC #	1842459
empirical formula	$C_{22}H_{24}ClF_6N_5O_4PRh$
formula wt	705.79
T (K)	199.99
a, Å	12.1943(2)
b, Å	18.7645(4)
c, Å	13.4798(2)
α, deg	90
β, deg	115.139(1)
γ, deg	90
V, Å^3	2792.29(9)
Z	4
cryst. syst	monoclinic
space group	$P2_{1/c}$
$\square_{calcd}$, g/cm^3	1.679
2θ range, deg	8.008 to 140.59
$\square$, mm^{-1}	7.088
abs corr	Multi-scan
GOOF^c	1.096
R1,^{a} wR2^b (I > 2σ(I))	0.0234, 0.0591

^{a} R1 = Σ||F$_o$|-|F$_c$|| / Σ|F$_o$| ^{b} wR2 = [Σ [w(F$_o^2$-F$_c^2$)^2] / Σ [w(F$_o^2$)^2]]$^{1/2}$ ^{c} GOOF = S = [Σ [w(F$_o^2$-F$_c^2$)^2] / (n-p)]$^{1/2}$

Special Refinement Details for 3.

In refinement of the structure of **3**, a single low-angle reflection (*hkl*: -2, 0, 2) was omitted due to abnormal intensity. The proximity of this reflection to the beamstop is likely responsible for the anomalous intensity. The structure of **3** contains a co-crystallized acetonitrile molecule.
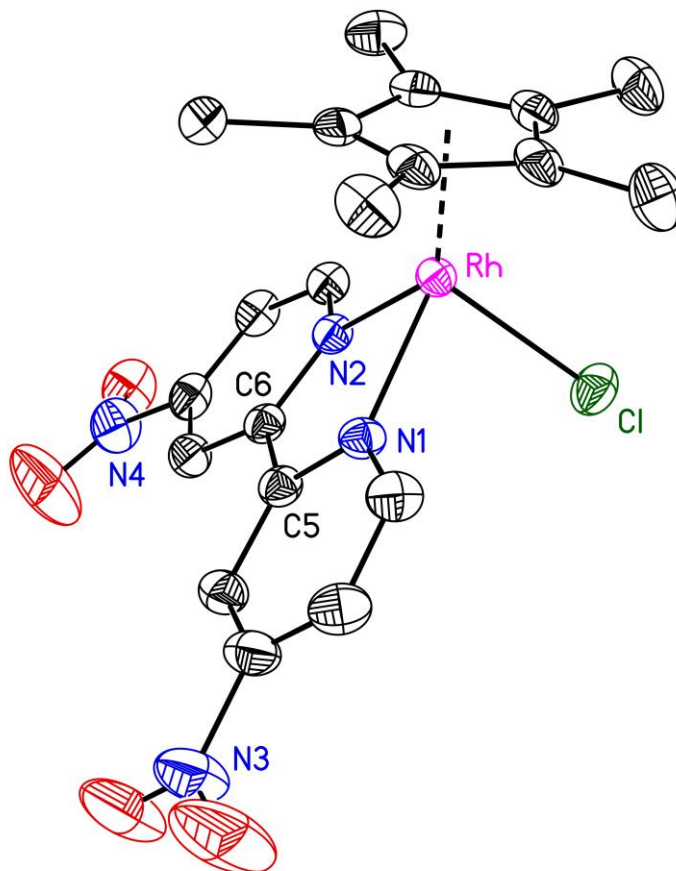

Figure S25: Solid-state structure of **3**. Hydrogen atoms, solvent, and counteranion are omitted for clarity. Displacement ellipsoids shown at the 50% probability level.
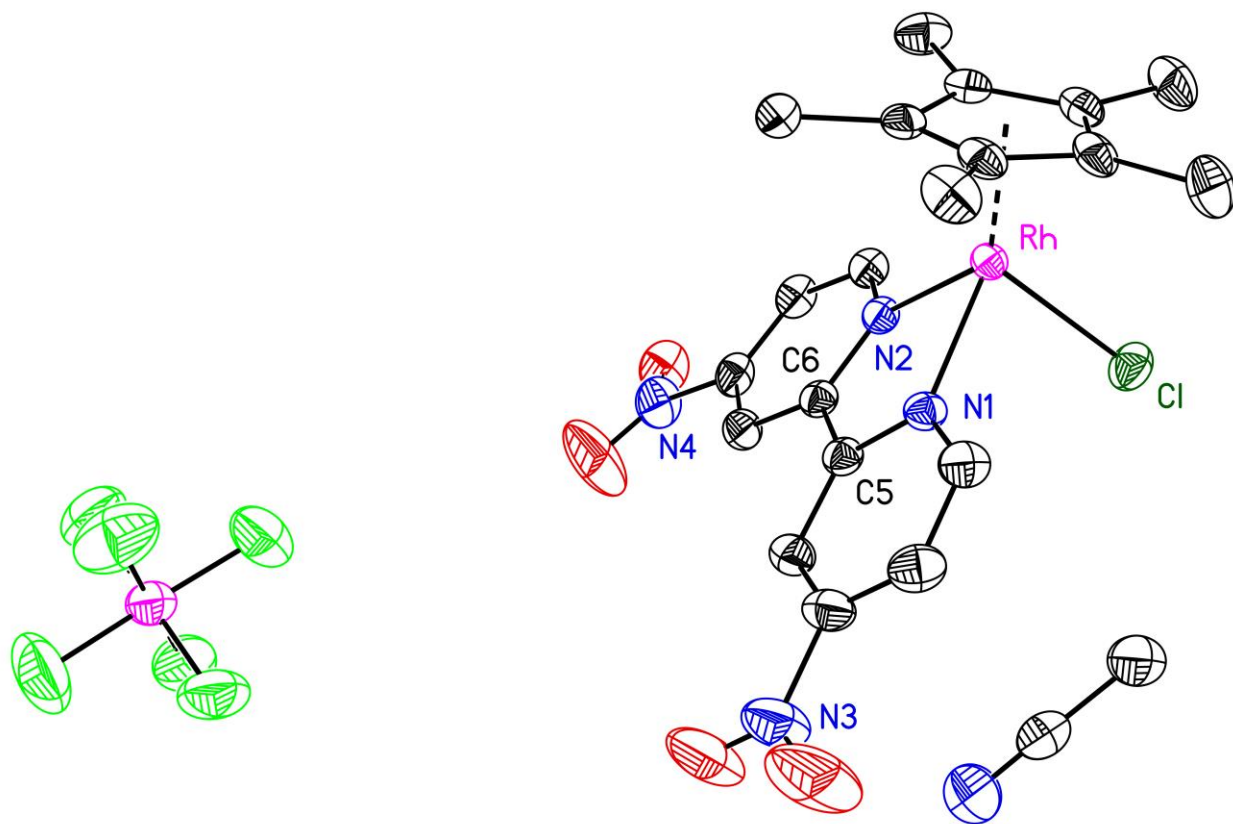
Figure S26: Full solid-state structure of **3**. Hydrogen atoms omitted for clarity. Displacement ellipsoids shown at the 50% probability level.
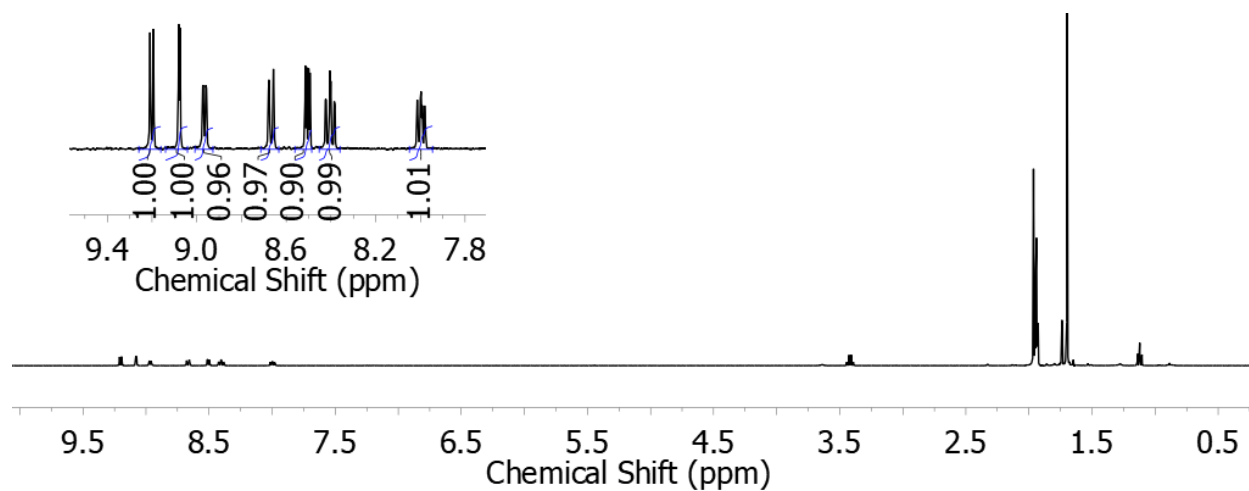
NMR Spectroscopy

Figure S1. ^{1}H NMR spectrum of [Cp*Rh($^{4\text{-}NO2}$bpy)NCMe][PF$_6$] in CD$_3$CN.
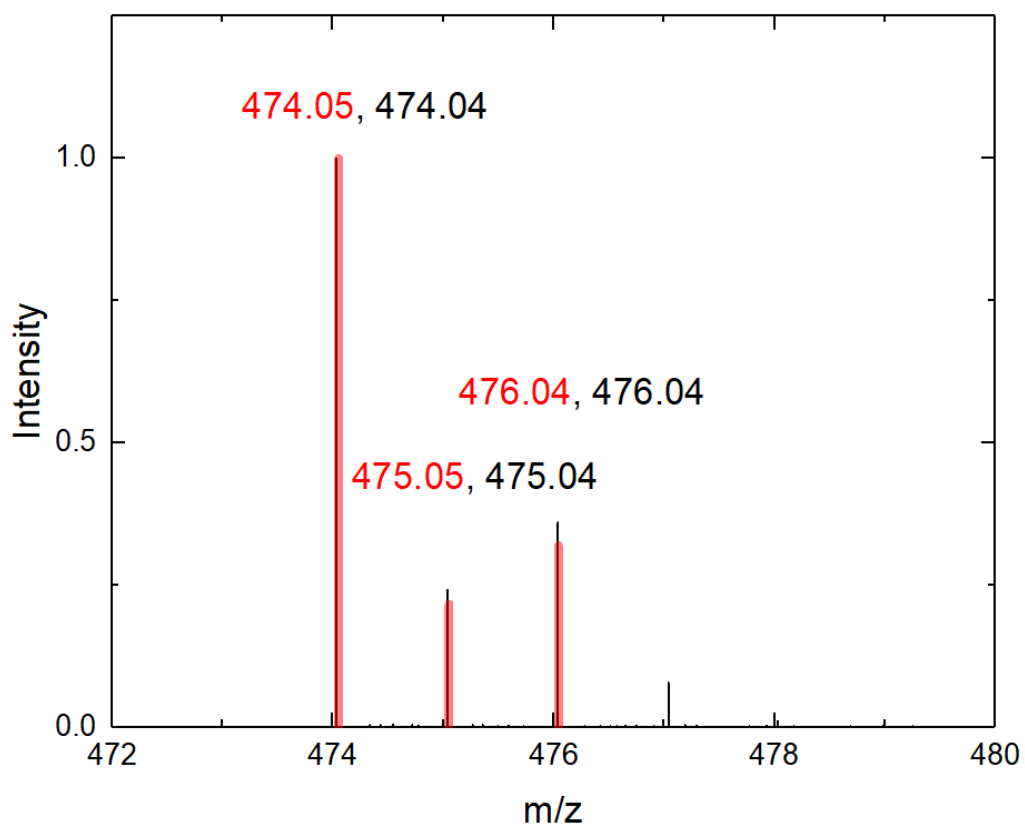
Mass Spectrometry

Figure S2. MS of complex **3** in MeCN solvent. Predictions based on ChemDraw calculations shown in red, actual data shown in black.
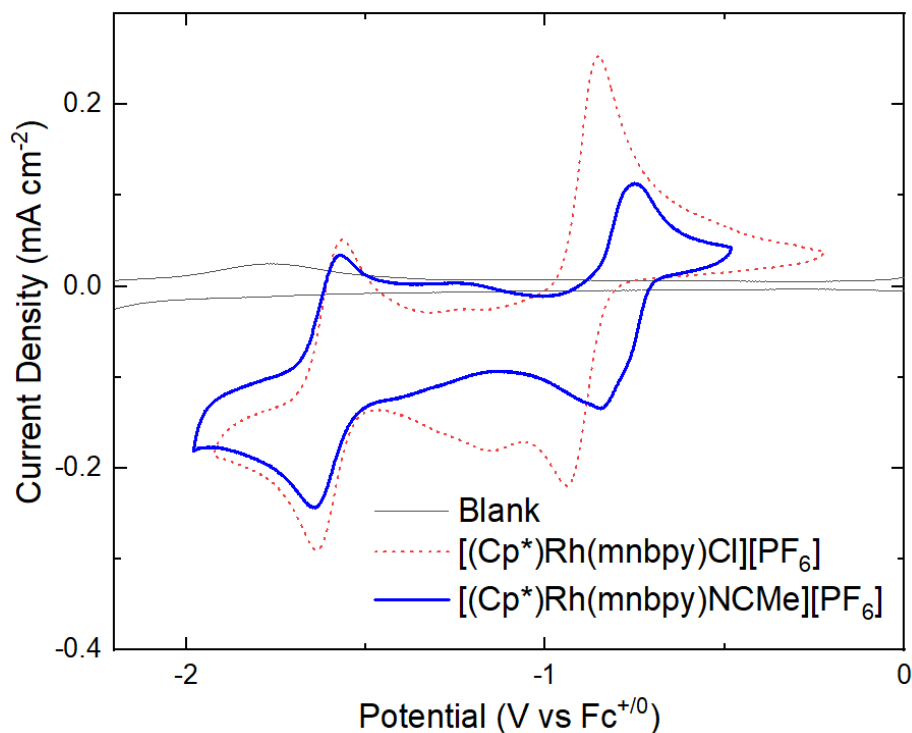
Electrochemistry

Figure S3. Comparison of electrochemical profile of **3**-solvento (with MeCN) and **3**. Concentration of compounds was ~ 1 mM. Electrolyte was 0.1 M $^NBu_4PF_6$ in MeCN. WE = HOPG, CE = Pt, RE = Ag$^{+/0}$.
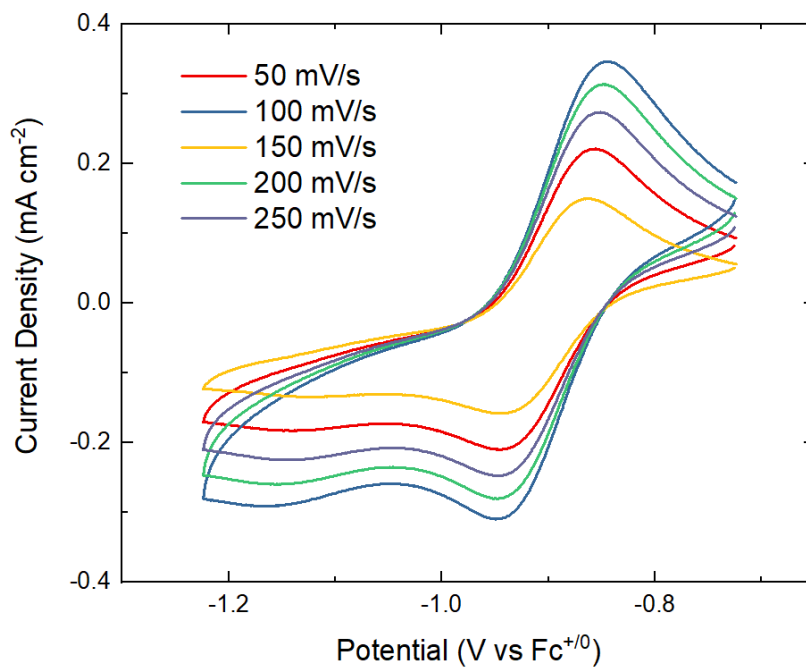

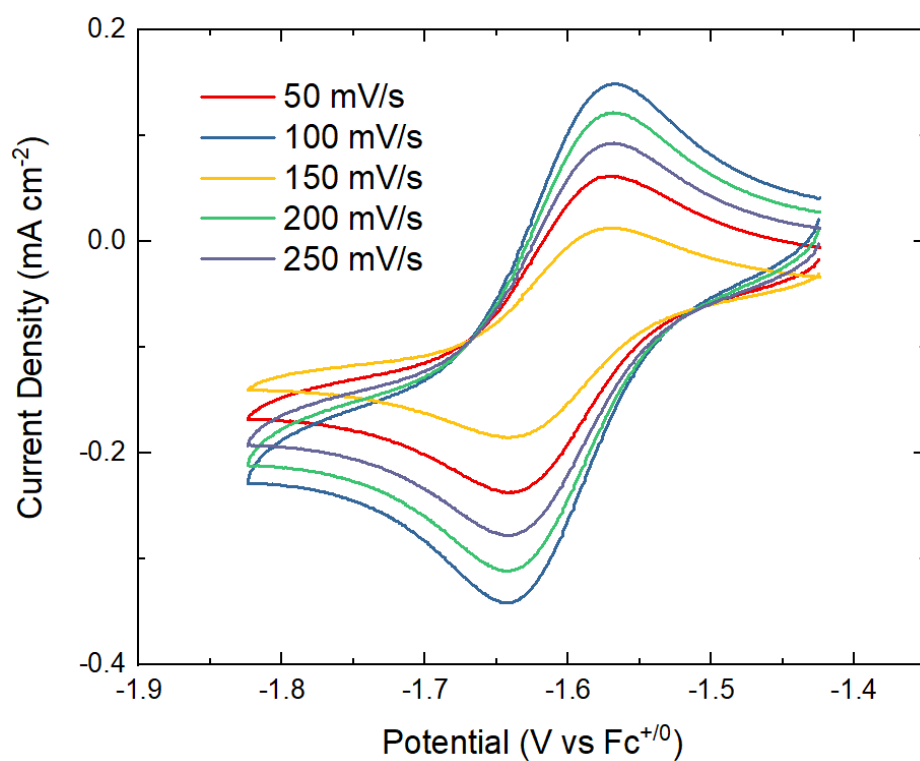**Figure S4.** Scan rate dependence of couple "A," complex **3**.

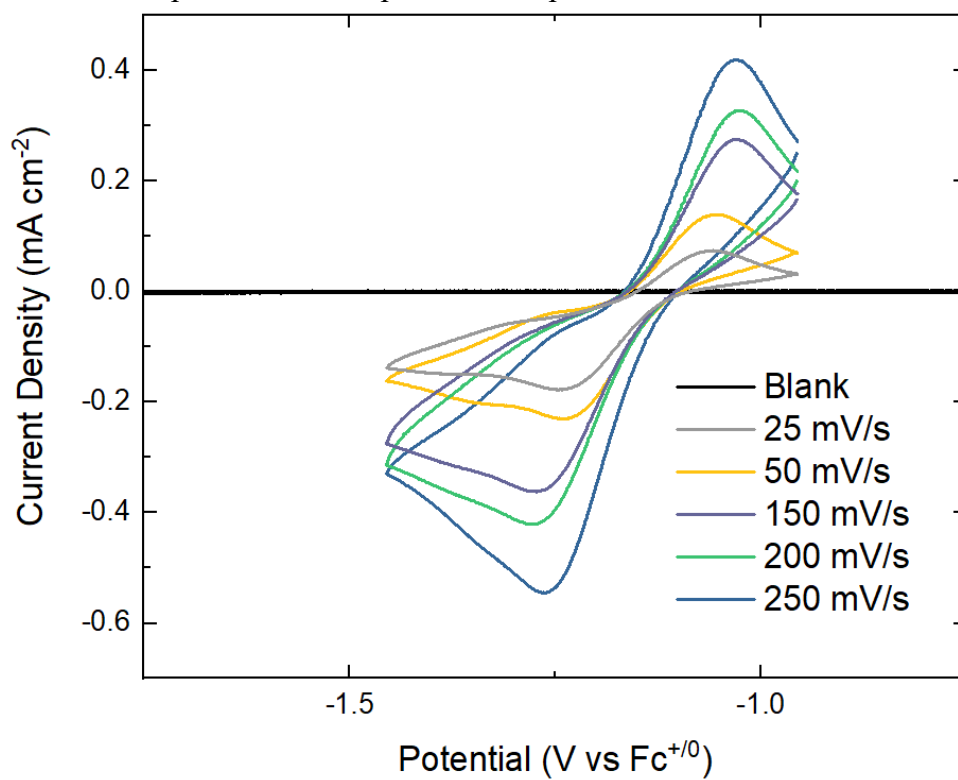**Figure S5.** Scan rate dependence of couple "B," complex **3**.

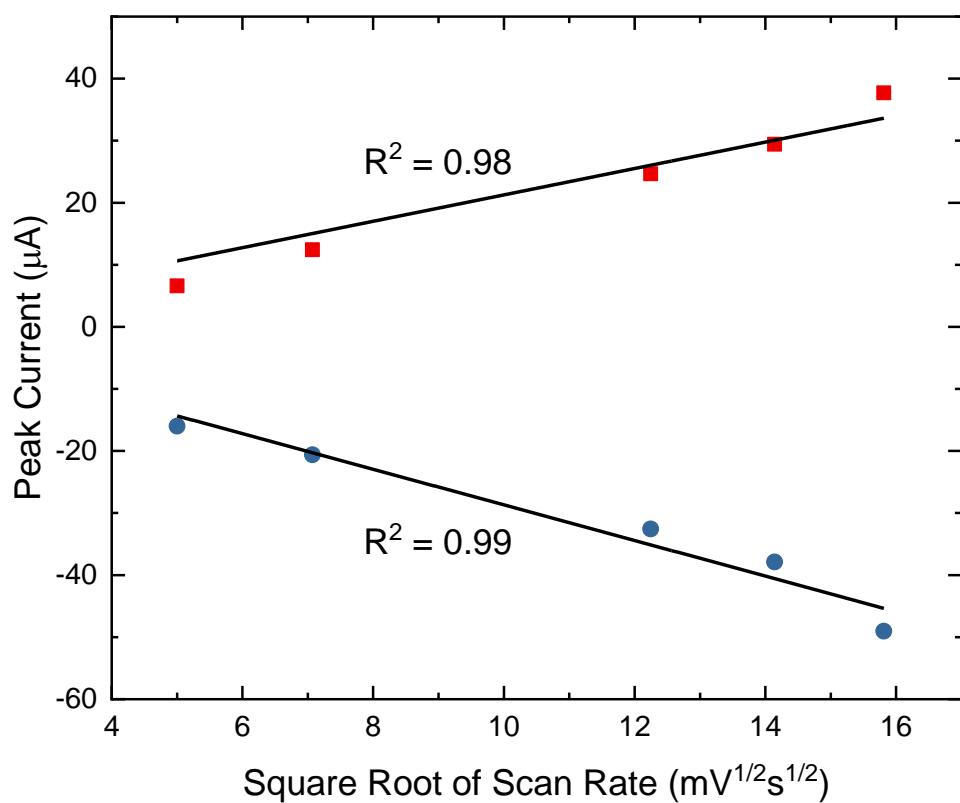**Figure S6.** Scan rate dependence of complex **4**.

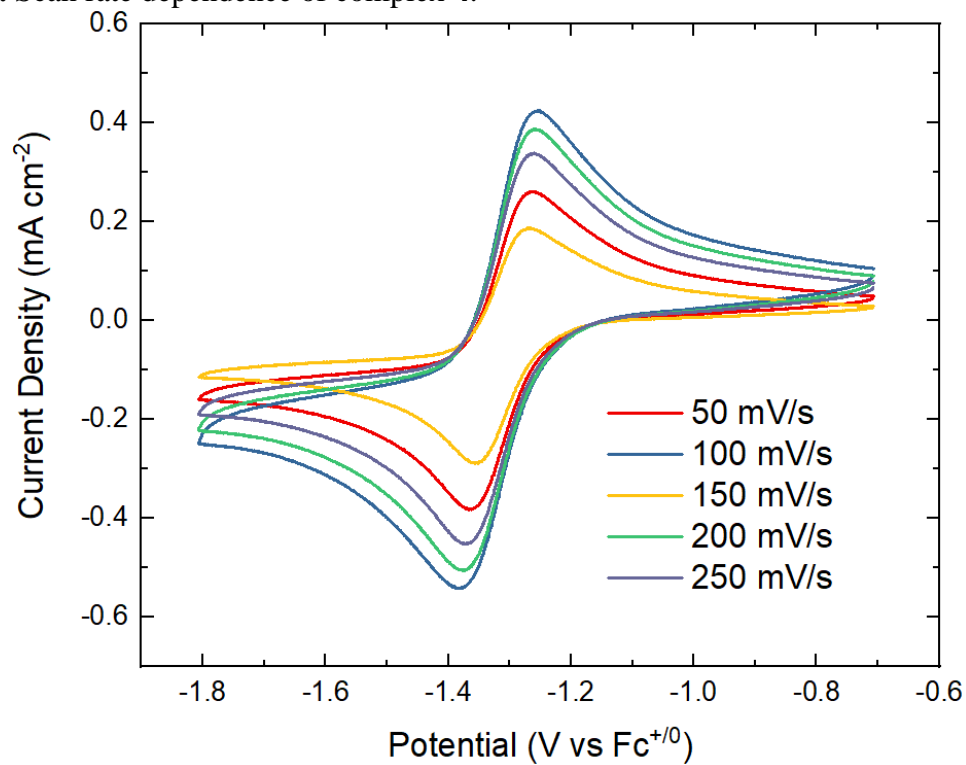**Figure S7.** Scan rate dependence of complex **4**.

Figure S8. Scan rate dependence of complex **6**.

References

[1] T. L. Cottrell, The Strengths of Chemical Bonds, 2nd ed., Butterworth, London, **1958**.

[2] Solomon, S.; Plattner, G.-K.; Knutti, R.; Friedlingstein, P. Irreversible Climate Change Due to Carbon Dioxide Emissions. *Proc. Natl. Acad. Sci. U. S. A.* **2009**, *106*, 1704–1709.

[3] Li, X.; Yu, J.; Jaroniec, M.; Chen, X., Cocatalysts for Selective Photoreduction of CO_2 into Solar Fuels. *Chem. Rev.* **2019,** *119*, 3962–4179.

[4] Lewis, N. S., Nocera, D.G., Powering the planet: Chemical challenges in solar energy utilization. *Proc. Natl. Acad. Sci. USA* **2006,** *103*, 15729–15735.

[5] Fripp, M., Switch: A Planning Tool for Power Systems with Large Shares of Intermittent Renewable Energy. *Environ. Sci. & Technol* **2012,** *46*, 6371–6378.

[6] Kölle, U. G., M., Organometallic Rhodium(III) Complexes as Catalysts for the Photoreduction of Protons to Hydrogen on Colloidal TiO2. *Angew. Chem. Int. Ed. Engl.* **1987,** *26*, 567–570.

[7] Blakemore, J.D., Hernandez, E.S., Sattler, W., Hunter, B.M., Brunschwig, B.S., Gray, H.B. Pentamethylcyclopentadienyl Rhodium Complexes, *Polyhedron*, **2014**, *84*, 14–18.

[8] Henke, W.C., Lionetti, D., Moore, W.N.G., Hopkins, J.A., Day, V.W., and Blakemore, J.D.,* Ligand Substituents Govern the Efficiency and Mechanistic Path of Hydrogen Production with [Cp*Rh] Catalysts, *ChemSusChem*, **2017**, *10*, 4589–4598.

[9] Hildebrand, F.; Kohlmann, C.; Franz, A.; Luetz, S. Synthesis, characterization and application of new rhodium complexes for indirect electrochemical cofactor regeneration. *Adv. Synth. Catal.* **2008**, 350, 909–918.

[10] Hansch, C.; Leo, A.; Taft, R.W. A survey of Hammett substituent constants and resonance and field parameters. *Chem. Rev.* **1991**, 91, 165–195.

[11] Simpson, P. G.; Vinciguerra, A.; Quagliano, J. V., The Donor Properties of 2,2'-Bipyridine N,N'-Dioxide. *Inorg. Chem.* **1963,** *2*, 282–286.

[12] Maerker, G.; Case, F. H., The Synthesis of Some 4,4'-Disubstituted 2,2'-Bipyridines. *J. Am. Chem. Soc.* **1958,** *80*, 2745–2748.

[13] Kavanagh, P.; Leech, D. Improved synthesis of 4,4′-diamino-2,2′-bipyridine from 4,4′-dinitro-2,2′-bipyridine-N,N′-dioxide. *Tet. Lett.* **2004**, *45*, 121–123.

[14] Zhang, D.; Telo, J.P.; Liao, C.; Hightower, S.E.; Clennan, E.L. Experimental and Computational Studies of Nuclear Substituted 1,10-Dimethyl-2,20-BipyridiniumTetrafluoroborates. *J. Phys. Chem. A* **2007**, *111*, 13567–13574.

[15] Wenkert, D.; Woodward, R.B. Studies of 2,2′-bipyridyl N,N′-dioxides. *J. Org. Chem.* **1983**, *48*, 283–289.

[16] ten Brink, G.-J.; Arends, I.W.C.E.; Hoogenraad, M.; Verspui, G.; Sheldon, R.A. Catalytic Conversions in Water. Part 22: Electronic Effects in the (Diimine)palladium(II)-Catalysed Aerobic Oxidation of Alcohols. *Adv. Synth. Catal.* **2003**, *345*, 497–505.

[17] White, C.; Yates, A.; Maitlis, P.M. (η^5-pentamethylcyclopentadienyl) -rhodium and -iridium Compounds. *Inorg. Synth.* **1992**, *29*, 228–234.

[18] Lionetti, D.; Day, V.W.; Lassalle-Kaiser, B.; Blakemore, J.D. Multiple binding modes of an unconjugated bis(pyridine) ligand stabilize low-valent [Cp*Rh] complexes. *Chem. Commun.* **2018**, *54*, 1694–1697.

[19] Kölle, U.; Kang, B.S.; Infelta, P.; Comte, P.; Grätzel, M. Electrochemical and pulse-radiolytic reduction of (pentamethylcyclopentadienyl)(polypyridyl)rhodiumcomplexes. *Chem. Ber.* **1989**, *122*, 1869–1880.

[20] Groom, C. R.; Bruno, I. J.; Lightfoot, M. P.; Ward, S. C., The Cambridge Structural Database. *Acta Cryst. Sec. B* **2016,** *72*, 171–179.

[21] Pilkington, M.; Capelli, S.; Hauser, J.; Hoffmann, C.; Burgi, H.-B., 4,4'-Dinitro-2,2'-bipyridine. *Acta Cryst. Sec. C* **1997,** *53*, 1719–1721.

[22] (a) Kinnunen, T.-J. J.; Haukka, M.; Nousiainen, M.; Patrikka, A.; Pakkanen, T. A., Electron withdrawing and electron donating effects of 4,4[prime or minute]-bipyridine substituents on ruthenium mono(bipyridine) complexes. *J. Chem. Soc. Dalton Trans.* **2001**, 2649-2654. (b) Moore, M.; Knight, D. A.; Zabetakis, D.; Deschamps, J. R.; Dressick, W. J.; Chang, E. L.; Lascano, B.; Nita, R.; Trammell, S. A., Electronic effects on the reactivity of copper mono-bipyridine complexes. *Inorg. Chem. Acta.* **2012,** *388*, 168-174. (c) McKeown, B. A.; Gonzalez, H. E.; Friedfeld, M. R.; Brosnahan, A. M.; Gunnoe, T. B.; Cundari, T. R.; Sabat, M., Platinum(II)-Catalyzed Ethylene Hydrophenylation: Switching Selectivity between Alkyl- and Vinylbenzene Production. *Organometallics* **2013,** *32* (9), 2857-2865. (d) S. Parsons, L. Yellowlees, P.A. Wood CCDC 247862: Experimental Crystal Structure Determination, **2014**, DOI: 10.5517/cc89xk0. (e) A.Yu. Kovalevsky, P. Coppens CCDC 179657: Experimental Crystal Structure Determination, **2014**, DOI: 10.5517/cc60ydj. (f) Weber, M. D.; Viciano-Chumillas, M.; Armentano, D.; Cano, J.; Costa, R. D., [sigma]-Hammett parameter: a strategy to enhance both photo- and electro-luminescence features of heteroleptic copper(I) complexes. *Dalton Trans.* **2017,** *46*, 6312-6323.

[23] There is a slight shift of the measured reduction potentials to more positive values (ca. 150-200 mV versus $Fc^{+/0}$) for all four redox events (see Appendix 1, Figure S10). Such solvent-dependent potential shifts are difficult to interpret reliably, although this shift may be explained by solvation effects that affect the $Fc^{+/0}$ couple in these two solvents (+0.40 V vs. SCE in MeCN vs. +0.56 V vs. SCE in THF).

[24] Saveant, J.-M. *Elements of Molecular and Biomolecular Electrochemistry*; Wiley: Hoboken, NJ, USA, **2006**.

[25] Hopkins, J.A., Lionetti, D., Day, V.W., and Blakemore, J.D.* Chemical and Electrochemical Properties of [Cp*Rh] Complexes Supported by a Hybrid Phosphine-Imine Ligand, *Organometallics*, **2019**, *38,* 1300–1310.

[26] Connelly, N.G.; Geiger, W.E. Chemical Redox Agents for Organometallic Chemistry. *Chem. Rev.* **1996**, *96*, 877–910.

[27] De Bruin, B.; Hetterscheid, D. G. H.; Koekkoek, A. J. J.; Grützmacher, H. In *Progress in Inorganic Chemistry*; John Wiley & Sons, Inc.: **2008**; Vol. 55, p 247–354.

[28] Lionetti, D.; Day, V.W.; Blakemore, J.D. Synthesis and Electrochemical Properties of Half-Sandwich Rhodium and Iridium Methyl Complexes. *Organometallics* **2017**, *36*, 1897–1905.

[29] (a) Creutz, C., Bipyridine radical ions. *Comments Inorg. Chem.* **1982,** *1*, 293–311. (b) Shida, T. *Electronic Absorption Spectra of Radical Ions*; Elsevier: Amsterdam; New York, **1988**.

[30] Coombe, V. T.; Heath, G. A.; MacKenzie, A. J.; Yellowlees, L. J., Spectroelectrochemical studies on tris(bipyridyl)iridium complexes: ultraviolet, visible and near-infrared spectra of the series [Ir(bipyridyl)$_3$]$^{3+/2+/+/0}$. *Inorg. Chem.* **1984,** *23*, 3423–3425.

[31] Appel, A.M.; Helm, M.L. Determining the Overpotential for a Molecular Electrocatalyst. *ACS Catal.* **2013**, *4*, 630–633.

[32] Muckerman, J.T.; Skone, J.H.; Ning, M.; Wasada-Tsutsui, Y. Toward the accurate calculation of pKa values in water and acetonitrile. *Biochim. Biophys. Acta Bioenerg.* **2013**, *1827*, 882–891.

[33] Murray, P. R.; Crawford, S.; Dawson, A.; Delf, A.; Findlay, C.; Jack, L.; McInnes, E. J. L.; Al-Musharafi, S.; Nichol, G. S.; Oswald, I.; Yellowlees, L. J., On the electronic structure of nitro-substituted bipyridines and their platinum complexes. *Dalton Trans.* **2012,** *41*, 201–207.

[34] Quintana, L.M.A.; Johnson, S.I.; Corona, S.L.; Villatoro, W.; Goddard, W.A.; Takase, M.K.; VanderVelde, D.G.; Winkler, J.R.; Gray, H.B.; Blakemore, J.D. Proton-hydride tautomerism in hydrogen evolution catalysis. *Proc. Nat. Acad. Sci. USA* **2016**, *113*, 6409–6414.

[35] Peng, Y.; Ramos-Garcés, M.V.; Lionetti, D.; Blakemore, J.D. Structural and Electrochemical Consequences of [Cp*] Ligand Protonation. *Inorg. Chem.* **2017**, *56*, 10824–10831.

[36] Smith, Barry E. Structure. Nitrogenase reveals its inner secrets. *Science* **2002**, *297*, 1654–1655.

[37] Paul N. Rylander, "Hydrogenation and Dehydrogenation" in *Ullmann's Encyclopedia of Industrial Chemistry*, Wiley-VCH, Weinheim, **2005**.

[38] Dawson, V. P.; Bowles, M. D. Taming Liquid Hydrogen: The Centaur Upper Stage Rocket (1958–2002). **2004**. Library of Congress.

[39] Aukauloo, A. & coworkers. Efficient electron transfer through a triazole link in ruthenium(II) polypyridine type complexes. *Chem. Commun.* **2011***, 47*, 11011–11013.

[40] Kodama, K.; Kobayashi, A.; Hirose, T.; Synthesis and spectral properties of ruthenium(II) complexes based on 2,2′-bipyridines modified by a perylene chromophore. *Tet. Lett.* **2013**, *54*, 5514–5517.

[41] Schwartz, K. R.; Chitta, R.; Bohnsack, J. N.; Ceckanowicz, D. J.; Miró, P.; Cramer, C. J.; Mann, K. R., Effect of Axially Projected Oligothiophene Pendants and Nitro-Functionalized Diimine Ligands on the Lowest Excited State in Cationic Ir(III) bis-Cyclometalates. *Inorg. Chem.* **2012,** *51*, 5082–5094.

[42] Shinkai, S. & coworkers. A boronic acid–diol interaction is useful for chiroselective transcription of the sugar structure to the Δ- *versus* Λ-[Co^{III}(bpy)$_3$]$^{3+}$ ratio. *J. Chem. Soc.*, *Perkin Trans. 2*, **1998**, 2281–2288.

[43] Crabtree, Robert H. *The Organometallic Chemistry of the Transition Metals*. Wiley, **2014**.

[44] DiLabio, G. A.; Ingold, K. U.; Solvolysis of para-Substituted Cumyl Chlorides. Brown and Okamoto's Electrophilic Substituent Constants Revisited Using Continuum Solvent Models. *J. Org. Chem.* **2004**, *69*, 1620–1624.

[45] *APEX2, Version 2 User Manual, M86-E01078,*; Bruker Analytical X-ray Systems: Madison, WI, June 2006.

[46] Sheldrick, G. M., SADABS (version 2008/1): Program for Absorption Correction for Data from Area Detector Frames, University of Göttingen, 2008.

[47] Sheldrick, G. *Acta Crystallogr., Sect. A: Found. Crystallogr.* **2015**, *71*, 3–8.

[48] Dolomanov, O. V.; Bourhis, L. J.; Gildea, R. J.; Howard, J. A. K.; Puschmann, H. *J. Appl. Crystallogr.* **2009**, *42*, 339–341.